UNIVERSITÀ DEGLI STUDI DI FIRENZE

PhD Thesis

Agnese Marcelli

Photophysical and photochemical processes in porphyrins and hemoproteins

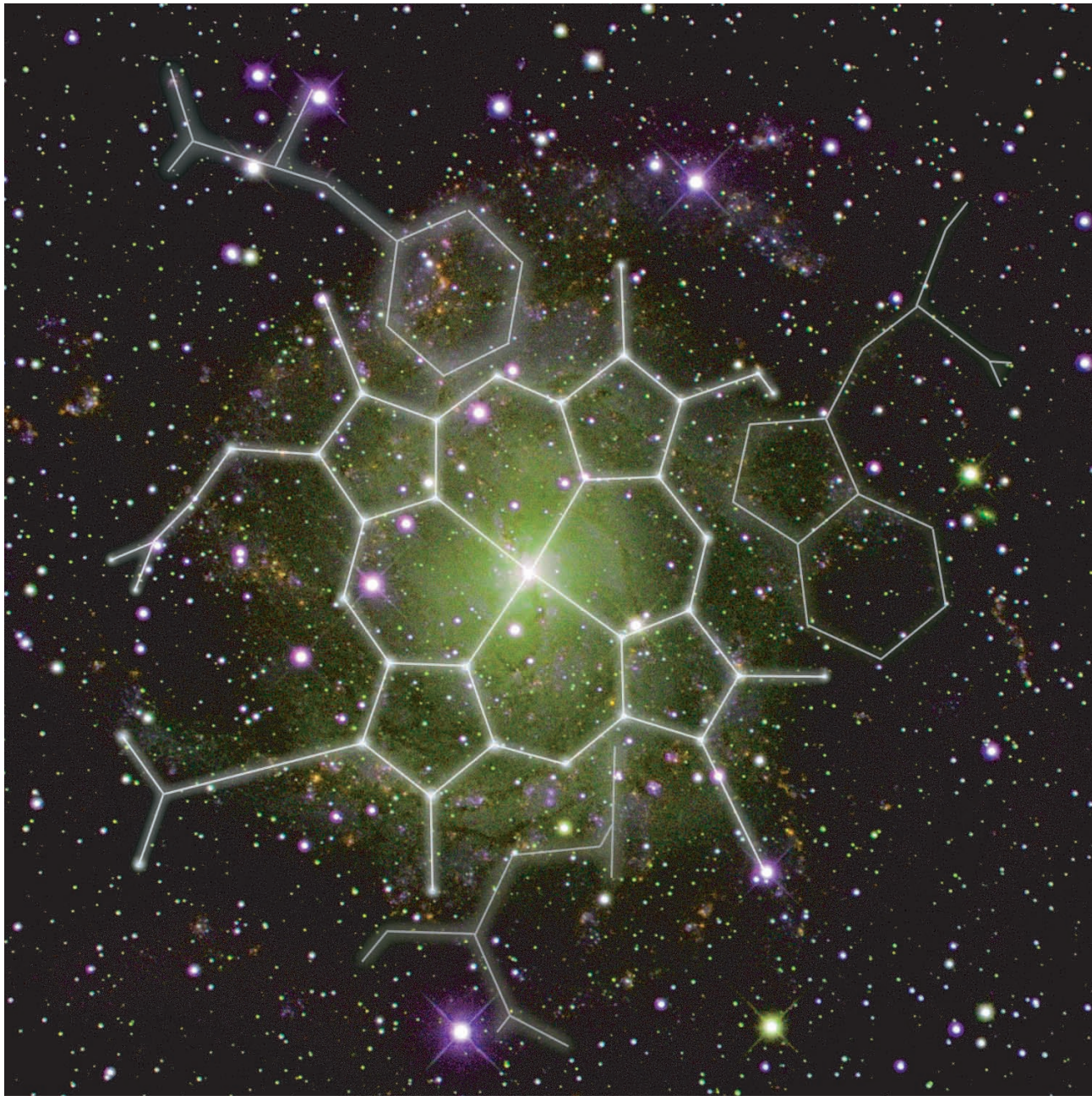

PHOTOPHYSICAL AND PHOTOCHEMICAL PROCESSES IN PORPHYRINS AND HEMOPROTEINS

Thesis submitted to the

Dipartimento di Chimica

Università degli Studi di Firenze

to obtain the degree of

DOTTORE DI RICERCA IN SCIENZE CHIMICHE

XXI ciclo

Settore disciplinare CHIM/02

presented by

Agnese Marcelli

Tutor	Coordinator of the PhD School
Prof. Roberto Righini	**Prof. Gianni Cardini**

December 2008

"If you can meet with Triumph and Disaster
And treat those two impostors just the same;"

Rudyard Kipling, **If**

Contents

Introduction and motivation

The common perception of hemoglobins and myoglobins as proteins tailored for the transport and storage of oxygen is not adequate to describe the functional properties of globins within all living organisms. In fact, the discovery of globin genes among prokaryotic and eukaryotic microorganisms rules out the possibility that the "hemoglobin-like" proteins were originally designed for oxygen transport or storage. At present, the number of these proteins is steadily increasing and these are amazingly distributed around the inside of a great variety of organisms, including bacteria, yeasts, algae, protozoa and fungi, distant from the phylogenetic point of view. This thesis is part of a broad range project, whose target is that of bridging the gap between fundamental research on novel bacterial hemoproteins and applications in the field of biotransformations, such as their future potential usage as auxiliary enzymes for bio-oxidative processes. In particular, this work reports on experimental observations of photochemical and photophysical processes in some porphyrins and bacterial hemoproteins, by means of time-resolved spectroscopy.

The recently discovered bacterial hemoglobins represent a very challenging class of proteins for hemoproteins dynamics studies. A number of questions concerning the connection between the original structural properties, the dynamics and the activity of these proteins is increasing. Despite the diverse functions of the hemoproteins, many of them are not fully understood yet, they have a common prosthetic group: the heme, composed of an iron-porphyrin complex. There is a great deal of evidence demonstrating that the

biological activity of the proteins is controlled by the conformational and electronic properties of this "chromophore". Therefore, the present research is focused on spectroscopic properties, starting from the basic porphyrinic system to more complex systems such as hemoproteins.

Light is not a natural ingredient of hemoprotein biochemistry, however optical techniques provide powerful tools to investigate activated processes strongly correlated with the functionality of such systems. An intense pulse of light interacts with the protein system at the electronic level and takes it "instantaneously" out of equilibrium, triggering a cascade of dynamical processes eventually bringing the system to a new equilibrium position. In particular, the ligand photodissociation by short laser pulses is widely employed in hemoproteins-carbon monoxide adducts to assess the dynamic, steric and electrostatic role of the heme environment. The target of the investigations is an ambitious one and concerns the understanding of the protein functioning at the atomic level. After the photodissociation, the ligand can either recombine with the iron atom from within the protein in a geminate mode, or diffuse into the solvent. If ligand is confined near the iron, the geminate recombination is observed; otherwise, the ligand diffuses further away. Iron out-of-plane displacement and heme doming following ligand dissociation accompany the whole photodissociation process, as well as the conformational details concerning the rearrangements of amino acid side chains within the heme pocket. These motions occur in the picosecond and sub-picosecond timescales and influence the geminate recombination rates of the photodissociated ligand.

"Does picosecond protein dynamics have survival value?" is an intriguing question to which the varied research proposals have tried to answer. Approximately 10 years ago, Brunori and coworkers [1] affirmed that the fast dynamic fluctuations have certainly this kind of value in hemoproteins and possibly in all proteins.

The experiments presented in this work utilize mainly pump-probe UV-vis transient absorption spectroscopy (TAS), employing ultrashort laser pulses ($\Delta t \leq 100$ fs). The method allows to characterize the short lived intermediates generated immediately after photoexcitation.

This thesis is organized as follows:
Chapter 1 provides an introduction to the "hemoglobin-like" proteins. Background and motivations of the study are highlighted. Furthermore, a summary of the current research in photodynamical and photochemical properties of the heme-contained systems is also presented.

In Chapter 2, we describe the basic principles and experimental set-up of TAS. Methods of data analysis are formulated and tested on the data recorded on samples of horse heart myoglobin, in order to assess their ability of reproducing previously reported results, and to check the sensitivity and time resolution of the instrumentation.

The photophysics of porphyrin and isoelectronic porphyrinic macrocycles is extensively described and discussed in Chapter 3, on the basis of time resolved absorption and fluorescence spectroscopy. The three studied molecular systems are the unsubstituted porphyrin (H_2P), diprotonated porphyrin (H_4P^{2+}), and tetraoxaporphyrin dication ($TOxP^{2+}$).

In Chapter 4, the spectroscopic study of a recently discovered protein is reported. The subject of this study is the truncated hemoglobin from *Thermobifida fusca*, we have carried out TAS measurements upon excitation in the Soret band, using CO as a ligand to the heme. The rebinding kinetics of the photo-detached ligand represents a sensitive tool for disentangling the interactions with the surrounding protein, and acts therefore as a probe for the chromophore-binding pocket dynamics.

The same approach has been followed in the study of a different protein system: the flavohemoglobin from *Escherichia coli* (HMP), reported in Chapter 5. Given the presence of an additional highly photosensitive chromophore (the flavin group), this investigation deserves particular care. Moreover, this protein shows the unusual heme iron-lipid acyl chain coordination; to this regard a dynamical study by femtosecond transient absorption spectroscopy can help in understanding this type of interaction. We have investigated the ferric and ferrous forms, and the correspondent CO complexes of the two lipid-free and lipid-bound HMPs.

Lastly, some final comments and a list of publications are given.

Chapter 1

State of art

1.1 The hemoglobin superfamily

The hemoglobins (Hbs) are found in a large variety of organisms (plant, animal, protist, and bacteria) and can be classified in the framework of the superfamily [2]. The hemoprotein polypeptide chain is arranged around the prosthetic group (the heme) building up the so-called *globin* structure, it determines the environment of the active site of the protein and consequently its functional properties. The protein chain is covalently bound to the heme, via the interaction between the iron of the heme and the imidazole ring of the histidine residue below the porphyrin ring, i.e. the proximal histidine. In the ferrous state, the sixth position can reversibly bind exogenous ligands, such as diatomic gaseous molecules in the so called distal position. The discovery of hemoglobins in all kingdoms of life raises fascinating questions about their physiological roles and the globin evolution. A recent work [3] has shown that lateral gene transfers from bacteria might be considered as responsible for the spread of the globin lineages. The presence of ancestral hemoglobin in Archaea [4] demonstrates that the gene for the globin proteins is very ancient and that the hemoglobins are designed for different functions than oxygen carriers as in the case of mammalian myoglobins. Nevertheless, an article entitled "Myoglobin's new clothes" [5] has been recently published in the prestigious journal *Nature*. Using myoglobin wild-type

and knockout mice, the authors have reported studies suggesting that the central role of myoglobin is related to the nitrite reductase activity and not to the oxygen storage.

The hitherto classification of the globins follows structural parameters rather than functional properties. Putative globin sequences have been identified in genomes from bacteria, archaea and eukaryotes and three globin lineages are singled out: the flavohemoglobins (FHbs), the globin-coupled sensor proteins (GCSs) and the "truncated" hemoglobins (trHbs) [3].

The FHbs are chimeric proteins comprising an N-terminal globin domain that exhibits the classical 3/3 globin fold, fused with a ferrodoxin reductase-like C-terminal FAD- and NAD-binding module. The genes codifying for the FHbs have been identified in a wide variety of bacteria and also in eukaryotic microorganisms, including yeasts and fungi. The physiological role of flavohemoglobins is still uncertain although consensus is emerging that envisages a role in the response of the bacterial cell to oxidative or nitrosative stress [6]. The GCSs have a two-domain structure containing an N-terminal sensor heme-globin domain with the 3-on-3 α-helical sandwich and a variable signaling domain. The latter lineage encompasses the single domain globins whose structures exhibit a 2/2 α-helical fold, based on four main α-helices of the classical fold. Although they are called "truncated" hemoglobins, their structure is the result of a complex modification of the canonical 3/3 globin fold, involving the whole protein chain, rather than of a simple "truncation" event [7]. These proteins display medium to extreme oxygen affinities, and have been proposed to be involved not only in oxygen transport but also in other biological functions, such as protection against reactive nitrogen species, photosynthesis and catalysis as terminal oxidases [8].

In spite of the impressive variability, among the globin proteins of the unicellular organisms, of the amino acids substitutions of the heme pocket, the heme is always covalently linked to the polypeptide chain through a proximal histidine residue (HisF8). Another highly, but not totally, conserved residue is the phenylalanine, the PheCD1, that appears to be necessary to stabilize the heme-binding [9].

The main features of the hemoglobin superfamily can thus be resumed in the following

points:

- the protein chain adopts a common structural motif known as the "globin fold", which hosts the heme;
- the heme is covalently linked to the protein chain through the Fe-HisF8 bond (proximal site);
- the iron of heme in the ferrous state is able to bind diatomic molecules, such as O_2, NO and CO (distal site);
- the mechanism of ligand recognition and stabilization varies, depending on heme environment (polarity, steric hindrance, etc.)
- the protein surface is connected to the heme by a cavity/tunnel system, that controls the diffusion of the ligand through the protein.

Generally, how does the protein structure determine its complex dynamic nature is one intriguing question that the present-day scientific community is still facing. This is the motivation of a great number of experiments turned to understand the protein structure-function correlation.

In this thesis, we focus our attention on the description of two important families of the hemoglobins-like proteins: trHbs and FHbs.

1.1.1 The truncated Hb family: an overview

More than three hundreds of truncated hemoglobin genes have been documented in the last 10-20 years in bacteria, unicellular eukaryotes and plants, they constitute a distinct phylogenetic group within the superfamily [10, 11].

The first evidence of hemoproteins in unicellular organisms was reported by T. Sato and H. Tamiya in 1937 [12] when spectroscopic studies on the suspensions of the ciliated protozoa *Paramecium caudatum* revealed the occurrence of hemoglobin-like protein. In 1953 Keilin and Riley confirmed the presence of hemoglobin in protozae [13]. The globin from *P.caudatum* was sequenced by Iwasaa four decades later (1989) [14], revealing 116

amino acid residues and a quite low sequence identity with vertebrate Hbs. The reduced size of the polypeptide chain, combined with the ability to bind diatomic exogenous ligand (such as O_2 and CO) earned this protein and its relatives the name of "truncated hemoglobins".

The first 3D structure of trHb from *P.caudatum* was determined by Bolognesi and coworkers [8]. In Figure 1.1 it is compared with the sperm whale Mb fold.

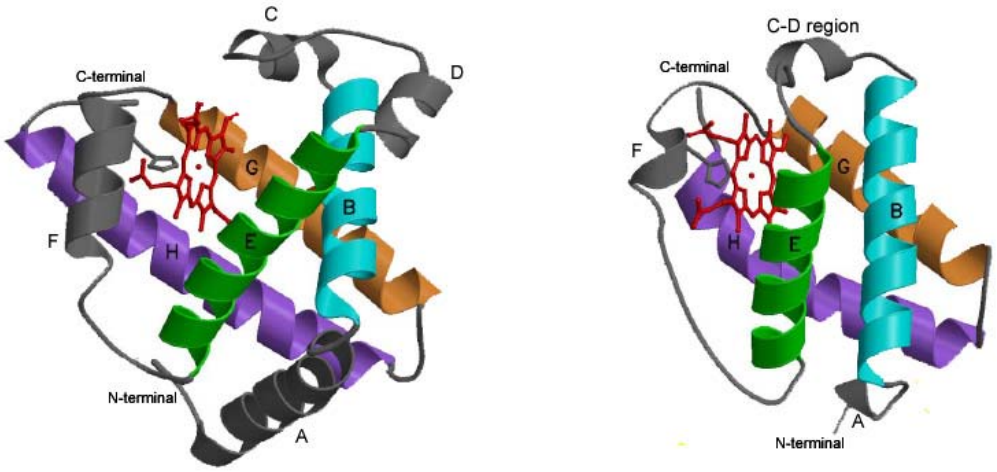

Figure 1.1: The α-helical sandwich fold in sperm whale Mb (3/3Hb, left) and in trHb from *P.caudatum* (2/2Hb, right). The figure has been taken from lecture by Prof. Bolognesi during the XII School of Pure and Applied Biophysics (*The ever changing world of (hemo)globins*, Venice 28 January - 2 February 2008).

The former is nearly two thirds of the latter in size. As observed above, based on structural features of the trHb family-fold the "truncated Hb" term does not represent properly the observed fold and the term "2/2Hb" is commonly used.

Thereafter many trHb genes have been found, most occurring in bacterial genomes. The analysis of increasing number of proteins has shown that this new globin family splits into three groups, designed as I, II and III (also distinguished by the N, O and P characters, respectively) [7]. The affiliation of each group depends on the internal sequence conservation. It is noticed that the patterns of amino acid conservation in the

heme pocket of each of these groups differ from that of vertebrate or invertebrate 3/3Hbs and that the sequence identity between trHbs from different groups is lower than 20% of the overall identity, while it is very high within a given group. 2/2Hbs from more than one group can coexist in the same organism, indicating a diversification of their functions.

From this picture it emerges that in the trHbs family the deviation from the 3/3 classical globin fold is only partly common to the three group. Specific structural features are typical for each group. Among the general features, we can assert that the trHbs are small hemoproteins, typically 20-40 residues shorter than mammalian Hbs. Their A-helix is drastically shorter, the D-helix is absent and an extended polypeptide segment (pre-F), followed by a short F-helix (one helix turn) is present. The helices are labelled according to the conventional globin fold nomenclature, A through H, starting from the N-terminal. Moreover, the C-D region is trimmed to about three residues, linking directly the C- and E-helices. Three Gly-motifs are individuated at the AB, at the EF inter-helical corners and just before the short F-helix, they have been suggested to contribute to the stabilization of the 2/2 fold, helping in locating the short A-helix onto the B- and E-helices. Besides the bend of H-helix, this one and the G-helix match the globin fold topology. These structural features are common in groups I and II; the only relevant difference is the presence of the pre-F helix in group II, see Figure 1.2. In fact, in group II the pre-F segment region hosts 15 residues, as the result of two amino acid insertions. This modification is reflected in the presence of a novel six-residue α-helix (the Φ-helix), involved in interactions with the heme propionate [15]. The deviation of the pre-F segment relative to group I trHbs may be related to a significant shift of the whole heme group within the heme crevice of trHbO (group II trHbs). In group III 2/2Hbs the A-helix is completely deleted, the AB hinge Gly-Gly motif is missing, thus forcing the protein residues preceding the B-helix to extend towards the GH region. An elongation of 7 amino acids is observed between the C- and E- helices. Such elongation of the CD region spans the C- and E-helices, but does not shift the position of the E-helix relative to the heme distal site.

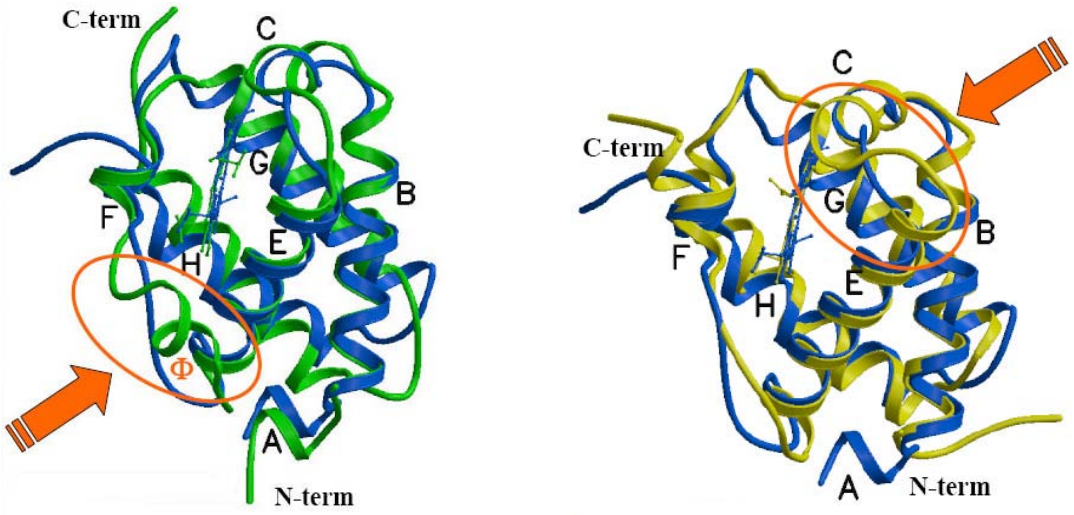

Figure 1.2: Comparative views of structural overlay between group I *Chlamydomonas eugametos* trHb (blue trace), group II *Mycobacterium tuberculosis* trHb (green trace) and group III *Campylobacter jejuni* trHb (yellow trace). (Figures taken from reference [16]).

In all 2/2 globins, the fold establishes a scaffold sufficient to efficiently bury the heme group, and the hydrophobic residues at topological positions provide a network of van der Waals contacts to the heme. Interactions between the heme and polar residues are known to provide further stabilization; additional salt bridges link heme propionates and positively charged residues. The unique heme-protein covalent interaction has been revealed in *Synechocystis* sp. 2/2HbN, occurring between the 2-vinyl group of the heme and an histidine residue [17].

A particular feature of this kind of proteins contrary to myoglobin of vertebrate is that, due to the shortened C-D region, the distal E-helix falls very close to the prosthetic group, thus causing side chain crowding of the distal site residues at topological position, such as B10, CD1, E7, E11 and G8. The topological positions within the globin fold of a single protein are referred to the tertiary structure of sperm whale myoglobin and are shown in Figure 1.3. Some of these residues are polar, allowing the formation of a network of hydrogen bonds, functional to an efficient stabilization of the exogenous ligand, but also to the rebinding of dissociated ligands. The polarity of the distal residues is the common properties of the 2/2Hbs, but the residues involved in the building of the

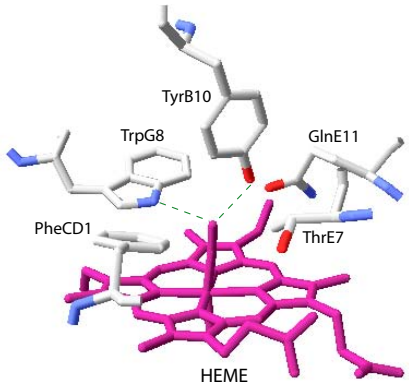

Figure 1.3: Scheme of the distal site of the CO complex of *Bacillus subtilis* 2/2HbO, in which the main residues discussed in the text and their topological positions are displayed. The green dashed lines show possible hydrogen-bonding interactions.

heme architecture switch over the three groups. In group I, for example, the hydrogen bond network involves residues at B10, E7 and E11 topological positions. The strongly conserved tyrosine (TyrB10) in position B10 plays a key role in the ligand stabilization through its OH group pointing directly to the heme ligand. Normally, the complete stabilization by hydrogen bond network is realized by a glutamine residue (Gln) located at E7 or E11, or at both positions. In group II, another residue, the tryptophan (TrpG8) is fully conserved; it contributes to the heme-bound ligand stabilization by the hydrogen bond linking the indole nitrogen atom and the ligand. Furthermore, the presence of a tyrosine at position CD1 in some 2/2HbO proteins drastically modifies the interaction network. In particular, structure and sequence analysis suggests that the nature of residues at CD1 is correlated with the nature of the site E11, at least for the group II trHbs. When the protein has a Tyr at CD1, a non polar residue is found at E11 position; conversely, when a non-hydrogen bond donor replaces the TyrCD1, a hydrogen bond donor is present in E11. TyrB10 and TrpG8 are invariant residues also in group III 2/2HbPs and are directly hydrogen bonded to the ligand. Contrary to group II, the group III truncated proteins display an invariantly Phe residue in CD1 position and a hydrophobic residue at position E11.

Table 1.1: Comparison of the topological site amino acids of selected trHbs, the first two rows refer to myoglobin from sperm whale and flavohemoglobin from *E.coli*, respectively. The trHbs are indicated by the name of the organism in which they occur. In bold type, the proteins studied in this thesis are highlighted.
The Protein Data Bank (PDB) codes are also reported.

Group	Organism	B10	CD1	E7	E11	F8	G8	PDB Code	[Ref]
	Sperm whale	L	F	H	V	H	I	1EBC	[18]
	Escherichia coli/HMP	Y	F	G	L	H	V	1GVH	[19]
	Paramecium caudatum	Y	F	Q	T	H	V	1DLW	[8]
I	Chlamydomonas eugametos	Y	F	Q	Q	H	V	1DLY	[8]
	Synechostis sp.	Y	F	Q	Q	H	V	1MWB	[20]
	Mycobacterium tuberculosis N	Y	F	L	Q	H	V	1IDR	[21]
	Mycobacterium tuberculosis O	Y	Y	A	L	H	W	1NGK	[15]
II	Bacillus subtilis	Y	F	T	Q	H	W	1UX8	[22]
	Thermobifida fusca	Y	Y	A	L	H	W	2BMM	[23]
III	Campylobacter jejuni	Y	F	H	I	H	W	2IG3	[24]

L = leucine; F = phenylalanine; H = histidine; V = valine; I = isoleucine; Y= tyrosine; Q = glutamine; T = threonine; A = alanine; W = tryptophan

All the consideration reported in this paragraph are discussed in the critical review by Pesce *et al* [7] and references inside. In table 1.1, the occupancy of the topological sites in different trHbs is summarized and compared with the sperm whale myoglobin and with the flavohemoglobin from *E.coli*.

As a general feature of protein matrix, although the protein fold is simple and very well conserved, different routes for ligand diffusion to/from the heme may be coded: the group I 2/2HbN proteins show a cavity/tunnel system connecting the protein surface to the heme distal site, the group II 2/2HbOs have a highly restricted protein matrix tunnel and finally, no evident cavity/tunnel system is present in group III 2/2HbP proteins. It has been reported [10] that in the first group the tunnel is composed of two orthogonal

branches from different access sites. Its potential role is thought to be the diffusion support and the accumulation of low polarity ligands/molecules. The residues lining the tunnels are generally hydrophobic. Instead, due to the different relative orientations of the helices and mainly to the increased volume of the side chains, the tunnel in group II is partially filled; in particular, the TrpG8 residue occupies the analogous volume of the shorter tunnel branch observed in group I, in the deeper part of the distal site pocket. The volume of the longer tunnel branch retains only two cavities, both fully shielded from bulk solvent.

1.1.2 The flavohemoglobin family

Flavohemoglobins are widespread within prokaryotes and eukaryotes, although their distribution does not follow a discernible pattern. They can be seen as chimeric protein in which a globin domain is fused with a ferrodoxin reductase-like domain. The flavohemoglobin heme domain is structurally similar to the single chain ancestral form of Hb and the heme pocket environment is strongly conserved among the members of the family on both the proximal and distal sites, thus suggesting a similar functional behavior within different microorganisms. In parallel, also the amino acid residues responsible for flavin binding are strictly conserved. The physiological role of flavohemoglobins is still uncertain; a NO scavenge activity has been already proposed, in which NO is converted to nitrate by reaction with the oxygenated heme [6, 25]. However, biochemical investigations have shown that these proteins possess a reductase activity. In fact, the heme iron is capable of efficient turnover in the ferrous state and catalyzes the reduction of multiple substrates.

Moreover, different kind of bacterial hemoglobins have been demonstrated to interact with membrane phospholipids both *in vivo* and *in vitro*. Ferrous form of *Alcaligenes eutrophus* flavoemoglobin (FHP) has been found to crystallize embedding a phospholipid molecule in the heme pocket [26, 27] and *Vitreoscilla* hemoglobin (VHb) [28], as well as *Mycobacterium tuberculosis* truncated hemoglobin HbO [29], have been reported to be preferentially located in contact with the bacterial inner membrane *in vivo* and to

be capable of reversible binding to liposomes *in vitro*. Recently, flavohemoglobin from *Escherichia coli* (HMP) has been shown to be able to bind reversibly a number of unsatured and cyclopropanated pospholipid and fatty acids [30]. This interaction is considered unusual due to the fact that it occurs in the ferric heme form. The binding results in a spectral change observed in UV-visible absorption, resonance Raman, EXAFS (Extended X-ray Absorption Fine Spectroscopy) and XANES (X-ray Absorption Near Edge Spectroscopy) spectra. Unfortunately, the 3D crystal structure of ferric ligand-bound HMP is not available, because the crystallization could not be achieved under the same experimental conditions in which the lipid-free derivative easily yields small hexagonal crystals [19].

The recently observed affinity for membrane lipids together with the reductase action, suggests that flavohemoglobins might be involved in the reduction of lipids under oxidative stress conditions within the bacteria cell. At the moment no evidence has been found yet for HMP to take part in the *in vivo* membrane repair mechanism, leaving open space for novel functional hypotheses. In these framework, an investigation by time resolved spectroscopy can help in understanding the interactions implied in the active site of the proteins.

1.2 Electronic absorption spectra of heme and hemoproteins

The biochemical activity and the electronic properties of hemoproteins derive in part from the possible electronic states of the heme group. It is well accepted that heme is of considerable biological importance, forming the active center of the ligand binding (myoglobins), electron transfer (cytochromes) and catalytic (peroxidases, etc.) proteins. Note that several biologically important kinds of heme exist, the most important one is the heme *b* and we refer to it in this thesis.

The heme contains one iron atom, coordinating the nitrogens of the protoporphyrin IX in the equatorial positions (see Figure 1.4). The protoporphyrin IX is the tetrapyrrole

macrocycle with different peripheral substituents: two vinyl groups in positions 2 and 4, four methyl groups in 1, 3, 5 and 8 and two propionyl chains in positions 6 and 7. The iron can assume two stable oxidation state, the ferric (FeIII) and ferrous (FeII) forms. The

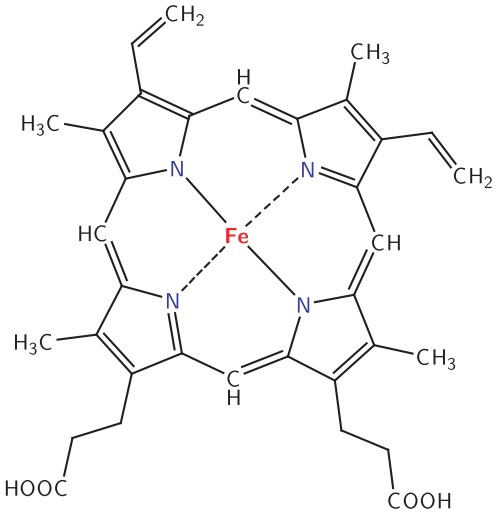

Figure 1.4: Structure of Fe-protoporphyrin IX: the heme.

optical properties of the iron-protoporphyrin IX complexes have been studied since many years [31, 32] and are considered deriving from the highly conjugated π-electron system. Two electronic transitions dominate the UV-visible region of the absorption spectrum of iron-porphyrin complex. The extinction coefficient of the low-energy transition is of the order of 10^4 $M^{-1}cm^{-1}$, the originated band is called Q_0, with its vibronic envelope, Q_v. While the intense B band is present in the violet region of the absorption spectrum with an extinction coefficient about ten times as great. They correspond to the porphyrin $\pi - \pi^*$ singlet transitions. The three signals have been referred by biochemists in order of increasing energy as α (Q_0), β (Q_v) and Soret (B) bands. Furthermore, an extra band at longer wavelength is present in the ferric state and its origin has been ascribed to ring to metal CT (charge transfer) transition. The intensity and the wavelength of a CT band are related to the difference between the d orbitals of the metal and the π^* orbitals of the porphyrins, and potentially to the nature of the axial ligands. Since the porphyrin $\pi - \pi^*$ singlet transitions are polarized in the plane of the macrocycle, they are all double

degenerate. In protoporphyrin IX, as in all the free based porphyrins, the plane does not longer possess the fourfold symmetry, due to the presence of two hydrogen atoms instead of the metal. So, the Q_0 transition is replaced by transitions polarized along each of the inequivalent axes: Q_0^x and Q_0^y, with their respective vibronic structure. So, there are four bands in the visible region (see Figure 1.5), while we note that the split of the Soret band is not resolved. Major details regarding the influence of the porphyrin macrocycle geometry on the determination of the spectral features are given in Chapter 3.

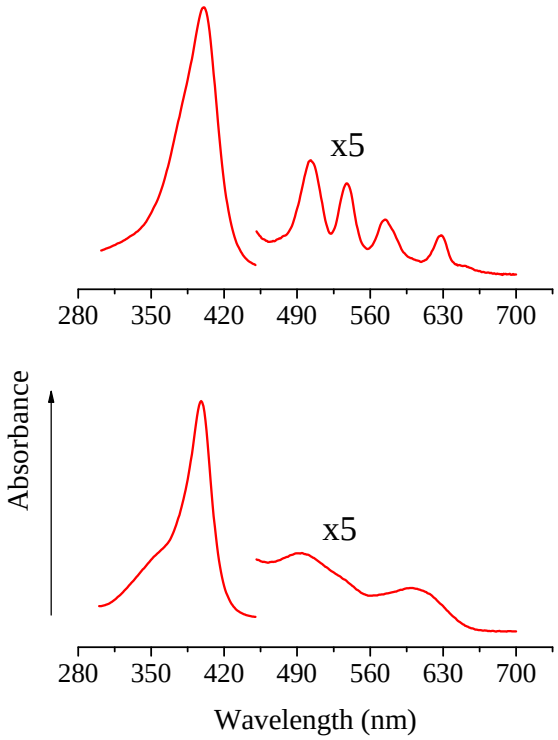

Figure 1.5: Absorption spectra of protoporphyrin IX (upper) and ferric hemin chloride (lower) in methanol.

The absorption spectra of the heme are also strongly affected by the environment, in particular by the protein chain. The oxidation and spin states play an important role in the determination of the spectroscopic properties of the hemoproteins. Fe(II) has six valence electrons in its $3d$ orbitals while Fe(III) has five valence electrons. The two axial positions of the iron atom can be occupied by ligands and they could introduce

an external perturbation. If the interaction with ligands is weak or the sixth position is not occupied, the d orbitals are quasi-degenerate and the occupancy follows the Hund's rule, thus producing a high spin (HS) configuration: S=5/2 for Fe(III) and S=2 for Fe(II). On the other hand, a strong interaction with the ligands can alter the relative energies of the $3d$ orbitals removing their degeneracy (the well-known process of ligand field splitting). The two $3d$ orbitals that point directly to the approaching ligands , i.e. the d_{z^2} and the $d_{x^2-y^2}$, are lifted in energy above the remaining three $3d$ orbitals. In this case , the electrons occupy only the lower orbitals (d_{xy},d_{xz} and d_{yz}) in a low spin (LS) configuration: S=1/2 for Fe(III) and S=0 for Fe(II). Since in the LS configuration the higher energy orbitals are unoccupied, the size of the core containing the iron atom is smaller than in the HS configuration and the metal lies in the plane of the tetrapyrrole ring, while the HS iron sits out of plane.

1.3 Photophysical model of relaxation processes in Hbs

The absorption of a photon by the heme can initiate a variety of sub-nanosecond processes that include the formation of transient excited electronic states with the subsequent structural response of the macrocycle to the new electronic configuration, and the non-radiative relaxation to the ground state. Photophysical behavior of metalloporphyrins in solutions were studied in detail by Holten and coworkers [33–35], they have shown that a number of various electronic states are involved in the relaxation path. The identification of the transient signals associated with the energy dissipation processes following heme photoexcitation is not only important and interesting by itself, but allows to proper separate these events from the ligand dynamics and from the protein structural relaxation in the hemoproteins studies.

To the best of our knowledge, the first paper dealing with excited state relaxation and photolysis in hemoproteins by means of subpicosecond optical pulses, was published in 1976 [36]. Photodissociation of carboxyhemoglobin (HbCO) was found to occur in less than 0.5 ps. The authors argued that the HbCO is easily dissociated because there

is a radiationless transition from the initially excited electronic state of the porphyrin π-electrons to a lower state corresponding to a $d_\pi \rightarrow d_{z^2}$ excitation of the iron atom. Contrary to d_π, the d_{z^2} orbital has a partially antibonding nature, which results in a repulsive force exerted on the CO molecule. An induced absorption was also observed; in the unliganded ferrous hemoglobin and oxyhemoglobin, the signal decays rapidly with a time constant of about 2.5 ps, while in HbCO it remains unchanged on a timescale of 20 ps. The observed response was interpreted as the evidence of a short-lived excited state. This experiment was carried out with a single color set-up using pulses at 615 nm for excitation and probing and it was not possible to identify the nature of such state. Subsequently efforts were made with the aim of measuring transient spectra with sufficiently high accuracy to identify the photoproducts [37, 38]. It was observed that the photolysis of HbCO brings to a broader, weaker and red-shifted signal compared with the steady-state spectrum of the deoxygenated ferrous Hb species. By means of extended Hückel calculations performed on the complex of iron-porphine with imidazole as a model chromophore, a detailed assignment of the transitions in the hemoglobin and its adducts were reported by Eaton *et al* [39].

In the early 1980s, femtosecond photolysis experiments in CO ligated Mb and Hb, along with the CO adduct of protoheme were carried out [40, 41]. The appearance of *deoxy* species was spotlighted with a 350 fs formation rate, identical for the three molecular species and independent of the presence of the protein chain. The authors discussed the kinetics of the signal rise on the basis of a spin-allowed dissociation channel. This requires the instantaneous formation of a transient high-spin ligated, highly photodissociative species, which relaxes to a stable high spin pentacoordinated state with out-of-plane displacement of iron. In other words, they suggested that the photodissociative species in heme-CO complexes is a low-lying multiplet ligand field state, populated via intersystem crossing. For the three molecules, an identical time constant of 3.2 ps was also observed and interpreted as the relaxation time of the directly excited ligated state towards the non-reactive ground state. For the sake of obtaining detailed information on the dynamics of the heme and of discriminating the energy dissipation processes after

photoexcitation from the structural relaxation, a Raman spectrometer providing, at the same time, both subpicosecond resolution and independently tunable pump and probe pulses was developed [42]. The obtained results are extensively reviewed by J.-L. Martin and M. H. Vos [43]. They concluded that in hemoprotein dynamics, the photodissociation of the ligand occurs in less than 50 fs with a quantum yield of approximately unity, irrespective of whether the ligand is CO, O_2 or NO, and that two short-lived species are formed upon ligand photodissociation. By following the kinetics of the transient bleaching of the Soret band after photoexcitation in the Q band, Martin and coworkers assigned these transients to excited states of the unligated heme and labelled them Hb^*_I and Hb^*_{II} [44]. The first was attributed to the transient species in which the heme is already partially domed and that decays in 300 fs to the ground state unligated species. The second was found to relax in 2.5-3.2 ps and the weight of this component was strongly dependent on the nature of the ligand, in particular it was found to be very low for the CO adduct. On the basis of experimental observations, the relaxation process was attributed to a homogeneous distribution of ligands in the heme pocket that rapidly recombine with heme. The fast recombination suggested that the heme in Hb^*_{II} does not change from the planar geometry of the ligated initial ground state and that the relative population is responsible for the geminate recombination of the ligand. Moreover, due to the similarities of the noticed protoheme behavior with those of hemoproteins, the authors of ref. [43] agreed that the steric features of the protein are less important than the nature of the ligand itself in determining the geminate recombination process. A general scheme of the absorption spectra of hemoproteins and of their photoproducts is reported in Figure 1.6. The $Hb^\dagger$ species, related to a non-equilibrium unligated hemoglobin and associated to the constraint in the hemoglobin tetramer, does not appear in a single chain protein, as myoglobin.

In the same paper, the authors note that an alternative assignment should be done for the two transient species Hb^*_I and Hb^*_{II}. Both of them might be attributed to vibrationally hot ground state unligated hemes. However, they consider the two states as electronic excited states because of the large frequency different between their absorptions

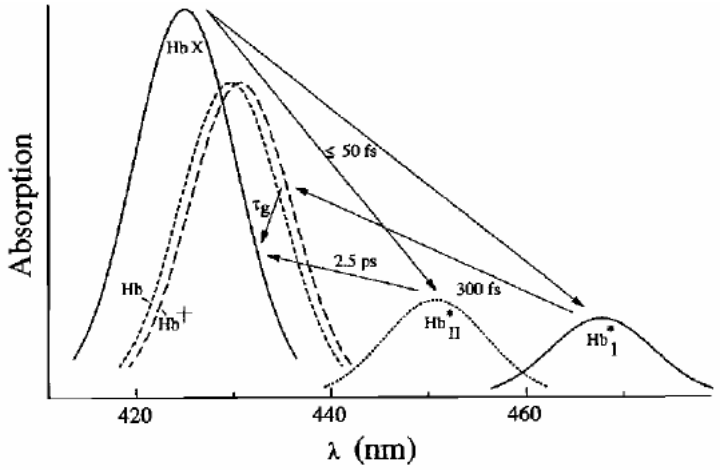

Figure 1.6: Generalized absorption spectra of heme proteins and their photoproduct, from Petrich *et al* [44]. X denotes the ligand (CO, O_2 or NO, indifferently).

and the ground state Soret band; in fact, the latter was known to be relatively insensitive to temperature. This model is one of first proposed, more recently in 2001 it has been corrected by Franzen and coworkers, including J.-L. Martin [45]. In contrast with the previous parallel model, they discuss a sequential model where the photoexcited heme decays to an intermediate state called Hb^*_I through a metal-to-ring ultrafast charge transfer ($\tau < 50$ fs). Subsequently, the Hb^*_{II} state arises from Hb^*_I via porphyrin-to-iron back charge transfer to produce a porphyrin ground state configuration and a non-equilibrium iron d-orbital population. So Hb^*_{II} was assigned to a vibrationally excited ground state macrocycle with a $d - d^*$ excited metal ion center. The sequential model can be written as: $^1Q \rightarrow Hb^*_I \rightarrow Hb^*_{II} \rightarrow Hb$. Hb^*_{II} is formed from Hb^*_I in less than 300 fs; its decay to the heme ground state occurs in about 3 ps.

The proposed pathway suggests also that the metal-to-ring ($d_\pi \rightarrow a_{1u}, a_{2u}$) charge transfer is the key event in the mechanism of photolysis of diatomic ligand following a porphyrin ring $\pi \rightarrow \pi^*$ transition. The entropy change enables the photoinduced charge transfer process, due to the stability of the high-spin d^5 Fe(III) CT state and the consequent destabilization of the Fe-CO bond, reducing the π-backbond by removal of electrons from the d_π orbitals. It has no effect on σ-donor ligands, such as histidine and water. This mechanism contrasts with the previously proposed process that involves a

spin-orbit interactions between the metal and the decaying ^1Q excited state with the increase of the electron density in the d_{z^2} orbital. The authors concluded that valence tautomerism provides a valid explanation for the mechanism of the diatomic ligand photodissociation and that the geminate recombination is governed by ligand-iron affinity rather than heme conformation (in-plane or out-of-plane) as opposite to Petrich *et al* have suggested [44]. Moreover, the heme iron out-of-plane displacement was found to be as rapid as the heme iron out-of-plane vibration period by sub-picosecond time resolved resonance Raman spectroscopy [46, 47].

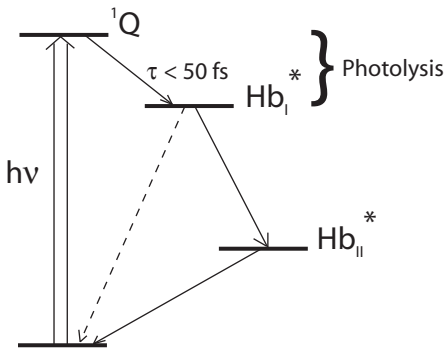

Figure 1.7: Kinetic scheme for heme photolysis decay, according to the model proposed by Franzen *et al* [45]. The dashed arrow displays the alternative sequentially decay of the Hb_I^* state towards the vibrationally hot ground state, as suggested by Kholodenko *et al* [48].

Another sequential model has just been discussed in 2000 by Kholodenko *et al* [48]. They obtained the transient spectral dynamics in the Q band and the III band regions after Soret band excitation of *deoxy* Mb. They detected two steps of electronic relaxation: a sub-100 fs step, seen as an instrument limited spike, and one with a time constant of a few hundred femtoseconds. After this second step, Mb is in a vibrationally hot, thermally non-equilibrated, ground electronic state. The vibrational relaxation shows a non-exponential behavior, that was fitted by a two exponential function, with a short time constant of a few ps and a second one, of smaller amplitude, of about 15-20 ps. The first time constant was related to the fast initial dephasing process due to the IVR (intramolecular vibration redistribution), while the second was attributed to a slower cooling process associated to the VR (vibrational relaxation) from the heme to the solvent

through the protein backbone [49]. The dynamics observed in the picoseconds temporal range was then ascribed to the vibrational cooling in the ground electronic state, with time constants consistent with the results of time-resolved Raman studies [42, 50]. A similar biphasic decay with time constant of 3 and 25 ps was reported for the relaxation of the ν_4 in-plane vibrational mode of the heme in myoglobin [51].

Lim *et al* [52] have proposed an intermediate picture for the process following the photoexcitation of myoglobin, in which contributions from both electronic and thermal relaxation are involved on the picosecond timescale. In fact, they found that the electronic relaxation to the ground state is not instantaneous (exponential growth time constant of 3.4 ± 0.4 ps), but proceeds through several intermediate electronic states, while the temperature of the electronically relaxed heme cools with a single exponential time constant of 6.2 ± 0.5 ps.

In Figure 1.7 the sequentially kinetic schemes are sketched, in accordance with the models proposed by Franzen *et al* [45] and by Kholodenko *et al* [48]. The difference between the two models is that in the former the intermediate relaxation step involving the the Hb^*_{II} state is present. From the shift of υ_4 band observed in time-resolved resonance Raman spectra, this state (living $\approx$ 3 ps) was interpreted as arising from an excited state with a non-equilibrium population of iron *d*-state. The Hb*II state has the ground state configuration if the porphyrin ring is considered (as demonstrated by Kholodenko and coworkers [48]). The authors also suggested that the dynamics does not depend on the amount of energy deposited into the heme by photoexcitation, at least within the range 20-70 kcal·mol^{-1}.

From the theoretical point of view, many papers deserve citation [53–57]. Their results confirm the assignment of the first intermediate state as an iron-to-ring charge transfer state, ruling out the possibility of an involvement of a high spin state in the photodissociation step. Although the analysis of data reported by Franzen *et al* [45] intends to resolve the contradiction between the previous different interpretations [44, 48, 52], the photophysical model of the relaxation processes in hemoproteins can not be considered certain yet.

In 2003, Ye and coworker published the results of their research on ferric and ferrous myoglobin, proposing an interpretation based on the vibrationally excited ("hot") electronic ground-state model [58]. Independently from the oxidation and ligation states, the spectra show an initially broad and red-shifted transient absorption signals which eventually decay to a typical band profile of a thermally relaxed state. Two components of the spectral evolution were discussed, involving both intramolecular, non-Boltzmann, vibrational redistribution (<1 ps) and cooling of a hot, Boltzmann equilibrated heme via vibrational energy transfer from the heme to the protein/solvent heat bath. Their discussion was based on the time evolution of specific spectral features; in particular, the authors observed on the blue side of the Soret band a component that could not be adequately explained. Under this respect the multiple electronic intermediate excited-state model results incorrect. They compared their point of view with the work published in 1988 by Petrich *et al*, stressing that the model proposed by Petrich *et al* was based on only single wavelength measurements. To tell the true, their discussion omitted any confrontation with the sequential model of Franzen *et al*, cited above. It was only enumerated as an example of multiple electronic state models.

In conclusion, different models have been proposed for the interpretation the ultrafast heme dynamics and for the nature of the short lived intermediates generated immediately after photolysis. Although the role of low-lying electronic excited state and of vibrational energy relaxation in the heme time evolution after photo-excitation represents the key point of the current research on hemoprotein dynamics, the route towards an unified picture is not straightforward and is currently the subject of debate.

1.4 Ligand migration properties

Ligand photodissociation with short laser pulses in hemoproteins-ligand adducts is widely employed in order to unravel the elementary dynamical processes underlining the functional properties of the proteins. The rebinding processes following ligand photolysis are often complex and depend of different factors, such as the reactivity of the heme iron

with specific ligands and the protein matrix surrounding the ligand binding site. The experimental investigated process is somehow opposite to the *in vivo* mechanism. In fact, the physiological cleavage of the iron-ligand bond occurs by thermal activation, the probability of the rebinding event strongly depends on the structure and dynamics of the protein chain. The impossibility of synchronizing the measurements with the arrival of external ligands in the near vicinity of the heme active site renders impossible to follow the direct conformational changes on the ultrafast timescale. Therefore, although the photodissociation is not a physiologically relevant event, it can be used to mimic the actual dynamics of the protein. In particular, the ultrafast processes triggered by the optical pulses are strongly related to the structure of the protein and to the protein-cofactor interactions [43]. The phonon energy exceeding that needed to dissociate the ligand is deposited initially into the heme. As rapid as the electronic relaxation, the heme iron moves out-of-plane, triggering a global conformational change of the protein [46]. Most experiments addressing the binding kinetics in hemoproteins use CO as ligand, although in Mb or Hb the importance of O_2 would be readily obvious. The preference for CO arises from the fact that the protein-CO complex is spectroscopically easy clear to observe [56], its photodissociation quantum yield is equal to 1 [59] and the complex is easier to obtain than using O_2 or NO.

The overall picture is based mainly on observations on myoglobins and their site-directed mutants. It is well known [60] that the photodissociated ligand can either recombine rapidly with the metal or diffuse out into the solvent. If the amino acids residues constituting the pocket heme confine the ligand near the metal, the geminate recombination takes place; instead, if the ligand can easily diffuse away, the chances of ligand-metal encounters decrease. The two possible scenarios can be discussed in terms of the amplitude and rate of the geminate reaction. So, from the dynamical data, it is possible to obtain information about the active site organization. We remind that the geminate recombination refers to the reaction of two transient species occurring before any separation by diffusion has occurred.

In the CO adduct of Mb, the Fe-C-O unit is oriented almost perpendicular to the heme

plane [61]. The dissociation of the ligand has been investigated by means of femtosecond time-resolved infrared and two trajectories have been individuate within a few hundreds femtoseconds that lead to CO located with opposite orientations. In both rotamers the CO axis ligand is roughly parallel to the heme plane [62]. Time-resolved X-ray crystallography reveals that the CO becomes temporarily ($\approx$ 200 ns) trapped in a so called "docking site" before escaping into the solvent or rebinding to the iron [63, 64]. This site is displaced about 2 Å from the active site and is considered as a mediator of the transport of the ligand to and from the bound position. In mammalian Mb, the highly conserved amino acid residues Val68, Ile107 and Leu29, in positions E11, G8 and B10 respectively, constitute the docking site. It has been shown [65] that the substitution of the latter with a phenylalanine strongly reduces the lifetime of the "docked" CO to $\approx$ 140 ps. Molecular dynamics simulation studies by Amadei, Di Nola and coworkers [66, 67] reveal the detailed kinetics of CO migration and binding in crystallized and solvated myoglobin. They show that the CO motion and the protein fluctuations are strictly correlated.

NO is more reactive towards heme than CO and its geminate recombination is observed in the picosecond timescale in sperm whale myoglobin and hemoglobin [68]. The kinetics of picosecond NO rebinding is found to be non-exponential and sensitive to the heme environment. Petrich *et al* [68] applied different functions to analyze the kinetic data: a bi-exponential decay function, a power law $\Delta A(t) = (1 + t/\tau_0)^{-n}$ and the expression $\Delta A(t) = exp[-\int_0^t k(t)dt]$. The latter equation corresponds to the possibility that the non-exponential behavior can arise from the time dependent evolution of the barrier for the rebinding process, while the power law can originate from the barrier distribution associated with different protein molecules (an inhomogeneous population). The authors show that the power law does not fit well the experimental profile, while the temporally distributed rebinding barrier model successfully reproduces the recombination data. These results support the interpretation of the complex rebinding behavior as arising from a homogeneous protein population with multiple binding sites, in which the barrier and the binding rate are altered by protein relaxation. The authors discuss the

Fe motion relative to the heme as the source of the time-dependent barrier. Moreover, they rationalize the observed ability of a double exponential decay to describe the data as due to a simplified approximation, limiting behavior of $k(t)$, to a complex rebinding process and they concluded that the out-of-plane configuration of the iron in respect to the macrocycle plane decreases the rate of geminate rebinding. They interpret the non-exponential rebinding kinetics to the modulation of the Fe heme distance that takes place in the same timescale, in which the proximal histidine assumes the control role.

Recently, it has been argued that the distal environment influences the kinetics of the ligand rebinding much more than the proximal effect. A growing body of data are recorded for the picosecond NO geminate rebinding process of wild-type leghemoglobin and six of its mutant proteins at the distal amino acid residues [69]. The results suggest that the distal barrier hinders the ligand from reorienting or diffusing far from the heme thus affecting the geminate rebinding path. If the rate of geminate ligand rebinding is enhanced, it must be because the barrier to ligand diffusion away from the heme has increased (closing in the heme pocket), and vice versa. In addition, slow geminate rebinding may be the result of the stabilization of the ligand by interaction with amino acids in the pocket, as happens in the CO docking site in Mb. The distal barrier clearly depends on the enclosed amino acids residues and the trajectory of the dissociated ligand brings to collisions that vary with the motion fluctuations, thus influencing the rebinding kinetics. The statistical distribution of impact produces different trajectories resulting in an inhomogeneous component to the relaxation [70].

Although the geminate rebinding of NO with myoglobin is faster than those of O_2 and of CO [71], a picosecond geminate recombination dynamics can be found also in the CO complex of a few proteins. Time-resolved CO rebinding studies were performed in microperoxidase, which consists of a heme with a proximal histidine that is part of an 11-peptide fragment [72]. This peptide renders the prosthetic group soluble in water and, due to the fact that the peptide is not long enough to wrap around the heme, the photodissociated CO is exposed to disordered solvent and not to a highly organized docking site, as in Mb. The observed rebinding kinetics is not exponential, probably

because the solvent cage effect influences the process. In this paper a model for the CO trapped within the solvent cage surrounding the heme is formulated and a kinetic time constant of $k = (110\ \text{ps})^{-1}$ is estimated. It emerges that the rate of CO rebinding in this protein is much faster than in Mb; this suggests the idea that the presence of a docking site is responsible for the slow CO rebinding observed in most hemoproteins.

The geminate heme-CO recombination in proteins is unusual; a chemically modified form of cytochrome *c*, termed carboxymethyl cytochrome *c* (cm cyt. *c*), is an example in which the recombination of CO is multiphasic with time constant of 16 ps, 120 ps and 1 ns [73]. The authors attributed these three phases to CO rebinding from different locations from within the distal pocket region. The high efficiency of the CO rebinding was seen as the consequence of a sterically hindered "caged" nature of the distal heme pocket from which it is difficult for CO to escape. It seems that the protein does not possess a ligand exchange pathway, in fact in cytochrome *c* the heme group is surrounded by a hydrophobic, structurally rigid pocket in which the interactions are weak. This configuration assures the restraint of the reorganization energy of the active heme environment, that guarantees the efficient electron transfer process. On the other hand, a structural flexibility of the protein chain is required in protein where the ligand transfer role is essential. Picosecond geminate recombination of CO to heme has been noted also in mutant forms of cytochrome *c* [74].

An intriguing structural feature for studying the ligand entry/escape dynamics to the active site (heme) is found in the recently discovered truncated hemoglobins. In the distal site of the heme pocket, the ensemble of polar residues are in contact with the iron-bound ligand coordination shell (see Fig.1.3). Spectroscopic properties of CO in different wild-type and mutant adducts reveal that the oxygen atom of the heme-bound CO could be H-bonded to the indole nitrogen of tryptophan, the hydroxyl of tyrosine or the NH_2 group of glutamine. This common pattern has been defined "*ligand inclusive hydrogen bond network*" [75, 76] and may represent a considerable barrier to ligand entrance and escape.

Chapter 2

Spectroscopic techniques

2.1 Transient absorption spectroscopy

2.1.1 Basic principles

Transient absorption spectroscopy (TAS) is an optical pump-probe time-resolved technique. In general, pump-probe experiments are used to investigate the nature and the evolution of the excited states of molecular species in study. In a transient absorption experiments, a short laser pulse, called pump (or excitation) pulse, excites the molecules, bringing them to the electronic excited state of interest. The time evolution of the excited state is monitored by a second broad UV-visible continuum pulse, i.e. the probe pulse, that is delayed in time in respect to the pump. The change in the sample absorbance ΔA before and after the excitation is the physical quantity that one wants to measure. A pump-probe pulse sequence allows to obtain an excited state absorption spectrum at a certain delay time. By repeating this sequence as a function of the pump-probe delay, it is possible to obtain the dynamical evolution (kinetics) of the transient absorption signal.

2.1.2 Instrumental apparatus

The experimental set-up is sketched in Fig.2.1. The most critical part of the pump-probe equipment is the source of pulses. Indeed, it must generate pulses short enough to

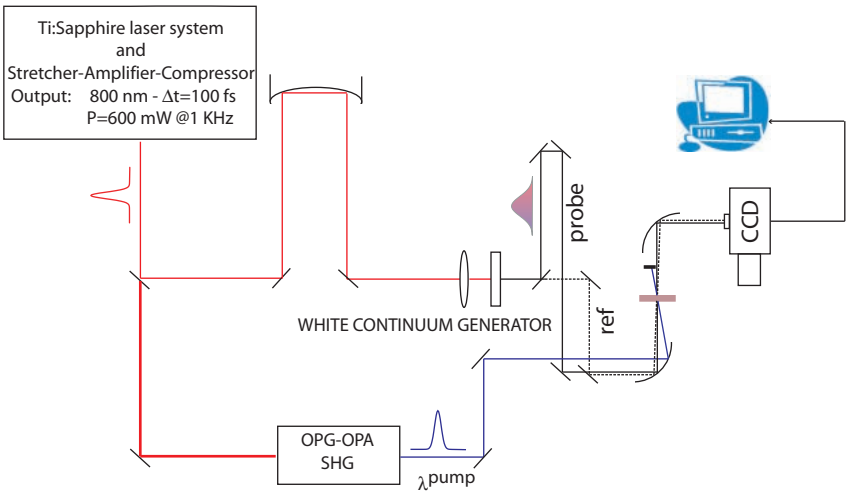

Figure 2.1: The femtosecond pump-probe spectrometer.

ensure an adequate time resolution, with an high peak power that allows to tune their frequency by means of parametric amplification. The system is based on a self-mode-locked Ti:sapphire laser (Spectra Physics, Tsunami), pumped by an intracavity frequency doubled cw Nd:YVO laser (Spectra Physics, Millennia). The pulses (800 nm, $\approx$ 70 fs, 82 MHz) emitted by the main oscillator are stretched, amplified and recompressed by a regenerative amplifier (BMI Alpha 1000) to give amplified pulses of $\approx$ 100 fs, with an average power of $\approx$ 600 mW at 1 KHz repetition rate. The pulse train is divided into two portions of unequal intensity ($\approx$ 95/5).

The more intense one is used to produce the excitation beam. Pump beams at 400 nm and 266 nm are obtained, respectively, by second and third harmonic generation from the fundamental pulses at 800 nm. Additional tunability is obtained by pumping a parametric amplifier, the TOPAS (Travelling-wave Optical Parametric Amplifier of Super-fluorescence) [77, 78]. The parametric amplifier generates two pulses at different frequencies, the signal and the idler, that are continuously tunable from roughly 1100

to 1600 nm and from 1600 to 2400 nm, respectively. The frequencies of signal and idler are determined by the phase-matching angle of the BBO crystal. As most electronic transitions are in the UV-vis spectral range, signal and idler can be doubled or combined with the fundamental, to obtain pump pulses from 800 up to 240 nm. The basic principles for obtaining the multiple output wavelengths required for the excitation beam are well known and fully described in the ref.[79]. In the experimental section relative to each sample taken into account in this work, the experimental conditions are reported.

The weakest portion of light, 1-2 mW, is focused on a CaF_2 plate to produce spectrally broad ("white continuum"), i.e., containing all wavelengths between 350 and 650 nm. The exact wavelength range depends on the specifications of the white light generation. In alternative, by replacing calcium fluorite plate with sapphire, the near infrared components of the probe spectrum (approximately until 1000 nm) become accessible, to the detriment of the blue side. However, this configuration is not adopted for the measurements reported in this thesis.
The white continuum beam is further split by a 50/50 beam splitter into probe and reference beams. The former reaches the sample with a variable delay from the excitation pulse, thanks to a suitable optical delay line, while the latter travels along a shorter path and always strikes the sample before the excitation. The reference beam provides a convenient normalization function for the transient spectrum, significantly increasing the signal to noise (S/N) ratio. The delay of the probe in respect to the pump pulse is determined by the distance travelled in the optical delay line, with a minimum step of 30 μm, corresponding to 100 fs.

The three linearly polarized beams are focused onto the same point of the solution by means of a parabolic mirror in a quasi-collinear geometry. The relative pump-probe polarization angle is set to 54.7° with the purpose of excluding rotational contributions to the transient signal. The sample is contained in a 2 mm thick quartz cell and is kept under continuous stirring by means of a small magnet. In order to minimize spurious photochemical effects, the repetition rate of the laser is reduced to 100 Hz by placing a mechanical chopper in the path of the main pulse train.

The experiments discussed in this thesis were performed with two different detection techniques. For the measurements of porphyrins (Chapter 3), the *deoxy* species and the CO adduct of flavohemoglobin from *E.coli* (Chapter 5), the dispersion and detection elements consisted of a single 25 cm Czerny-Turner monochromator (Chromex 250) and a coupled back-illuminated CCD camera (Princeton Instruments; response spectral range 300−1000 nm). The other measurements (Chapter 4 and ferric samples of HMP in the Chapter 5) were done by means of a Hamamatsu double linear array CCD, coupled to a spectrograph (Jobin Yvon CP 140-1824) and controlled by a home-made front-end circuit. The signals were fed into a simultaneous analog-to-digital conversion board (Adlink DAQ2010) and data acquisition was done by means of a LabVIEW computer program[1]. This second detection system gives some disadvantages as to the spectral resolution, but it allows to record spectra with better signal to noise ratio in a very short time.

2.1.3 Measurements of time resolved spectra

Transient absorption spectroscopy is commonly used to monitor the change of absorbance spectrum following the photoexcitation of molecules. The quantity of interest can be extract from the signal according to the following equation:

$$\Delta A(\lambda, \tau) = -log(T(\lambda, \tau)) \tag{2.1}$$

where $T(\lambda, \tau)$ is the photoinduced or transient transmittance. Similarly to the static transmittance, the transient one is defined as the ratio of the intensity of the probe beam recorded with $I(\lambda, \tau)$ and without $I_0(\lambda)$ the pump pulse and can be calculated by:

$$T(\lambda, \tau) = \frac{I(\lambda, \tau)}{I_r(\lambda)} \cdot \frac{I_r(\lambda)}{I_0(\lambda)} \tag{2.2}$$

The intensity of the probe is always divided to the intensity $I_r(\lambda)$ of the reference beam, that always interacts with the sample before the excitation process. The last

[1]The acquisition program was written by Dr Laura Bussotti, while the front-end was developed by Prof. Marco Prevedelli in collaboration with the electronic workshop at LENS.

factor is the ratio between the intensities of the two beams without the excitation pulse, i.e. the *baseline*.

Irrespective of what detector is in use, both probe and reference beams are spread in wavelength after the dispersion element and a multichannel detection is achieved, so that the intensity profile of the probe $I_p(\lambda)$ and of the reference $I_r(\lambda)$ can be obtained at a given delay time.

In practice, each transient spectrum is acquired in three steps. Shutters are used to orderly block and unblock the pump and probe beams in a sequential exposition of the events. This procedure allows to subtract the scattered light contribution from the overall signal.

1. $I_p + F_p$, $I_r + F_r$; with both pump and white continuum pulses
2. I_p^0, I_r^0; with only the white continuum passing through the sample
3. F_p, F_r; with only the pump

The commas separate the contributions of the two channels. Let F_p and F_r indicate the amount of spurious light seen by the detector superimposed to the probe and reference beam, respectively, i.e. all the fluorescence and scattered light that depends only on the pump and therefore that must be eliminate. This contribution is recorded, then subtracted from the intensity obtained when both pump and probe pulses impinge on the sample. So the calculation of transient transmittance at a given delay time between pump and probe is obtained by applying equation 2.3:

$$T(\lambda,\tau) = \frac{[I_p(\lambda,\tau) + F_p(\lambda)] - F_p(\lambda)}{[I_r(\lambda) + F_r(\lambda)] - F_r(\lambda)} \cdot \frac{I_r^0(\lambda)}{I_p^0(\lambda)} \tag{2.3}$$

First of all, the *baseline* is acquired to correct any mismatch between the two channels. Indeed, the spectral contents of probe and reference, which are the reflected and the transmitted components of the white continuum by a beam splitter, are never exactly the same. This fact makes unreliable the simple ratio for the $T(\lambda,\tau)$ estimation. It is striking to frequently check the stability of the *baseline*, the flatness and the point to point intensity fluctuations determine the sensitivity of the detection system. We

generally observe that 1000 shots are sufficient to produce a baseline which is flat within a variation of absorbance (ΔA) of $\pm$ 0.002.

After the measurements are carried out for several pump-probe delay times, the data can be collected in a two dimensional array, which provides both spectral and dynamical information.

In general, transient absorbtion spectra arise from three different contributions: excited state absorption (ESA), stimulated emission (SE) and bleaching (B).

ESA is associated with the decrease of $I(\lambda, \tau)$ with respect to the incident intensity $I_0(\lambda)$ and therefore with positive transient absorbances, $\Delta A(\lambda, \tau) > 0$. Conversely, SE and B correspond to the condition $I(\lambda, \tau) > I_0(\lambda)$ and therefore to $\Delta A(\lambda, \tau) < 0$. Notice that the former two features provide information about the excited states, while the latter is the component associated to the ground state depletion. Such spectral signal appears in correspondence to the steady-state absorption transitions and points out the ground state recovery time. Moreover, the bleaching intensity of the transient spectrum can be useful as an internal reference to estimate excited state oscillator strengths. When the excitation of sample raises the photoinduced reaction, an absorbtion band ($\Delta A(\lambda, \tau) > 0$) from the ground state of the product might be observed in the transient spectrum, i.e. this transient signal is not related to the excited state, but simply to a different chemical species. For this reason, it is called antibleaching (AB), instead of ESA.

2.1.4 Experimental related aspect and data handling

By using white continuum pulse as a probe, we are able to record at once a broad range of wavelengths. In practice, the wavelengths composing such a pulse are affected by a significant positive chirp due to group velocity dispersion (GVD). A detailed discussion of this effect can be found in reference [80]. The GVD effect influences the recorded spectral features; a possible method to limit such an inconvenience is to reduce the total amount of optical materials introduced into the beam path. However, for the analysis of the spectra in the first picosecond it is necessary to correct for the spectral artifact produced by this effect. The red components of the white continuum speed over the blue components, so

that probing in the two visible regions does not occur at the same delay time. Figure 2.2A shows the TA spectral evolution due to the white light dispersion. It should be noted that the signals evolve from left to right, i.e. from the blue to the red side of the spectra. This evolution has nothing to do with any of the molecular processes occurring after the excitation and can be numerically corrected. In order to better discriminate between this contribution and the transient signal of interest, we quantitatively determined the GVD contribution as a function of the wavelength measuring the optical Kerr effect (OKE) on the solution with heterodyne detection, as already reported [79]. Accordingly, the transient spectra measured in the first picoseconds were reconstructed with the help of a home-made correction program. The experimental signal onset times standing between the spectral range of each probe wavelength are translated in accord to the dispersion curve obtained from the OKE measurements, expressed by the following equation.

$$\tau(\lambda) = 0.0066 + 0.010 \cdot \lambda - 4.2 \cdot 10^{-5} \cdot \lambda^2 + 9.9 \cdot 10^{-8} \cdot \lambda^3 - 9.7 \cdot 10^{-11} \cdot \lambda^4 \qquad (2.4)$$

The result is shown in figure 2.2B.

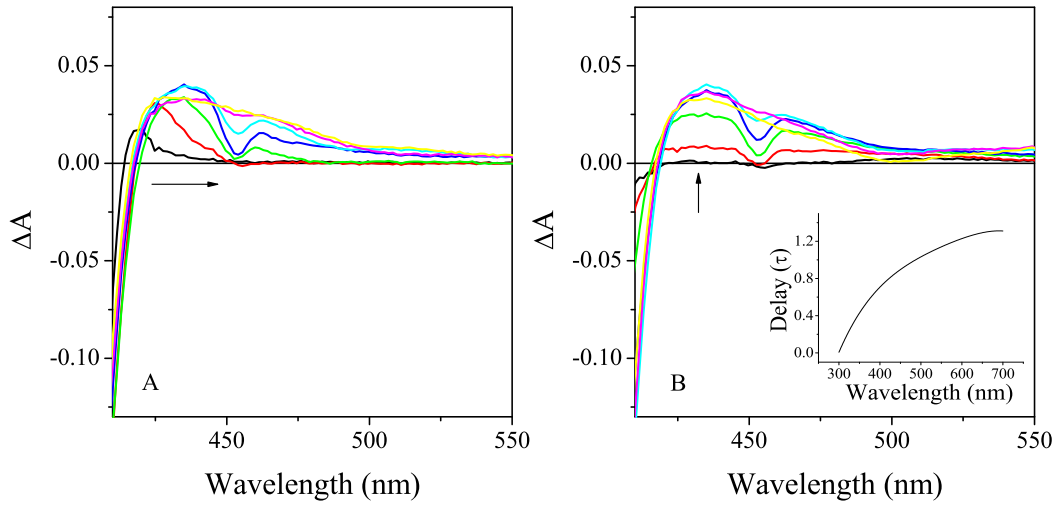

Figure 2.2: TA spectra evolution of met-Mb at shorter delays. The artifact due to the white dispersion follows a spectral evolution that obscures the short-time (hundreds of fs) transient absorption behavior. The experimental data (panel A) are compared to TA spectra after the dispersion compensation (panel B). The dispersion curve calculated according to Eq.2.4 is also displayed in the inset. The narrow band at roughly 460 nm is the stimulated Raman gain (SRG) signal.

Transient absorption spectra can be examined by different methods. Kinetics are plotted at any given wavelength to obtain the time course of the spectral features of interest. In addition, single value decomposition SVD can be practised to extract the spectra of the kinetic components, trying benefit from the global analysis. When a large time-wavelength data set is available, it would be convenient to analyze all of them together. The SVD analysis has been widely used in many scientific fields [81]; in particular this approach is applied in many publications concerning the recombination kinetics in proteins at different time regimes. SVD is a factorization procedure that reduces the data matrix to a series of orthogonal basis components. If $A(\lambda, t)$ is an mxn matrix then the SVD returns three matrixes, as below:

$$A(\lambda, \tau) = USV^T \tag{2.5}$$

where U is an $m - by - m$ matrix, the matrix S is $m - by - n$ with nonnegative numbers on the diagonal (as defined for a rectangular matrix) and zeros off the diagonal, and V denotes an $n - by - n$ matrix. U contains a set of orthonormal "output" basis vectors, i.e. basis spectra as a function of λ. Associated with each basis is a eigenvalue in the diagonal matrix S, so that each diagonal element can be considered as scalar "gain" by which each corresponding input is multiplied to give a corresponding output. The orthonormal "input" or "analyzing" basis vectors are enclosed in matrix V and the rows of the transpose V^T express the time course of the spectra basis. The number of components that one have to consider is determined by the weight in the S eigenvalue matrix. If the single value component, scaled according to its respective singular value, is comparable with the experimental noise, then the component will be neglected.

2.1.5 SVD in the analysis of CO recombination in Mb

In order to better explain the SVD analysis, we describe the handling of data recorded in photolysis experiments of the myoglobin CO adduct. These measurements have constituted a test to find the experimental conditions for the highest sensitivity and have been performed with the aim to reproduce previously reported results [44, 45, 48]. The

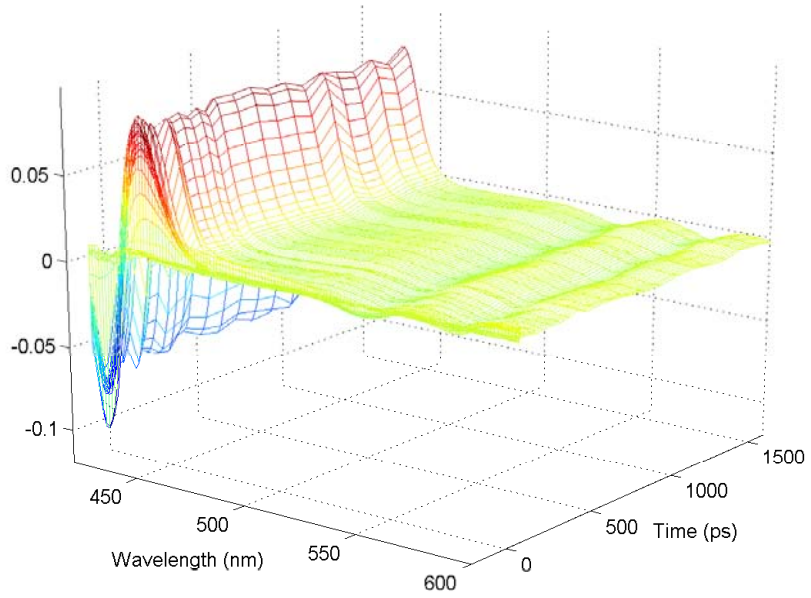

Figure 2.3: 3D plot of transient absorption spectra of MbCO, excited at 400 nm (E=0.6 μJ/pulse). The absorbance of the sample is adjusted in order to obtain an absorbance of 1.4 at the Soret maximum ($\lambda = 422$ nm).

Figure 2.3 shows a tri-dimensional plot of ΔA as a function of the delay time and the wavelength. Before performing the SVD analysis, the spectral distortion due to GVD must be corrected and the data are collected in matrix $A(\lambda, t)$. As we have seen in the previous subsection, SVD decomposes the original data into three matrices (U,S,V), reducing the whole set of spectra to a limited number of orthogonal basis components. The number of the significative basis spectra is determined by the weight of the elements in the matrix S. The singular values of the first eight SVD components of matrix A are reported in the table in Figure 2.4, where we display the spectra corresponding to the three major SVD components, scaled according to the respective singular values.

As the third component has little or no spectral features, we can confidently assess that the next fourth component is negligible. As an indicative general rule, our experience suggests to consider only the components whose singular values are greater than 10% of the first element S_{11}. So, the non-negligible N columns (in this case, $N = 3$) of the V matrix are multiplied by their respective singular values (SV) and simultaneously fit to

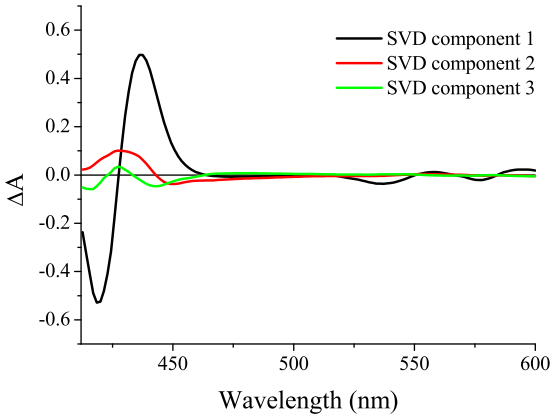

Component i	Singular Value S_{ii}
1	1.9051
2	0.3535
3	0.1935
4	0.1062
5	0.0608
6	0.0416
7	0.0355
8	0.0182

Figure 2.4: Spectra of SVD components of MbCO data. The ΔA values are scaled according to the singular value reported in the table.

a sum of M exponentials.

$$SV_N(t) = \sum_{m=1}^{M} C_{nm} \cdot e^{-t/\tau_m} \tag{2.6}$$

The resulting kinetic profiles are shown in Figure 2.5. M is the minimum number of time constants necessary to globally fit all the N SVD components. The parameters are given in Table 2.1.

The spectral basis and the correspondent time course vectors have not a physical meaning, but for each decay it is possible to construct the associated spectra (DAS). By the following equation:

$$DAS_m(\lambda) = \sum_{n=1}^{N} C_{nm} \cdot U_n(\lambda) \tag{2.7}$$

the spectrum associated to each of the m exponential components is obtained from a set

Table 2.1: Parameters for simultaneous fit of time course SVD components to a biexponential model including a constant contribution.

	300 ± 100 fs	3.1 ± 0.8 ps	constant
SV_1	-0.11	0.04	0.26
SV_2	-0.18	-0.08	0.03
SV_3	0.18	-0.05	0.004

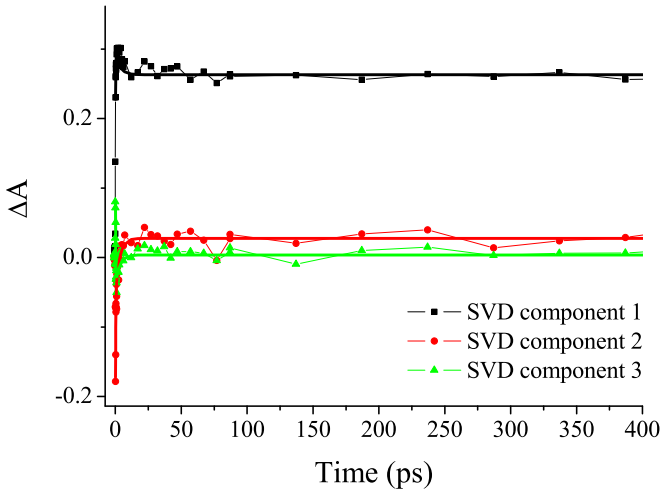

Figure 2.5: Time courses of the SVD components of MbCO data. The ΔA values are scaled according to the singular value reported in the table in Figure 2.4.

of N coefficients C_{nm}.

The decay profiles SV are analyzed starting from 150-200 fs. In fact, an artifact due to the cross-phase modulation (XPM) [82] is generally superimposed to the signal in correspondence of the temporal coincidence between pump and probe and forbids to properly separate the different contributions in the first two hundreds femtoseconds.

From our analysis, two time constants including a baseline (constant component) are obtained and the corresponding DAS are shown in Figure 2.6.

The 240 fs exponential component is associated to a broad signal with a maximum around 480 nm and to the bleaching of the *deoxy* Mb. This spectrum is in agreement with recently reported results for hemoglobin [45] and can be attributed to the transient absorption from the CT state of the pentacoordinated species. The spectral component associated to the decay time $\tau_2 = 3.1$ ps resembles the first derivative of the Soret absorption band in the *deoxy* Mb, a signature of the band spectral shift. We observe that the zero crossing is at 434 nm, corresponding to the peak of the *deoxy* Soret band. The time associated to such a DAS gives the time dependence of the band shift, that can be related to the vibrational relaxation of the hot pentacoordinated ground state. Finally, the origin of third DAS ban be easily understood considering the spectral time

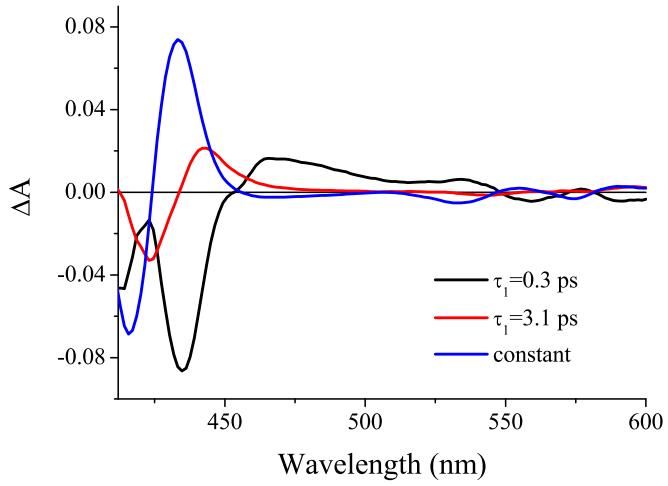

Figure 2.6: Spectral components of the three time contributions to the transient absorption signal in MbCO.

evolution. It is remarkable that the measured signals change in the first picoseconds following the photodetachment, until the transient absorption spectrum coincides with properly scaled steady-state difference absorption spectrum *deoxy* Mb - MbCO. This evidence means that the photoexcited heme has reached a new equilibrium configuration: the five-coordinated high spin *deoxy* Mb in the ground electronic state. Similarly, the kinetics profiles extracted from the spectra at different wavelengths show a plateau at long delay time (data not shown). The plateau (or baseline) is fitted with the constant background added to the biexponential decay model and indicates the absence of any geminate recombination on short timescales. The spectrum associated with the long time signal, is the third DAS (blue line in Figure 2.6) that corresponds very well to the static difference spectrum.

2.1.6 Measurements of kinetic profiles

The decay curves in correspondence of specific wavelengths have been determined following two different sampling procedures. In the simplest one, excited state absorbances at a given wavelength are extracted from the limited number of transient absorption spectra actually measured. In the second a higher sensitivity is achieved (a) by increasing the

repetition rate of the laser pulses and lowering the intensity of the pump, and (b) by making use of lock-in detection techniques. In this scheme, the wavelengths are selected placing different interference filters (FWHM $\approx$ 20 nm) onto the probe beam path beyond the sample cell and detecting the probe intensity with a silicon double-photodiode. A lock-in amplifier synchronized with a mechanical chopper operating at 500 Hz alternatively blocks every second pumpe pulse of the 1 KHz train and amplifies the probe signal when the excitation pulse is switched on. The relaxation dynamics is sampled with variable time steps starting from 50 fs in the first picosecond interval and ending to 1 ps in the interval 20-50 ps, so that the number o the points in a given time interval is approximately constant. Increasing the delay, larger time steps were chosen between 500 and 1500 ps. Due to the higher number of sampling points the second procedure described here was preferred to the first one, except for the measurements of hemoglobin from *Thermobifida fusca* and ferric HMP (flavohemoglobin of *E.coli*). The small quantities available for these samples made impossible to prepare freshly solution for both the experimental configurations. The decay curves measured in the two cases have been found to be essentially coincident.

The relaxation kinetics has been studied on the basis of the following expression

$$\Delta A(\tau, \lambda) = \int_{-\infty}^{+\infty} g[(t-\tau), \lambda] R(t, \lambda) dt$$

where the transient absorbance at the selected wavelength results from the convolution of the instrumental function $g[(t-\tau), \lambda]$ with the molecular response function $R(t, \lambda)$. The latter is further expanded in terms of exponential contributions as $R(t, \lambda) = \sum_i A_i(\lambda) \exp(-t/\tau_i)$, each component of which is characterized by the amplitude A_i and lifetime τ_i.

2.1.7 The instrumental function

For a faithful deconvolution of the kinetic profiles, the knowledge of the instrumental function is indispensable. The instrumental function is defined as cross-correlation between pump and probe pulses. However, in order to determine the "real" function, a

suitable experiment should be designed, whilst using the same sample cell in the identical conditions (angle between pump and probe and their diameters, for example) used for the actual measurements. As this is often difficult to obtain, in practice the instantaneous signals appearing in transient absorption spectra can be conveniently utilized [83]. These signals include two-photon absorption (TPA), stimulated Raman gain (SRG) and cross-phase modulation (XPM). TPA and SRG are non-linear effects produced by the short laser pulses with very high pump power density, while the XPM arises from the temporal chirp of the continuum white probe [82]. The temporal envelope of these signals reproduces the pump-probe cross-correlation function, $g(t) = \int I_{pump}(t')I_{probe}(t'+t)dt'$.

In particular, in most cases we determined the instrumental function by measuring the time profile of stimulated gain of the most intense Raman bands of the solvent. For a qualitative description of this phenomenon, we can assume that two photons of appropriate frequencies, spatially overlapped and coincident in time, impinge onto the sample. When the excitation frequency is close to a specific component of the probing white continuum, the emission of a third photon can be stimulated. The stimulated gain energy corresponds to the difference between the molecular ground state and a virtual energy level through which the pump photons are scattered and it is specific for each medium. The Raman wavelength λ_{SRG} and the pump wavelength λ_{EXC} can be related by means of the following expression:

$$\frac{1}{\lambda_{EXC}} - \frac{1}{\lambda_{SRG}} = \nu \cdot 10^{-7} \tag{2.8}$$

The wavelengths must be expressed in nm, while ν, that is the frequency of an active Raman transition of the molecular system, is in cm^{-1}. SRG does not contain any relevant information about the sample; nonetheless, the plot of the intensity of the Raman signal *vs* the delay time (see fig. 2.7) gives the pump-probe cross-correlation function. Figure 2.7 shows a typical cross-correlation function obtained by this method: the time profile is Gaussian, with a full width half maximum (FWHM) of $= 160 \pm 10$ fs.

This method allows to measure the instrumental function, even if indirectly. The measure is accurate only if one refers to a probing wavelength near the Raman signal. As

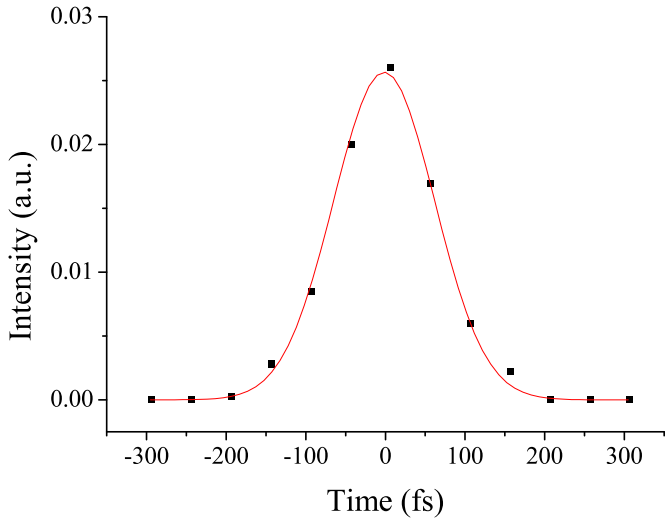

Figure 2.7: Intensity of the stimulated gain Raman signal *vs* the delay time between pump and probe pulses in water ($\lambda_{EXC} = 400$ nm; $\lambda_{SRG} \approx 460$ nm). The red line is the result of a Gaussian fit that provides the instrumental function with temporal width of FWHM $= 160 \pm 10$ fs.

a matter of fact, the temporal resolution is primarily determined by the pulse duration; however, the latter is not the only parameter that one should consider for the instrumental function evaluation. There is another effect that possibly contributes to the broadening of the instrumental function. If the central wavelength of the pump and of the probe are different, the refractive index experienced by the two pulses inside the sample cell is different and hence there is a mismatch of the velocity (GVM) of the two pulses. In other words, the pump and probe pulses travel at different speeds in the medium, and the cross-correlation function broadens. In the case of Gaussian pulses, the instrumental function broadening due to GVM can be calculated from:

$$G(t) = \frac{c}{a\Delta n}\{erf[a(\tau + \frac{l}{c}\Delta n)] - erf(a\tau)\} \tag{2.9}$$

where Δn is the difference between the refractive indexes of the medium at the pump and probe wavelengths, l is the optical path (length of the interaction volume), $a = 2\sqrt{ln2/(\Delta\tau_{pump}^2 + \Delta\tau_{probe}^2)}$. $\Delta\tau$ indicates the duration of the pulses, i.e. their full width half maximum (FWHM).

The broadening effect described by Eq 2.9 is obviously dependent on the probe wave-

length. In our experiments we never observed any appreciable variation of the measured instrumental function with the probe wavelength. This leads us to conclude that the GVM effect although present, is small and approximatively constant through the entire probe wavelength range considered, at least for the limited path length of the pulses in our samples (tipically 1 mm). As a consequence we can avoid any further correction, and assume that the measured instrumental funcion contains also some average contribution of GVM.

2.2 Time-resolved fluorescence spectroscopy

The sample is excited by the tunable femtosecond pulses obtained from the laser apparatus described for TAS. The fluorescence is collected by a quartz lens and focussed onto the photocathode of a Hamamatsu R2809U-01 microchannel plate photomultiplier, after elimination of the excitation beam scattered radiation by means of an appropriate set of colored filters. The photomultiplier signal is fed into a digital oscilloscope (1.7 GHz band-pass) grounded through a 50 Ω resistor. The slightly asymmetric instrumental function, measured by light scattering from a latex solution, has a time duration (FWHM) of 550 ps, highly reproducible from one experiment to another. The experimental time profiles were deconvoluted taking into account the instrumental function and were fitted by exponential functions, obtaining intrinsic fluorescence lifetimes.

2.3 Steady state spectroscopy

The absorption spectra have been recorded by a Lambda 950 Perkin Elmer model spectrophotometer. The fluorescence spectra were measured by means of a Perkin -Elmer spectrophotofluorimeter (mod. LS55).

Chapter 3

Excited state dynamics of porphyrins

3.1 The relevance of porphyrins

Porphyrins are abundant in nature and they play important role in a large number of different biological occurring processes: oxygen transport and storage in aerobic organisms, electron transfer in the intracellular respiratory chain, electron and energy transfer in photosynthesis [31], for example. Besides they have been employed in the supramolecular light-harvesting assemblies in order to realize efficient photo-electron transfer systems [84, 85]. In material science [86–88], the extremely large nonlinear optical susceptibilities of porphyrin linear arrays and oligomers, obtained by clever combination of porphyrin moieties, are related, among other factors, to the high polarizability of these π-electron systems, i.e., to the whole set of their excited states. The photodynamic therapy is another important field of interest, it is worth recalling that hematoporphyrin in the lowest triplet state acts as a photosensitizer for the generation of excited singlet oxygen [89].

It is then conceivable that many studies have been performed on this subject. One point that clearly emerges is that porphyrins can coordinate several different metals through the four central nitrogens to form metal-porphyrins. Depending on the type of coordinated metal, new properties are introduced, concerning redox potentials, excited state energies and lifetimes.

Moreover, it has been observed that the ring conformation influences the rate constants of processes that are involved in the molecular functionality. Distorted porphyrins have been synthesized by crowding of substituents at the periphery of the macrocycle with the purpose of investigating how the conformational flexibility affects the photophysical properties of non-planar prosthetic groups [90, 91]. It was found that distorted porphyrins exhibit smaller fluorescence yields and larger shifts between absorption and fluorescence origins. The $S_1(\pi\pi*)$ lifetimes of distorted dodecaphenyl- and of tetra-tert-butylporphyrin at room temperature in nonpolar solvents are strongly reduced with respect to those of planar tetraphenyl- and octaethylporphyrin [92, 93]. Correspondingly, a model was proposed where the nonplanar macrocycle, following the photoexcitation and the increase of conformational freedom in the S_1 state, changes to funnel geometries where S_1 and S_0 are close in energy, thus enhancing the deactivation channel of internal conversion.

The correlation between conformational flexibility and photophysical properties in nonplanar porphyrinic prosthetic groups can be followed by studying an alternative but not less attractive systems: the diprotonated porphyrins. In this respect, some work on substituted nonplanar porphyrin diacids has already appeared. For instance, in diprotonated octaethylporphyrin (H_4OEP^{2+}) and tetraphenylporphyrin (H_4TPP^{2+}), the increase of the $S_1 \rightsquigarrow S_0$ nonradiative decay relative to the neutral species was observed [94]. It seems however that little attention has been devoted to the diprotonated species of unsubstituted porphyrin (H_4P^{2+}; **2** in Figure 3.1). MO/DF ab initio calculations [95, 96] and X-ray results on closely related systems [97] gave the common indication that the lowest ground state conformation is nonplanar, i.e., saddle-shaped with D_{2d} symmetry. Due to the absence of peripheral substituents, the molecular species **2** of Fig.3.1 is recommended for studying the effect of macrocycle nonplanarity.

In order to assess the effect of the conformational distortion in the H_4P^{2+} case, the comparison with suitable planar porphyrinic systems ("normal" according to a previous classification [92]) is considered. A straightforward choice might be the unsubstituted free base porphyrin or porphine in view of its overall photophysical behavior in the S_1

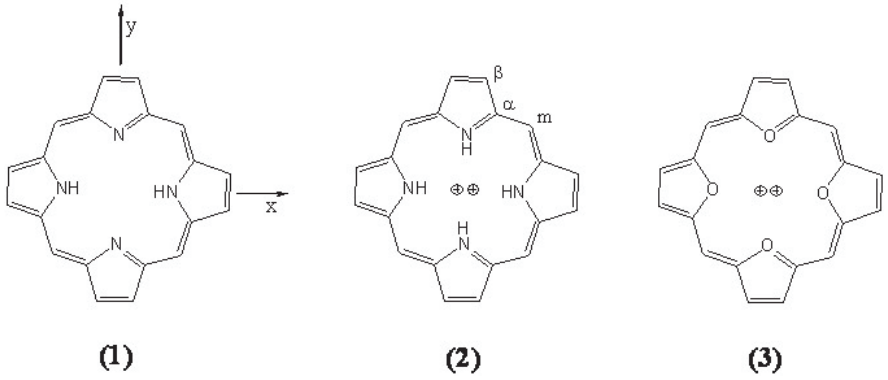

Figure 3.1: Molecular structures of porphine **1**, diprotonated porphyrin **2**, and tetraoxaporphyrin dication **3**. The reference system, common to the three species, is shown for convenience on **1**. The α, β, and *meso* positions are indicated on **2**.

state, including the negligible shift between absorption and fluorescence origins and the S_1 lifetime [98] which is in the range of those of essentially planar substituted porphyrins. However, this is arguable for states higher than S_1. In Figure 3.1 the basic structure of the porphine is indicated as **1** and constitutes the simplest molecule in the porphyrin-type family. It would be desirable to rely on a normal system with an energy diagram of the lowest $\pi\pi^*$ states paralleling as much as possible that of H_4P^{2+}. It luckily happens that tetraoxaporphyrin dication ($TOxP^{2+}$; **3** in Figure 3.1) fulfills this requirement and moreover shows strong fluorescence both from S_1 and S_2 states.

A detailed study of the stable conformations of these compounds was reported by Salvi *et al* [96]. Besides the vibrational frequencies of **1**, **2** and **3**, in this paper the stable geometries of D_{2h}, D_{2d} and D_{4h} symmetries, respectively, were calculated using the B3-LYP functional and cc-pVDZ basis set, obtaining an accurate assignment of the vibrational spectra.

Therefore, for the sake of acquiring a deeper knowledge of the fast/ultrafast processes in this thesis work, the photophysical properties of unsubstituted porphyrin (H_2P), diprotonated porphyrin (H_4P^{2+}), and isoelectronic tetraoxaporphyrin dication ($TOxP^{2+}$) have been studied in solution at room temperature by means of steady-state spectroscopic

techniques, transient absorption spectroscopy and time-resolved fluorescence.

3.2 Materials and methods

Porphine **1** (H_2P) was purchased from Frontier Scientific (USA) and used without further purification. The diprotonated species **2** (H_4P^{2+}) was obtained by addition of a small amount (5% in volume) of trifluoroacetic acid in porphine solution. The conversion form **1** to **2** species is quantitative. The tetraoxaporphyrin dication **3** has been kindly provided by Prof. E. Vogel (University of Köln, Germany) as perchlorate salt [99].

Solutions were freshly prepared using benzene as a solvent for **1** and **2**, and concentrated $HClO_4$ for **3**. The fluorescence spectra were taken with sample concentration in the range $10^{-4}-10^{-7}$ M, no difference has been noticed within the mentioned limits. The $S_1 \rightarrow S_0$ emission profile was corrected for the instrumental response. To this purpose, the fluorescence spectrum of Rhodamine 6G perchlorate ($c = 6 \times 10^{-4}$ M in ethanol) was compared with the reference spectrum [100], and the correction factor was applied at each wavelength.

The quantum yields were estimated by comparison with compounds of well-known quantum yield [101]. In order to avoid any inner filter effects, the absorbance was adjusted not to exceed 0.1 at the Soret maximum. 9-phenylanthracene (PA; $\Phi_{S_1 \rightarrow S_0} = 0.49$ in cyclohexane) and 9,10 diphenylanthracene (DPA; $\Phi_{S_1 \rightarrow S_0} = 1.0$ in cyclohexane) were used as standards. The integrated fluorescence intensities are linearly proportional to absorbances. With the same excitation wavelength and solvent, quantum yields are obtained from the the simple expression $(\Phi_A/\Phi_B) = (m_A/m_B)$ where A and B are the two compounds DPA and PA, and m_A and m_B are the slopes of tha A and B linear plots. Cross-calibration gives 0.52 for PA and 0.95 for DPA with quantum yield ratio independent of λ_{exc} in the range 325-365 nm. Transient absorption experiments are carried out with freshly prepared solutions using as solvent the benzene/ciclohexane (1:10) mixture for **1** and **2**, while the concentrated $HClO_4$ is invariant for **3**. The solvent combination with ciclohexane is suggested by the necessity of reducing to a negligible

level the undesired two-photon transient signal from benzene excited at 400 nm, yet maintaining the full solubility of the compound.

Time-resolved measurements have been performed exciting **1** at 400 nm and 490 nm, **2** at 400 nm and **3** at 370 nm. Pump and probe experiments were carried out in solutions whose concentration was adjusted such that the absorbance in a 2 mm thick cell was ≈ 0.8 at the exciting wavelength. In the case of **1**, for excitation at 490 nm and the same cell thickness the absorbance was set to ≈ 0.5. Freshly prepared samples were excited with pulse energy varying between 0.3 and 0.8 μJ, the transient signal was found to be proportional to the intensity of the pump pulse. The absorption spectra were measured before and after each experiment to check sample quality and stability.

The pump pulses at 400 nm were generated by frequency doubling the fundamental 800 nm radiation (for the details of the instrumental apparatus, see chapter 2). Whereas the 370 nm wavelength was obtained as fourth harmonic of the signal (1480 nm infrared beam generated in the BBO crystal). Signal pulses at 1265 nm were also produced and frequency-mixed with the fundamental ones (800 nm) to give the excitation pulses (0.3 μJ energy) at 490 nm. The optical generator and amplifier (OPG-OPA) allows to achieve the tunability of the excitation pulses by changing the phase-matching condition. Wavelengths at 544 and at 527 nm were also obtained as the fourth harmonic of the idler (FHI).

For the kinetic analysis, it is necessary to know the instrumental function. A Gaussian shaped cross-correlation function with temporal width (FWHM) 160 ± 10 fs was determined by SRG.

3.3 Steady-state results

The absorption and fluorescence spectra of diluted solutions ($c = 5 \times 10^{-6}$ M or less) are reported in Figure 3.2. The absorption spectra are discussed making reference to the well-known four-orbital model of porphyrins [31, 102]. Under D_{4h} symmetry for **3** and D_{2d} symmetry for the lowest energy conformation of **2** the two lowest excited states may

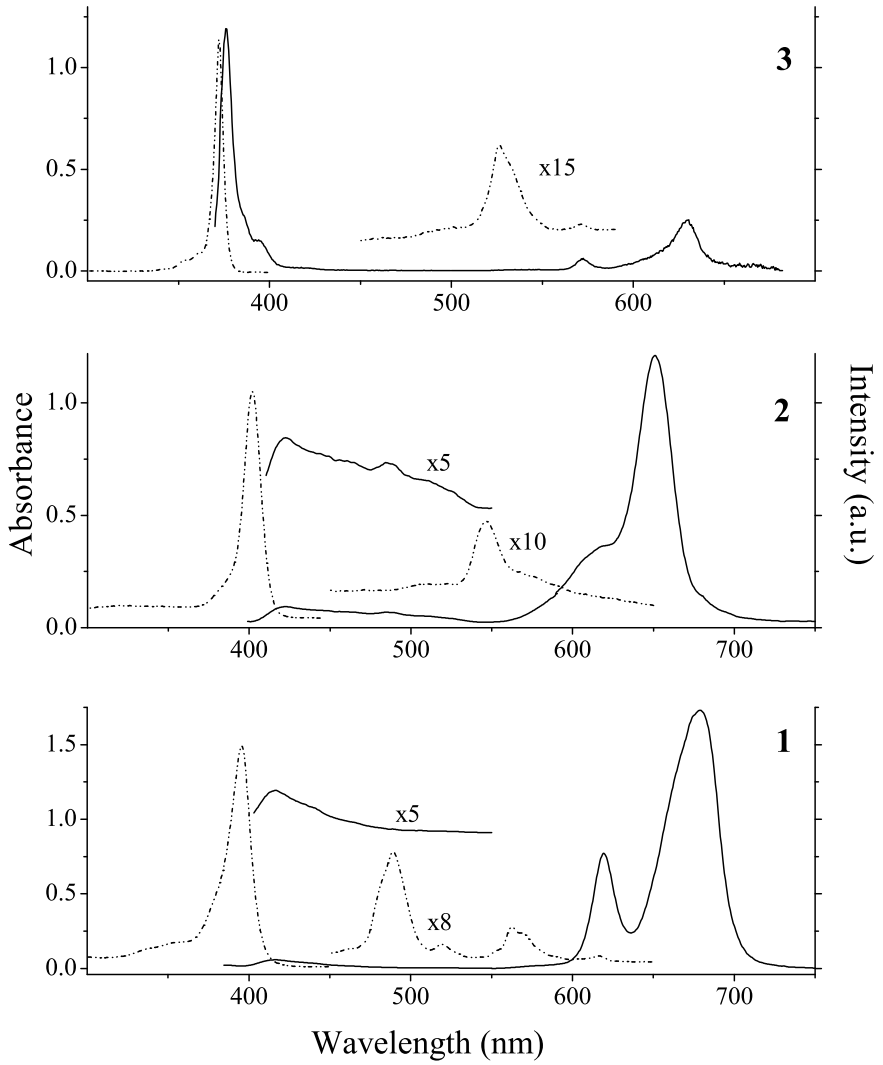

Figure 3.2: Absorption (long dash) and fluorescence (full line) spectra of porphine **1**, diprotonated porphyrin **2**, and tetraoxaporphyrin dication **3**. The absorbance scale is on the left and the fluorescence scale on the right. The excitation wavelengths of the fluorescence spectra are 350 nm for **1** and **2** and 365 nm for **3**.

be described as minus and plus combinations of excited configurations resulting from the promotion of one electron from the highest occupied molecular orbitals. The $S_0 \rightarrow S_1$ and $S_0 \rightarrow S_2$ transitions are allowed and give origin to the so-called Q and B (or Soret) bands, respectively. The first transition is weakly allowed because of the near equality of the transition moments from the ground to the two excited configurations, for the same reason the second transition is strongly allowed. Lowering the molecular symmetry to D_{2h} in **1** splits each of the two excited states into two components.

Details of the observed absorption spectra are added in the following subsection:

H*$_2$*P. The absorption spectrum of **1** was already discussed [103]. Four bands are expected, Q_x (B_{3u}); Q_y (B_{2u}) and B_x (B_{3u}); B_y (B_{2u}), although the splitting is observed only for Q_x; Q_y pair. Experimentally Q_x and Q_y are well separated with origin at 16205 cm^{-1} (617.0 nm) and at 19230 cm^{-1} (520.0 nm), respectively. The Q_x transition shows also two vibronic additions at 17590 and 17720 cm^{-1} (1385 and 1515 cm^{-1} from the origin), while only one intense vibronic transition is present above the origin of Q_y at 488 nm, assigned as 19230+1260 cm^{-1}. It borrows intensity much probably through electronic coupling. The strong B_x and B_y transitions are spectrally unresolved and give origin to an intense band with the maximum at 396 nm (25250 cm^{-1}) and width Γ (fwhh) $\approx$ 1070 cm^{-1}.

***H*$_4$*P*$^{2+}$**. Under D_{2d}, the absorption profile of **2** is expected consisting of Q and B band with highly different intensities, assigned as $A_1 \rightarrow E$ transitions [95, 96]. The Soret band is found at 402.0 nm (24875 cm^{-1}) with $\Gamma \approx$ 810 cm^{-1}. In the Q band region, a single peak is observed at 546.2 nm (18310 cm^{-1}) and a long unstructured tail extending beyond $\approx$ 600 nm.

***TOxP*$^{2+}$**. Under D_{4h}, the Q and B transitions present E_u symmetry. The electronic origin of the Q band is observed as a very weak peak at 571.5 nm (17495 cm^{-1}), whereas that of the B band shows prominently at 372.2 nm (26865 cm^{-1}) as a sharp peak with a remarkably low bandwidth, $\Gamma \approx$ 415

cm^{-1}. A vibronic band 1515 cm^{-1} above the Q origin is observed.

Going now to the fluorescence results, a very interesting $S_2 \rightarrow S_0$ emission is observed, much more intense for $TOxP^{2+}$ than for H_4P^{2+} and H_2P. The $S_2 \rightarrow S_0$ fluorescence spectra of **1-3** are collected in Figure 3.3.

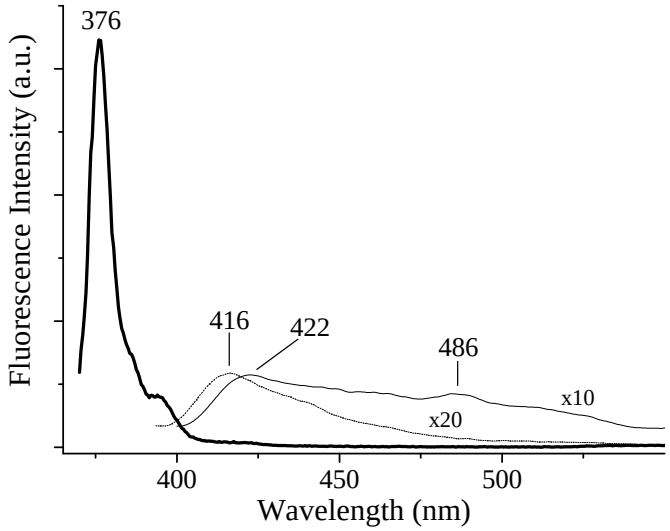

Figure 3.3: The $S_2 \rightarrow S_0$ fluorescence spectra of **1** (dotted line), **2** (thin line) and **3** (thick line).

In the tetraoxaporphyrin dication case, this fluorescence is extraordinarily sharp and reveals an excellent mirror symmetry in respect to the corresponding absorption (as showed in Fig.3.2). On the contrary, the fluorescence bands of the porphine and its dication are shifted and very much broadened in respect to their absorption counterparts.

In the red region of the porphine emission spectrum, reported in Fig.3.2, the intense and well-structured $Q_x \rightarrow S_0$ emission is evident. The origin (at 619.2 nm) is 55 cm^{-1} to the red of the absorption origin. An intense vibronic band is observed at $\approx$ 679.0 nm, 1420 cm^{-1} lower than the fluorescence origin. In the $S_1 \rightarrow S_0$ spectrum of diprotonated porphyrin a single strong band is seen at 651.0 nm (15360 cm^{-1}). In respect to the single absorbtion peak, an energy difference of 2950 cm^{-1} can be calculated and depends on the vibrational frequency of the excited mode in S_0 and S_1, as well as on the gap between the absorption and fluorescence origins. Thus, on this basis, no accurate estimate of the

Table 3.1: Summary of spectral and photophysical data of porphine (**1**), its dication (**2**) and tetraoxaporphyrin (**3**). $\Delta E_{abs/em}$ is the absorption/emission shift and η the fluorescence quantum yield value; τ_f and τ_R are the observed fluorescence lifetime and the calculated radiative lifetime, respectively. [a] From literature [98]. [b] Estimated from quantum yield measurements.

		$\Delta E_{abs/em}$ (cm^{-1})	η	τ_f (ns)	τ_R (ns)
1	Q_x	55	0.054^a	15.8	238
	B_x;B_y	1210			1.9
2	Q		0.046^a	5.5	133
	B	1205	$5.6\times10^{-4\,a}$	$1.5\times10^{-4\,b}$	2.6
3	Q	15	0.11	7.3	100
	B	285	0.035	$\leq$0.1;0.04^b	1.1

absorption/emission shift can be given. On the contrary, regarding the S_2 state, the absorption/emission shift is 1205 cm^{-1}, very similar to that of porphine. A very small shift (15 cm^{-1}) is found in the Q fluorescence of the tetraoxaporphyrin dication. The spectral and photophysical data are summarized in Table 3.1, where also the fluorescence quantum yields are reported. It is found that the $S_2 \rightarrow S_0$ fluorescence quantum yield of tetraoxaporphyrin is surprisingly high ($\eta_{S_2} = 0.035$), 2−3 order of magnitude more than the values in some metalloporphyrins. From this knowledge and the estimation of the S_2 (or B) radiative lifetime by the Strickler and Berg relation [104] (≈1.1 ns), it is possible to calculate the fluorescence lifetime $\tau_{S_2} = \eta_{S_2}\times\tau_{R,S_2} \approx 40$ ps. For the sake of completeness the quantum yield measurements have been extended to S_1 ($\eta_{S_1} = 0.11$).

The same consideration for **2** give a value of ≈150 fs for τ_{S_2}.

3.4 Time-resolved results

3.4.1 Fluorescence lifetimes

The time profiles of the B and Q fluorescence of species **2** and **3** have been measured and are shown in Figure 3.4.

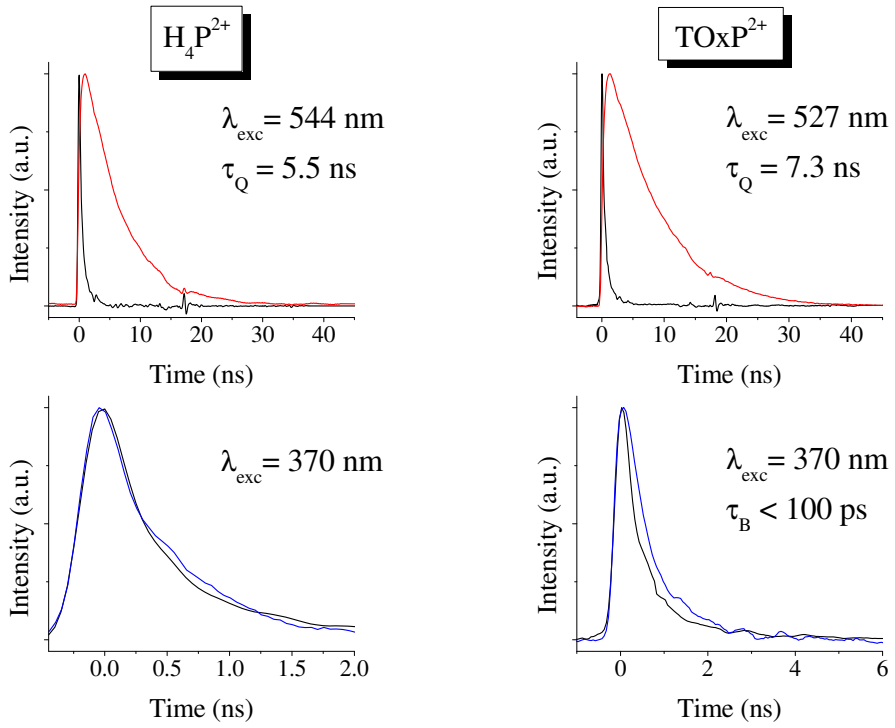

Figure 3.4: Observed decay profiles for the $S_1 \rightarrow S_0$ (top, red line) and $S_2 \rightarrow S_0$ (botton, blue line) fluorescence of H_4P^{2+} (left side) and $TOxP^{2+}$ (right side). The instrumental function (full black line) is also shown in the figure.

The Q fluorescence profiles of the porphyrin dication (**2**, H_4P^{2+}) is monoexponential with a time constant of 5.5 ns, independently from the excitation wavelength, 544 and 370 nm and from the purging process by pure nitrogen. Considering this result with quantum yield, η=0.046 [98], the radiative lifetime is calculated to be ≈120 ns, which compares satisfactorily with the value of 133 ns derived from Strickler and Berg relation [104]. On the contrary, the B fluorescence decay overlaps with the instrumental line shape.

From the Q fluorescence decay of the tetraoxaporphyrin (**3**, $TOxP^{2+}$), we obtained a lifetime of 7.3 ns. The S_1 lifetime is substantially the same (7.2 ns) when the excitation is at 370 nm. The B fluorescence profile evolves in a time interval comparable to that of the instrumental function and cannot be determined with good accuracy even applying a deconvolution procedure. In any case a reasonable upper limit of ≈100 ps may be set for S_2 lifetime.

The porphine (**1**) is excited in the Soret and Q bands. Only the fluorescence from S_1 is detected. The estimated time constant is 10.7 ns in aerated solutions and 15.8 ns after deoxygenation, in good agreement with the reported value [98]. Contrary to the other two molecules, a variation between aerated and N2-purged solutions is observed.

3.4.2 Transient absorption data

Porphine. The transient spectra of **1** were measured in the time interval 0−1.5 ns, following the B band excitation (400 nm) as well as the Q_y band excitation at 490 nm. The transient spectra in the range 405-600 nm and the spectral dynamics are rather complex. The time evolution of these spectra is shown in Figure 3.5. The negative absorbances are assigned as bleachings of the Q_x and Q_y bands, except for the signal at about 450 nm that disappears within 200 fs and is due to the SRG of the solvent.

A very broad ESA band appears simultaneously with the excitation (within the instrument function). This signal is strongly distorted due to the overlap with the solvent Raman peak and the B signal at 488 nm. In spite of the spectral congestion, it is clear that the ESA band undergoes spectral transformation even on a very short timescale

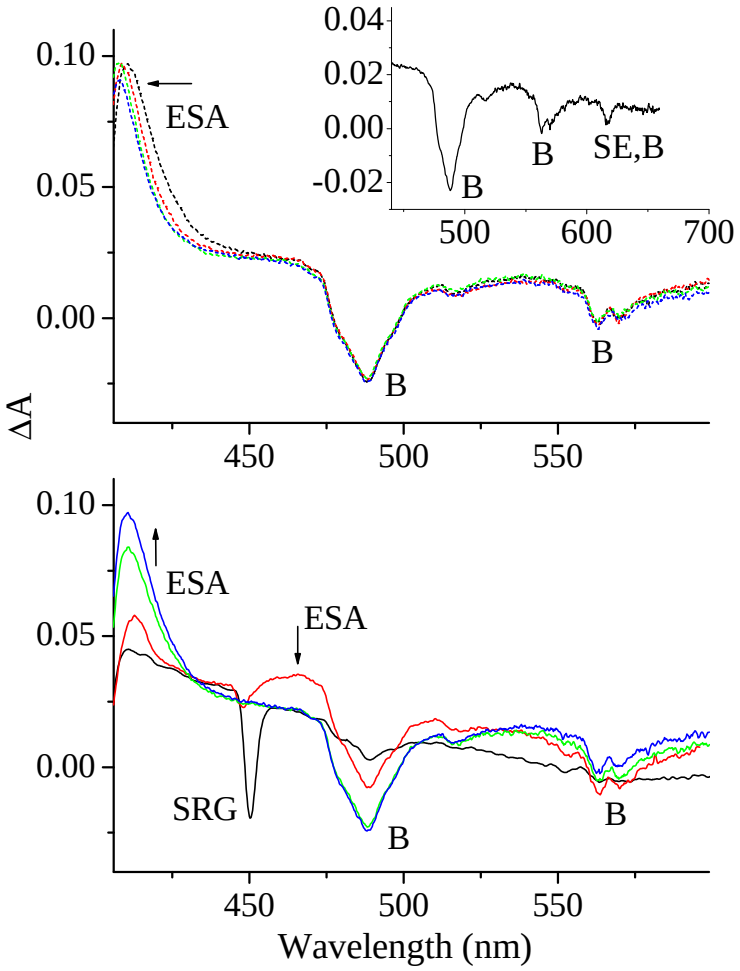

Figure 3.5: Transient absorption spectra of **1** in benzene/cyclohexane 1:10 solution (c = 3×10^{-5} M), exciting at 400 nm, at selected delay times. The ESA, SRG, B and SE symbols identify transient bands due to excited-state absorption, stimulated Raman gain of the solvent, bleaching and simulated emission, respectively. In the *lower panel*, the transient spectra in the first 5 ps are shown: temporal coincidence between pump and probe pulses (black solid line), at 200 fs (red solid line), 1 ps (green solid line) and 5 ps (blue solid line). In the *upper panel*, the evolution of the transient spectra is displayed after 5 ps: 5 ps (black dashed line), at 20 ps (red dashed line), 100 ps (green dashed line) and 500 ps (blue dashed line). In the *inset*: transient absorption spectrum at 1.5 ns delay time, both B and SE contribute to the negative Q_x origin peak at around 620 nm. The arrows indicate the time changes of the signals.

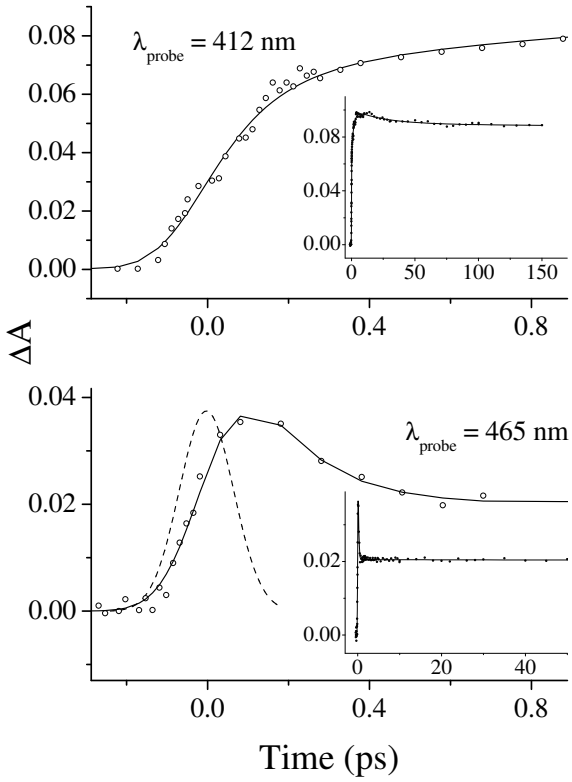

Figure 3.6: Kinetics profiles (open circles) recorded at 412 nm (upper) and 465 nm (bottom) for the PH_2 in benzene/cyclohexane solution (c = 3×10^{-5} M), pumped at 400 nm. The cross-correlation Gaussian profile (fwhm = 160 fs) between pump and probe is also reported as dashed line. The insets of the two panel show the behavior for long delay times.

and, at 200 fs delay time, two ESA bands are observed with maxima at 412 and 465 nm.

The two bands show largely different kinetic behaviors, as reported in separate panels of Figure 3.6.

The longest wavelength component rises within the time resolution of our apparatus and decays in less than 600 fs to a nonvanishing background level. By applying the deconvolution/fitting procedure, it is not possible to resolve the ultrafast formation of the state responsible for this signal, whereas the decay time of the band is confidently fitted to 150 ± 40 fs. Simultaneously the intensity of the signal centered at 412 nm increases and the relative maximum experiences a blue-shift. This phenomenon is apparent in

Fig.3.5-upper panel. It is proper to note that this ESA band is severely distorted due to the onset of the Soret absorption: above 400 nm the band is partially cancelled by Soret bleaching. From the analysis of the kinetics profile recorded at 412 nm, four different components to the signal are identified. The biexponential growth with time constants 140 ± 40 fs and 1.8 ± 0.3 ps is followed by two decay processes at different timescales: the first one has a lifetime of 25 ± 3 ps, the second one is too long to be measured accurately with our apparatus, but is consistent with the lifetime of the Q_x state (10.7 ns in a nondegassed benzene solution [105]).

Finally, exciting into the Q_y vibronic band at 490 nm, transient spectra in the range 410-480 nm have been obtained. Due to the low absorbance of the Q_y band and to the difficulty of spatially separating the pump from the probe beam, the obtained transient spectra (data not shown) have a spectral quality lower than those of recorded with excitation pulses at 400 nm. Nevertheless, the spectra obtained at early delay times indicate conclusively that the two ESA bands at 412 and 465 nm are due to initial states different from B.

Diprotonated porphyrin. The transient absorption spectra of **2** in the same experimental condition as for **1** are collected in Figure 3.7. At zero delay between pump and probe the dication porphyrin shows an unstructured broad ESA band that undergoes spectral evolution at positive delay times. Already at 200 fs, the spectrum exhibits a transient absorption centered at 440 nm with a long tail extending up to 525 nm. The intensity of the maximum increases in the interval up to a few tens of picoseconds. The Q band bleaching is also observed.

In order to fully characterize the spectral dynamics, we measured the kinetics profiles at 440 nm and at 500 nm. Representative results along with multi-exponential fits are reported in Fig.3.8. Three separate dynamic components are observed: the formation of the transient in few hundreds of femtoseconds, a second process in the picosecond range and a decay of several nanoseconds. The corresponding time constants obtained from the deconvolution/fitting procedure are $\tau_1 = 300 \pm 50$ fs, $\tau_2 = 9 \pm 2$ ps and $\tau_3 = 5.5$ ns. The latter value was kept constant in the fitting process and equal to the Q

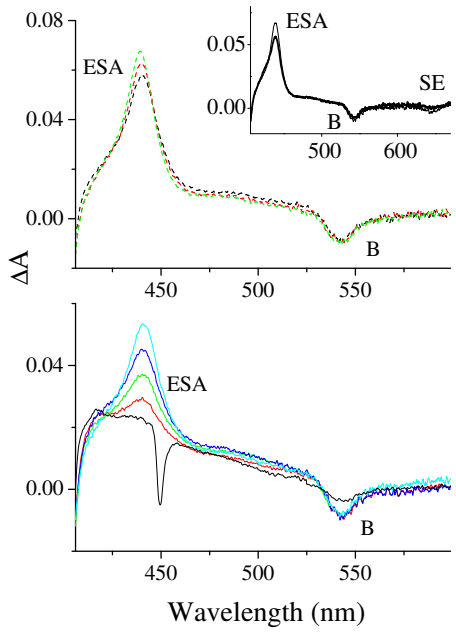

Figure 3.7: Transient absorption spectra of **2** (c = 2×10^{-5} M in benzene/cyclohexane 1:10, 5% trifluoracetic acid), exciting at 400 nm, at selected delay times. The ESA, SRG, B and SE symbols identify transient bands due to excited-state absorption, stimulated Raman gain of the solvent, bleaching and simulated emission, respectively. In the *lower panel*, the transient spectra in the first picosecond are shown: temporal coincidence between pump and probe pulses (black solid line), at 200 fs (red solid line), at 400 fs (green solid line), at 600 fs (blue solid line) and at 1 ps (cyan solid line). In the *upper panel*, the evolution of the transient spectra is displayed at 2 ps (black dashed line), at 10 ps (red dashed line) and at 20 ps (green dashed line). In the *inset*: transient absorption spectra at 20 ps (thin line) and at 1.5 ns (thick line) delay times.

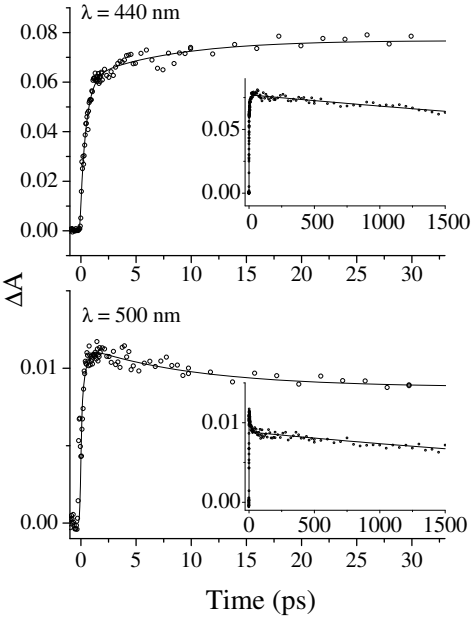

Figure 3.8: Kinetics profiles (open circles) recorded at 440 nm (upper) and 500 nm (bottom) of **2** in the same experimental conditions detailed in Fig.3.7. The insets of the two panel show the transient absorbances at the probe wavelengths for long delay times.

lifetime measured in the non-degassed solution (see Table 3.1). As we can see in Fig.3.8, the shortest time τ_1 corresponds in both kinetics profiles to a rise time, while the second time τ_2 has positive amplitude (decrease of intensity) for the kinetics measured at 500 nm and negative amplitude when the probe is at 440 nm, indicating that this time constant corresponds to the decay time at 500 nm and to the rise time at 440 nm of the same relaxation process.

Tetraoxaporphyrin dication. The transient absorption spectra of **3** in $HClO_4$ (see Figure 3.9), pumped at 370 nm ($S_0 \rightarrow S_2$ transition) exhibit a remarkably well structured ESA band doublet at 405 nm and 412 nm for delay time $\geq$20 ps. The intensities of the two components simultaneously increase and reach the maximum at about 100 ps. Beyond this delay time the intensity of the transient spectra decreases and, as shown in the inset, the profile remains unaltered. In Figure 3.10 the kinetic profiles recorded in correspondence of the two maxima are reported. The time profiles are well reproduced by the convolution of the instrumental function with a single rise time of 25 ± 5 ps and a single decay time of 7.2 ns. The latter value is coincident with the fluorescence lifetime of the Q state (see Table 3.1) and is kept constant during the fitting procedure. In the observed kinetic profiles, a spike is also present, appearing and decaying within our temporal resolution. The spike is ascribed to a two-photon process [82, 106] and does not add any information about the excited states of the molecule.

3.5 Discussion

Considering first porphine **1**, irrespective of the excitation transitions at 400 nm ($S_0 \rightarrow B$) or at 490 nm ($S_0 \rightarrow Q_y$) , we observe two ESA bands at 412 nm and 465 nm even at very short delay times. No rise component is resolved for the 465 nm ESA signal when exciting in the Soret band, suggesting that the decay from the directly excited state is within the time resolution of our apparatus, 160 fs. This interpretation is in accordance with the results reported in previous studies [107, 108]. In fact, in porphyrin derivatives an upper limit of $\approx$ 40 - 50 fs has been estimated for the $B \rightsquigarrow Q_y$ internal conversion.

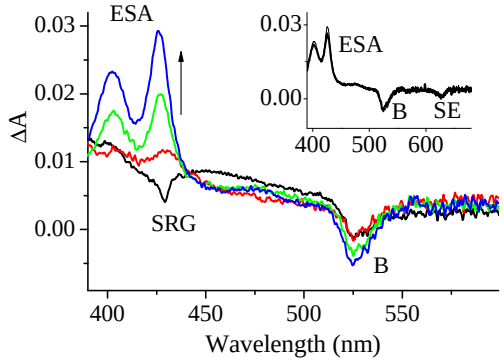

Figure 3.9: Transient absorption spectra of **3** (c = 6×10^{-6} M in $HClO_4$), exciting at 370 nm, at selected delay times. The ESA, SRG, B and SE symbols identify transient bands due to excited-state absorption, stimulated Raman gain of the solvent, bleaching and simulated emission, respectively. Key: black solid line, temporal coincidence between pump and probe pulses; red, green and blue solid line, 5, 20 and 200 ps delay times, respectively. In the *inset*: transient absorption spectra at 200 ps (thin line) and at 1.5 ns (thick line) delay times.

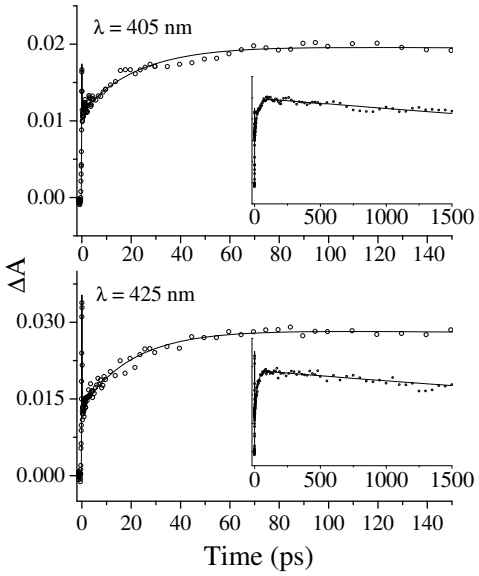

Figure 3.10: Kinetics profiles (open circles) recorded at 440 nm (upper) and 500 nm (bottom) of **2** in the same experimental conditions detailed in Fig.3.7. The insets of the two panel show the transient absorbances at the probe wavelengths for long delay times.

Moreover, the decay time of the 465 nm transient coincides, within the experimental accuracy, with the shortest rise time of the 412 nm transient. This means that the Q_y depopulation is coupled with a population growth relative to the manifold of the Q_x vibrational levels quasi-degenerate with Q_y. Accordingly, the two kinetic behaviors correspond to the same deactivation channel, i.e., $Q_y \rightsquigarrow Q_x$ internal conversion with time constant of ≈150 fs. This time is much shorter in H_2TPP [108] and stretches to 90 fs in the more complex derivative having two phenyl substituents on opposite *meso* positions and methyl or ethyl groups in all β positions [107]. Thus, the internal conversion rate increases from **1** to H_2TPP, paralleling the increasing number of phenyl substituents along the ring periphery. Also the subsequent decay processes are slower in **1** than in the derivatives. The decay time constants of 1.4 and 1.5 ps for the two substituted porphyrins are attributed to vibrational energy relaxation in the Q_x state [107, 108]. In the case of **1** the time constant is slightly longer, 1.8 ps. The substituent effect is even larger for the last process occurring in Q_x before fluorescence, i.e., thermal equilibration with the solvent. The time constant of 25 ps for **1** exceeds appreciably the reported value for H_2TPP, which is in the range 10 - 20 ps [108]. The time constants are resumed in Table 3.2.

Going from **1** to **3** the molecular symmetry increases from D_{2h} to D_{4h} so that, as already pointed out in the section 3.3, the Q and B states are doubly degenerate and their energy separation is much larger than between B and Q_y. A single rise process of 25 ps time constant is observed before fluorescence, indicating that the population of the thermally equilibrated Q state increases in the picosecond timescale. As to the B lifetime, an upper limit of ≈ 100 ps can be estimated from the time-resolved fluorescence and a value of ≈ 40 ps is calculated from quantum yield measurements on highly diluted ($\approx 10^{-7}$ M) solutions. Considering the uncertainty of this indirect determination, we can reasonably conclude that the rise of the Q state population is correlated with the decay of the B state, i.e. the internal conversion process $B \rightsquigarrow Q$ takes place with a time constant of ≈ 25 ps. Vibrational relaxation, which is known to occur in few picoseconds or less in the excited states [109], is not resolved in respect to internal conversion. A good estimate

Table 3.2: Multiexponential fittings of the observed kinetic profiles shown in Figs.3.6, 3.8 and 3.10: time constants (τ, ps), amplitudes (A) and wavelengths (λ_{probe}, nm). Decay processes correspond to positive amplitudes while rise processes to negative amplitudes.

(1)			(2)			(3)		
λ_{probe}	A	τ	λ_{probe}	A	τ	λ_{probe}	A	τ
412	-0.06 -0.03 0.01 0.09	0.14 ± 0.04 1.8 ± 0.3 25 ± 3 $10.7^{(a)}$	440	-0.05 -0.016 0.08	0.30 ± 0.05 9 ± 1 $5.5^{(a)}$	405	-0.009 -0.02	25 ± 3 $7.2^{(a)}$
465	0.037 0.02	0.15 ± 0.04 $10.7^{(a)}$	500	-0.05 0.026 0.009	0.33 ± 0.05 9 ± 1 $5.5^{(a)}$	425	-0.015 0.029	25 ± 3 $7.2^{(a)}$

$^{(a)}$ time constants in nanoseconds held fixed in the multiexponential fitting.

of the thermal equilibration process in the Q state can be achieved from the observed blue-shift of the band, as a function of the delay time. Although the accuracy is limited by the scarcity of data points, the plot reported in Figure 3.11 is reasonably fitted to a single exponential with time constant of ≈ 11 ps. The thermal equilibration component may be deconvoluted from the total rise process without altering substantially the time constant of the internal conversion.

The dramatic increase of the IC time constant in comparison with ≈ 50 fs in **1** is related to larger energy gap $\Delta E(B - Q)$ [110]. In other words, no additional singlet state between B and Q contributes to the decay. In this respect, we note that the energy level diagram of **3** is similar to that of D_{4h} metalloporphyrins, the only difference being the reduced gap in the latter systems. This leads to speculate about a possible correlation between the internal conversion rate constants of **3** and of metalloporphyrins. B fluorescence lifetimes have been reported [111, 112] for Zn(II) and Mg(II) TPP in various solvents for which $\Delta E(B - Q)$ ranges between 6300 and 7100 cm^{-1}. The rate constants, calculated at moderate/small fluorescence quantum yields [111], are plotted in

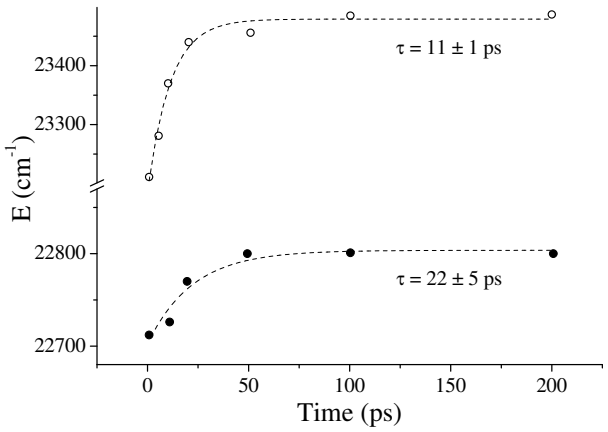

Figure 3.11: Dynamic blue shift of the ESA band at 440 nm, for **2** (full circles)and at 425 nm, for **3** (hollow circles). The time constant of the thermal equilibration in the Q state are indicated in the figure.

Figure 3.12 in a semilogaritmic scale *vs* $\Delta E(B-Q)$; the corresponding value for **3** is also reported. As the latter value falls close to the semilogaritmic linear plot, it is tempting to propose that the 25 ps lifetime fairly corresponds to that of the D_{4h} porphyrin macrocycle isoelectronic with **3** in the absence of the central metal atom. Diprotonated porphyrin **2** is a more complex case than **1** and **3**. In fact, the rate of the internal conversion depends on the separation energy between the two states [110]; for **2** the value of 8500 cm^{-1} is comparable, though smaller, to that of **3** and much larger than that of **1**. Then, we are inclined to associate the observed time constant of 9 ps with the $B \rightsquigarrow Q$ decay. On the other hand, the B lifetime is estimated $\approx$ 150 fs from fluorescence yield and radiative lifetime measurements. To our opinion, the difference between 150 fs and 9 ps is too large to be attributed to inaccuracies of the indirect estimate, as proposed for **3**. This leads us to conclude that decay processes more efficient than the $B \rightsquigarrow Q$ internal conversion are operative in the present case. As a matter of fact, it should be recalled that nonplanar porphyrins have strongly reduced Q lifetimes in respect to those of substituted planar porphyrins [92, 93]. The effect is attributed to the torsional flexibility of **2** in the Q state. The conformational freedom produces excited state configurations with vertical energy gap from the the ground state smaller than that of the equilibrium Q geometry, thus

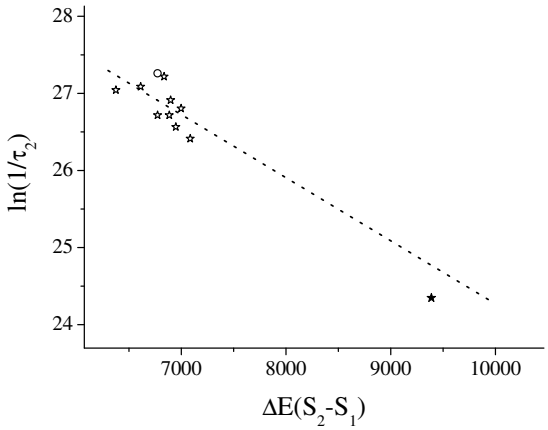

Figure 3.12: Logarithmic plot of the IC $B \rightsquigarrow Q$ rate constant $1/\tau_2$ (s^{-1}) *vs* energy gap (cm^{-1}) between the two states. Stars and hollow circle refer to data taken from literature [111, 112] for Zn(II) and Mg(II)-TTP in various solvents. The full star is the value of the rate constant for **3** determined in this work. The dotted line has been obtained from the linear regression of data on metalloporphyrins.

enhancing the rate of internal conversion [94]. A similar mechanism may be invoked for the B state.

As a second point, a charge transfer state is possibly involved in the deactivation process of the B state, according to a recent suggestion [113]. In Figure 3.3 the B fluorescence is shown for the three studied molecules and the emission profile of **2** is extended over a range wider than for **1**. A band roughly centered around 486 nm can be singled out and two assignments can be hypothesized, i.e. fluorescence either from the second conformer of **2**, S_2 (**2**;C_i) $\rightarrow$ S_0 (**2**;C_i), or from the lowest CT state of the complex (**2**;D_{2d})$(CF_3COO^-)_2$. The first hypothesis is ruled out on the basis of MO calculations[1], from which the first vertical transitions are obtained. The calculated energy values do not vary appreciably with the conformational structure. Thus, we extended the calculation to a molecular complex, in order to evaluate the second hypothesis [105]. The system under consideration is the simplified complex, obtained by substitution of the trifluoroacetate

[1] All the TD-DFT calculations, discussed in this chapter, have been performed by Dr Moroni Laura, Dr Gellini Cristina and Prof. Salvi Pier Remigio, Dipartimento di Chimica, Università degli Studi di Firenze.

with the formiate counterion in order to preserve the D_{2d} symmetry (**2**;D_{2d})$(HCOO^-)_2$. The counterion is in close contact with the macrocycle (O$\cdots$H distances as short as 1.502 Å) and two types of excited states are found. The first includes states arising from singly excited configurations built on MOs mostly localized on the macrocycle ring. These are $\pi\pi^*$ states approximately similar to the S_1 and S_2 states of the isolated H_4P^{2+}, with lower vertical excited energies as consequence of the presence of the counterion. The calculated transitions from the ground state to these states are at $\approx$ 547 nm and $\approx$ 362 nm, in good agreement with the experimental absorption spectrum of **2**. The second set of states are described as due to electron promotion from occupied MOs localized on the formiate counterion to virtual MOs localized on the porphyrin macrocycle. These are CT states and they are interspersed between S_1 and S_2 or at energy higher than S_2. The vertical excitation energy of the lowest CT states are estimated to be $\approx$ 478 nm and $\approx$ 473 nm, with oscillator strengths $\approx$ 0.01, they are also active in fluorescence. Moreover, the occurrence of CT state between S_1 and S_2 justifies the decrease to the picosecond/subpicosecond time regime of the S_2 lifetime in **2** compared to **3**. In fact, the internal conversions B $\rightsquigarrow$ CT followed by CT $\rightsquigarrow$ Q provide a more effective deactivation mechanism than the direct B $\rightsquigarrow$ Q channel. Following these considerations, we attribute the ultrafast 300 fs decay to a combination of two factors: B $\rightsquigarrow$ CT conversion and, probably to a lesser extent, B $\rightsquigarrow$ Q conversion through distorted B configurations. The second CT $\rightsquigarrow$ Q conversion occurs with time constant 9 ps. We know from the blue shift of the ESA band that the thermally equilibrated Q state is reached within $\approx$ 22 ps (see figure 3.11). In complete analogy to the case of **3**, the time constant of the CT $\rightsquigarrow$ Q internal conversion is practically unaffected by the inclusion of the thermal equilibration in the fitting procedure of the kinetic profile at 440 nm (Fig.3.8).

Summarizing, due to the presence of intruder CT states, the decay mechanism of **2** is intrinsically different from that of **3**. In fact, the rate constant corresponding to the 300 fs lifetime is at strong variance with those reported in Figure 3.12. For example, the B lifetime of ZnTTP measured by fluorescence up-conversion techniques, is 1.45 and 2.35 ps in benzene and ethanol, respectively [114, 115], in contrast with the ultrafast

lifetimes of porphyrin complexes with transition metals having partially filled d orbitals, which fall in the range 50-100 fs [116]. Thus, the metal ions influence considerably the photophysical process of the porphyrin core, allowing for charge transfer processes from the metal d orbitals to the macrocycle and vice versa.

Chapter 4

The truncated hemoglobin from *Thermobifida fusca*

4.1 A novel thermostable hemoglobin

The identification of "hemoglobin-like" proteins in thermophilic actinobacterium *Thermobifida fusca* was reported in 2005 by Boffi and coworkers [23]. The presence of hemoglobins in thermophilic micro-organism brings out fundamental questions concerning the structural parameters that lead to thermostability of these proteins. Four genes within the genome of the bacterium *Thermobifida fusca* have been identified for as many proteins: a protoglobin (Tf-Pgb), a truncated hemoglobin (Tf-trHb), a flavohemoglobin (Tf-FHb) and an additional globin-like protein. The biochemical functionality and the physiological significance of these most intriguing hemoproteins are still unknown.

The Tf-trHb is capable of efficient O_2 binding and releasing between 55 and 60 °C, the optimal growth temperature for *Thermobifida fusca*. On the contrary, vertebrate myoglobins are inefficient in exchanging exogenous ligands at high temperature. The crystal structure of the ferric, acetate-bound derivative was obtained at 2.48 Å resolution [23] and it conforms to that of group II truncated hemoglobins. Its three-dimensional structure is reported in Figure 4.1 (PBD code: 2BMM): it consists of a two-over-two

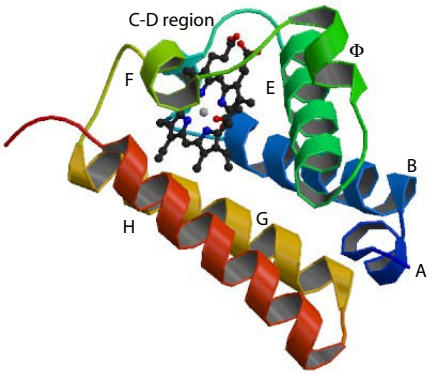

Figure 4.1: Three-dimensional structure of Tf-trHb. It displays a two-over-two alpha helical sandwich fold formed by the helices B, E, G and H; shorter F and A helices than in the classic globin fold; absence of helices C and D; presence of an additional phi-helix between helices E and F.

alpha helical structure.

The distal heme pocket architecture (see Figure 4.2) shows that the acetate ion ligand is stabilized by interactions with residues Tyr67-CD1 and Trp119-G8. The carbonyl oxygen of the acetate ion is hydrogen bonded to the OH group of the former amino acid and to the indole group of tryptophan (distances = 2.86 and 2.52 Å, respectively). The latter amino acid is rigorously conserved in the three proteins showed in Figure 4.2, i.e., Tf-trHB and other two group II hemoglobins from *Mycobacterium tuberculosis* (Mt-trHbO) and from *Bacillus subtilis* (Bs-trHb). The Trp119-G8 is essentially parallel to the heme plane. In the proximal region the His106-F8 is bonded to the Fe(III) of the heme with an unusually short distance (N-Fe = 1.92 Å). As we discussed in Chapter 1, the ligand photodissociation by short laser pulses in hemoproteins-ligand adducts is widely employed to unravel the elementary dynamical processes underlining the structure-function relationship of these proteins. The native residues chain has been modified to study the effects of the specific amino acids inside the heme pocket. We performed transient absorption spectroscopy experiments on the mutant, hereafter referred to as TrpG8Phe, which presents three modified residues: F107E, R91E and W119F. The first two substitutions do not involve the heme pocket, but they have proved necessary to obtain the mutation into the pocket, furthering the solubility and the subsequent handling of the samples. Since

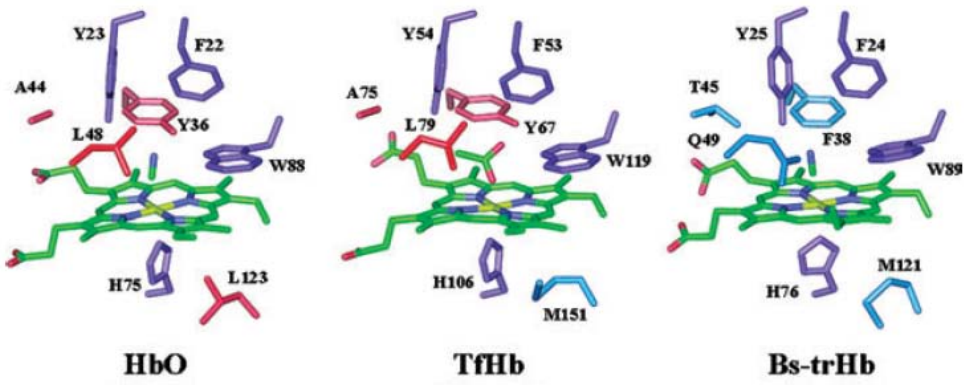

Figure 4.2: Close up view of the active sites of Tf-trHb (in the center, PDB code: 2BMM), Mt-trHbO (on left, PDB code: 1NGK) and Bs-trHb (on right, PDB code: 1UX8). Residues that are conserved in all three structures are marked in violet, Tf-trHb residues conserved with respect to Mt-trHbO and Bs-trHb are red and cyan, respectively (from Bonamore *et al* [23]).

these mutations concern only lateral amino acids, we expect that in the double mutant the photophysical heme properties and the geminate recombination rate are unchanged in respect to the native protein. Indeed, the strict similarity of the experimental data for the two systems supports this hypothesis and the same conclusion can be reached for the wild-type Tf-trHb and its double mutant (F107E and R91E). Therefore, the latter can be considered as the *scaffold* protein in respect to the mutant TrpG8Phe. We present here the results on the CO complexes of the *scaffold* protein and the TrpG8Phe mutant investigated by femtosecond time resolved transient absorption spectroscopy. The important mutation on TrpG8Phe is the replacement of the tryptophan with phenylalanine.

4.2 Experimental and data handling

The gene coding for a hemoglobin-like protein (Tf-trHb) was cloned in *Escherichia coli* for overexpression. The truncated hemoglobin from *Thermobifida fusca* (Tf-trHb) samples were provided in the ferric form by Prof. Boffi (Department of Biochemical Sciences, University of Rome "La Sapienza", Italy).

The ferrous Hb form (*deoxy*) was prepared by adding a small amount of sodium

dithionite in a 0.1 M phosphate buffer at pH 7.2 under pure nitrogen atmosphere. It should be mentioned that excess sodium dithionite has a pronounced effect on the UV-vis absorption line-shape of the *deoxy* derivatives. An intermediate species with a blue-shifted Soret peak is detected, especially at high dithionite concentrations ($>$ 20 mM). This spurious species was observed in other truncated proteins [76] and assigned to the formation of a stable low spin ferric sulphide adduct [117]. Thus, in all our measurements, the dithionite concentration was constantly kept below 20 mM and different experiments were carried out on freshly prepared samples.

The CO complex was obtained by performing the same reduction under CO atmosphere, no change of the stationary spectrum is observed if the CO gas is added before or immediately after dithionite addition.

The concentration of all samples during the TA experiments was adjusted so as to yield an optical density OD $<$1.5 at the Soret maximum (optical path length = 2 mm), corresponding to a good signal to noise ratio in the whole probed spectral region. The samples were excited with the second harmonic (400 nm) of the fundamental pulses in resonance with the blue side of the Soret band. A white light continuum probe pulse measured the transient spectrum. The energy of the pump pulses was varied in the range 0.3-0.8 μJ to exclude possible intensity related artifacts.

4.3 Results

Figure 4.3 shows the steady-state spectra of ferrous Tf-trHb and its CO adduct, together with their difference spectrum. As for all hemoglobins, the spectra vary considerably depending on the oxidation state of the iron and on the molecule to which it is bound. The spectrum of the *deoxy* form shows two absorption bands at 429 and 557 nm. When the protein binds CO the first band (the Soret) becomes narrower and blue-shifts to 420 nm, while in the visible range two bands become resolved (542 and 570 nm). It is of interest to note that the spectral profile presents a shoulder at 620 nm.

In the time resolved spectra reported in the following subsections the characteristic

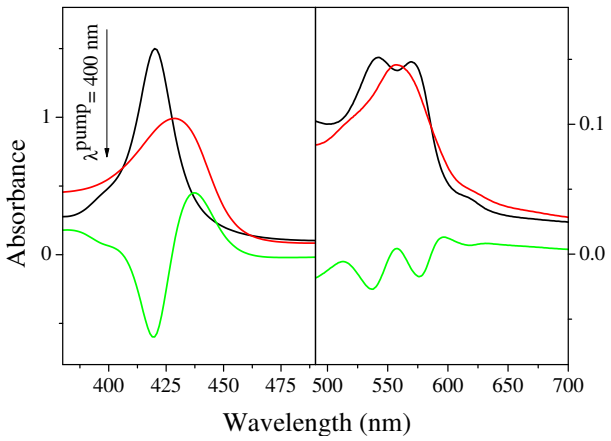

Figure 4.3: Steady-state absorption spectra of the ferrous Tf-trHb (red line) and its CO complex (black line). The difference spectrum is also shown (green line). The protein concentration is ≈ 50 μM (2 mm path length cell).

behavior of hemoproteins is revealed. They contain negative (B, bleaching) and positive (ESA, excited state absorption and AB, antibleaching) bands.

4.3.1 Tf-trHb CO complex

The transient absorption spectra of the CO complex of Tf-trHb at different delays after laser photolysis are presented in Figure 4.4, where four spectral features are evident:

- the bleaching of the Soret band at 420 nm;
- an ESA between 430 and 520 nm;
- the bleaching of the Q bands;
- a second diffuse ESA from 580 nm to the red side of the probed spectral range.

On the shortest timescale, the ESA band extending beyond 440 nm undergoes spectral narrowing and blue shifting, while the transient spectra evolve until the signal is dominated by the difference between the ground state spectrum of the Tf-trHb *deoxy* form and the CO adduct.

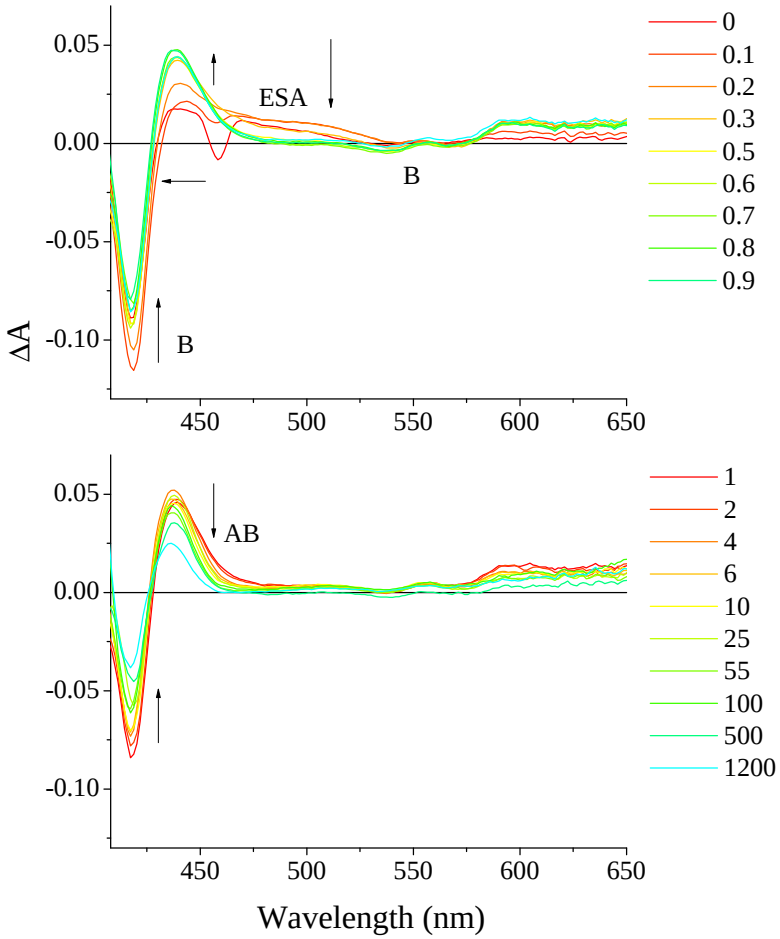

Figure 4.4: Transient absorption spectra of the **CO complex** of the **Tf-trHb** excited at 400 nm with femtosecond pulses (0.6 μJ/pulse). The absorbance of the sample is 0.4 at the pump wavelength. The delay times between pump and probe pulses are reported in the legends and the values are expressed in picoseconds. (Upper panel) transient spectra in the first 1 ps. The negative peak at 465 nm is due to the stimulated Raman gain of the water. (Lower panel) transient spectra after 1 ps delay time.

Indeed, it is well known (see Chapter 1) that laser pulses induce the dissociation of the bond between iron and CO, resulting in only one type of photoproduct: the dissociated pentacoordinate heme. As the resulting transient signal peaked at 437 nm is originated from the ground state of the last species and not from an excited state, it is common to refer as the antibleaching band [59].

In Figure 4.5 the decays of the signals extracted at significant wavelengths are reported. The fitting required the convolution of the Gaussin shape instrumental function (FWHM = 160 fs) with a multiexponential decay step function. The results are summarized in Table 4.1.

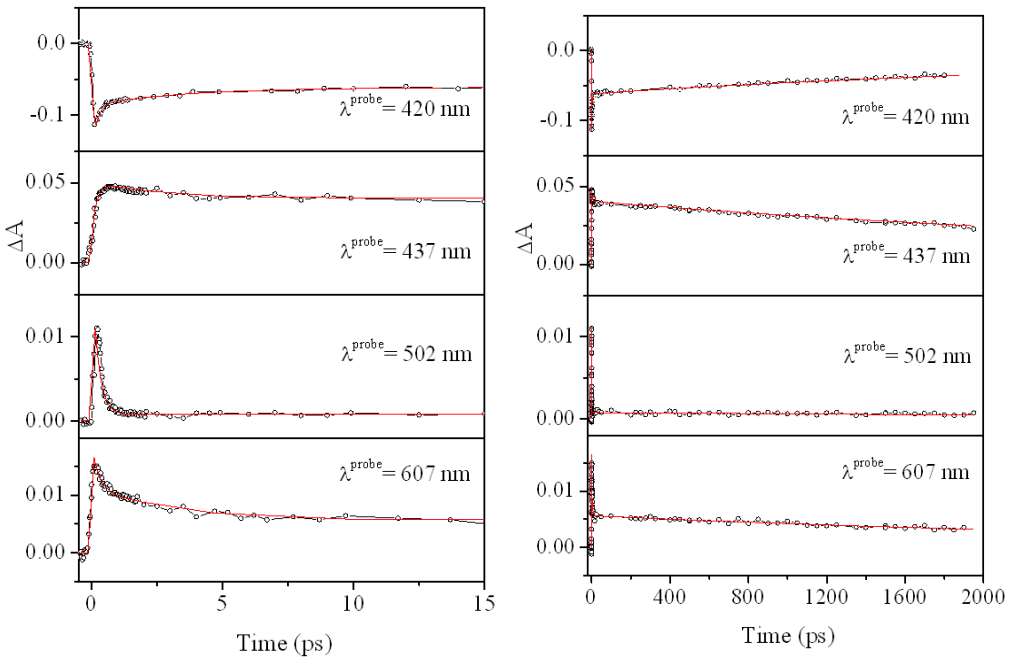

Figure 4.5: Transient absorbance of the **CO complex** of the **Tf-trHb** as a function of the delay time in the same experimental conditions detailed in Fig.4.4. The left panel contains the kinetic profiles in the first 15 picoseconds, the right panel shows the whole decay accessible with the experimental set-up.

Three different time constants result: 200-300 fs, corresponding to a decay process involving all the wavelengths except the AB component centered at 437 nm, a time constant of several picoseconds and a 3-4 ns component. In order to properly separate the transient signal associated with ligand dynamics and protein rearrangements from

Table 4.1: Multiexponential fittings of the observed kinetic profiles shown in Fig.4.5 recorded in the **CO complex** of the **Tf-trHb** sample: probe wavelength (λ_{probe}), time constants (τ, ps) and amplitudes (A). The analysis of the time dependent signal was done by fitting the convolution of the instrumental function with: $H(t) = \sum_i A_i(\exp(-t/\tau_i)$. Decay processes correspond to positive amplitudes while rise processes are associated with negative amplitudes. The opposite is true for the bleaching signal at 420 nm.

λ_{probe}	A_1	τ_1 (ps)	A_2	τ_2 (ps)	A_3	τ_3 (ps)
420	-0.18 ± 0.02 (45%)	0.34 ± 0.05	-0.08 ± 0.01 (20%)	4 ± 1	-0.14 ± 0.01 (35%)	3400 ± 200
437	-0.08 ± 0.03 (38%)	0.2 ± 0.1	0.03 ± 0.001 (14%)	3 ± 1	-0.10 ± 0.01 (48%)	3900 ± 400
502	0.05 ± 0.005 (96%)	0.2 ± 0.1	–	–	0.002 ± 0.001 (4%)	4000 ± 1000
607	0.02 ± 0.01 (50%)	0.2 ± 0.1	0.01 ± 0.01 (25%)	3 ± 1	0.010 ± 0.005 (25%)	3500 ± 200

those related to photophysical processes occurring after the excitation of the heme, it is convenient to study in detail the relaxation dynamics in *deoxy* Tf-TrHb.

4.3.2 *Deoxy* Tf-trHb

The transient spectra recorded at early times are reported in Figure 4.6. Four bands can be recognized in the 410-700 nm interval, peaked at about 425, 470, 560 and 610 nm. The

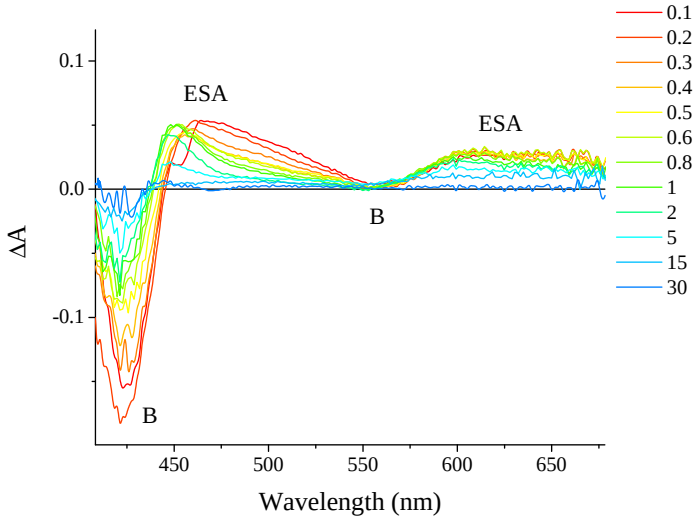

Figure 4.6: Transient absorption spectra of ***deoxy* Tf-trHb** excited at 400 nm with femtosecond pulses (0.8 μJ/pulse). The absorbance of the sample is 0.8 at the pump wavelength. The delay times between pump and probe pulses are reported in the legend, the values are expressed in picoseconds.

first band is associated to the bleaching of the Soret band and it forms instantaneously. In the 440 - 525 nm range, a positive absorption band is observed which narrows and shifts to lower wavelengths as time increases. The bands at 560 and 610 nm correspond to the bleaching of the Q band and to an excited state absorption, respectively. The spectra are corrected for the white continuum dispersion, so their rise time overlaps perfectly with that of the Soret bleaching. In Figure 4.6, the evolution of the signals is reported up to 20 ps. At later times, a residue of the signals is still visible with a very low intensity (ΔA $\approx$ 0.002-0.004) comparable to the fluctuations of the baseline. Even at the maximum delay time accessible with our experimental set-up (1.9 ns), the signal does not vanish

and its spectral profile is strongly reproducible. We observed a similar behavior in the horse heart myoglobin; a small offset at long delay has been noticed also in the band-III region transient spectra, after Q-band excitation of skeletal muscle myoglobin [48]. The observation that this contribution is not linearly proportional to the intensity of the pump pulse, suggests that it arises from a two-photon absorption [82]. On the other hand, we cannot completely rule out effects due to the sulphide adduct on the dynamic behavior of this species. The difference in absorbance is too low for allowing a precise characterization of this signal.

It is convenient to follow the absorbance change at a given wavelength as a function of time (see Fig.4.7).

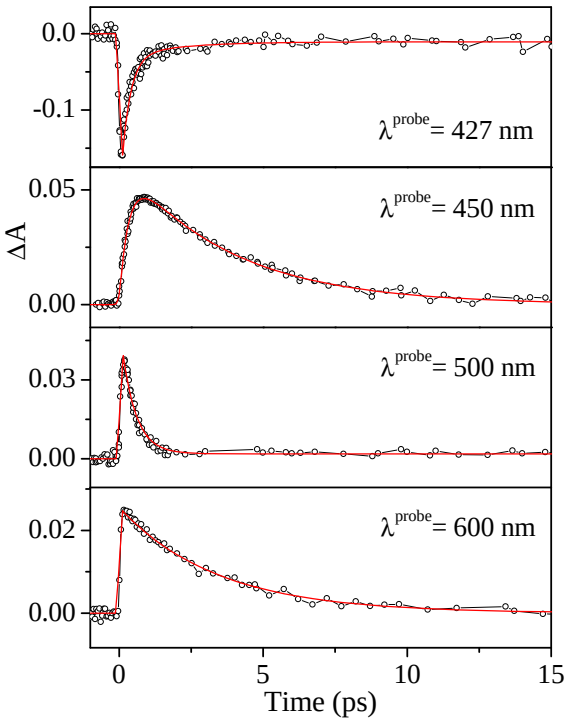

Figure 4.7: Transient absorbance of ***deoxy* Tf-trHb** as a function of the delay time in the same experimental conditions detailed in Fig.4.6.

Table 4.2 collects the optimized parameters obtained by fitting the time profiles of Fig.4.7 with a step function, convoluted with the instrumental function (pump-probe cross-correlation = 160 fs).

Table 4.2: Multiexponential fittings of the observed kinetic profiles shown in Fig.4.7 recorded in ***deoxy* Tf-trHb** sample: probe wavelength (λ_{probe}), time constants (τ, ps) and amplitudes (A). The analysis of the time dependent signal was done by the fitting of the convolution of the instrumental function with: $H(t) = \sum_i A_i(\exp(-t/\tau_i) + A_k$. Decay processes correspond to positive amplitudes while rise processes are associated with negative amplitudes. The opposite is true for the bleaching signal at 427 nm.

λ_{probe}	A_1	τ_1 (ps)	A_2	τ_2 (ps)	A_k
427	-0.15 ± 0.01 (84%)	0.36 ± 0.04	-0.02 ± 0.01 (11%)	2.5 ± 1.5	-0.009 ± 0.001 (4%)
450	-0.076 ± 0.002 (53.5%)	0.33 ± 0.05	0.065 ± 0.001 (46%)	3.6 ± 0.9	0.0007 ± 0.0003 (0.5%)
500	0.049 ± 0.005 (96%)	0.35 ± 0.06	–	–	0.002 ± 0.001 (4%)
600	–	–	0.025 ± 0.004 (99.5%)	3.4 ± 0.4	0.0001 ± 0.0001 (0.5%)

Two different processes contribute to the time evolution of these signals in distinct temporal domains: a fast component, with a decay time of several hundred femtoseconds (τ_1) and the recovery of the ground state in the picosecond timescale (τ_2). In the fitting procedure, the non-vanishing long delay component was taken into account as an offset: its weight is small ($<5\%$) for all the kinetics profiles. The longest time τ_2 corresponds to a decay process present at all wavelengths. The shortest time τ_1 corresponds to a decay when the transient is probed at 427, 500 and 600 nm, while it is a rise time in the kinetic profile recorded at 450 nm. It should be pointed out that the fast decrease of the bleaching of the Soret band is probably not due to a ground state recovery, but can be ascribed to the increase of the near by ESA signal with the opposite sign. Otherwise, a fast decrease would also be noted in the region of the Q band bleaching.

The data were obtained on a sample whose concentration was adjusted to have a Soret peak absorption of $\sim$1 OD in a 2 mm path length cell. Due to the lower value of the extinction coefficient, this implies that the concentration of this sample is higher than that of the Tf-trHB-CO solution. Other measurements have been carried out at different concentration without observing any variation in the time constant for the ESA band, and the induced absorbance scales linearly with the concentration.

The reported spectra are similar for all the hemoproteins studied in this work and also strongly resemble those reported by Challa *et al* [118] for the five-coordinated, high-spin heme in a nominally isotropic solvent environment. Despite more than 20 years of active research in the field involving several groups, the understanding of the electronic and vibrational behavior of photoexcited hemes has not yet converged to a single model. Nevertheless, it is widely accepted that the observed spectra are dominated by the vibrational dynamics associated with an evolving ground-state species. In the first picosecond, an isosbestic point at 456 nm is detected (see Figure 4.6), suggesting that a very fast internal conversion (IC) occurs between two electronic states, in agreement with the consecutive model applied to simulate the experimental data in the paper cited above [118]. The authors have found that, after the excitation of the blue side of the Soret band, a very rapid $S_2 \rightsquigarrow S_1$ decay (sub-100 fs) occurs, followed by a somewhat slower

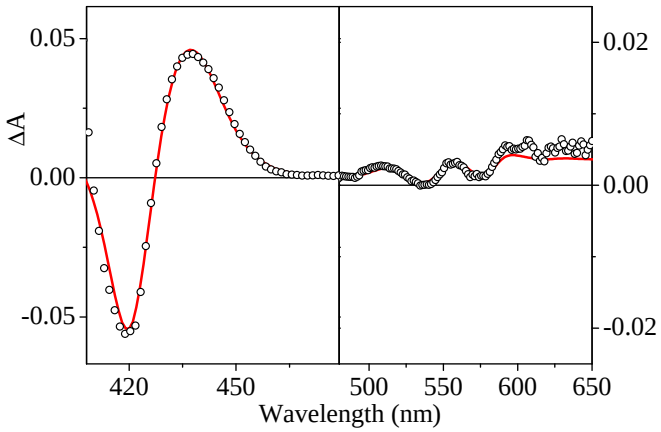

Figure 4.8: Comparison between the transient spectrum of the **CO complex** of the **Tf-trHb** recorded at 40 ps (open circles) and the static difference spectrum (red line).

(800 fs) $S_1 \rightsquigarrow S_0^*$ nonradiative decay. The S_0^* state evolves into the corresponding room-temperature, thermalized state S_0 via *intra*molecular vibrational energy redistribution (IVR) among the porphyrin modes and via *inter*molecular vibrational energy relaxation (VER) towards the protein/solvent. IVR is responsible of the energy transfer from the initial accepting modes associated with the $S_1 \rightsquigarrow S_0$ internal conversion to the rest of the macrocycle, while the energy in excess of the heme dissipates into the environment (protein and/or solvent).

Therefore, although the interpretation of ultrafast heme dynamics is not straightforward, we believe that the fast time constant is related to an excited state relaxation [45, 48, 118], while the second dynamic process can be ascribed to the vibrational relaxation of the hot electronic ground state. No protein conformational change and ligand effect are necessary to explain our observations in *deoxy* Tf-trHb. The complete cooling of the locally hot heme occurs with a rate constant of 3-4 ps.

Coming back to the CO adduct, the similarity between the first two time constants reported in Table 4.1 ($\tau_1 = 0.2 \pm 0.1$ ps and $\tau_2 = 3 \pm 1$) and those of the *deoxy* sample leads us to conclude that the relaxation of the electronically and/or vibrationally excited heme is completed within few tens of picoseconds, and that the geminate recombination process can be easily separated, taking place with a time constant $\tau_3 = 3-4$ ns ($k = 2.9 \pm 0.4 \times 10^8$

s^{-1}). In addition, it is worth noticing that the transient spectrum measured at 40 ps delay is identical to the properly scaled equilibrium difference spectrum (see Figure 4.8).

Thus, for longer delay times the transient absorption signal is simply composed of an amplitude decay with a fixed cross-zero point, matching the isosbestic point of the "stationary" absorbtion spectra of the two species. The isosbestic point corresponds to the wavelength at which the reactant and product have the same absorbance (i.e. $\Delta A = 0$ in the equilibrium difference spectrum).

4.3.3 Optical transients of mutant TrpG8Phe

In the mutant protein analyzed the tryptophan W119 (TrpG8) is substituted by a phenylalanine (see Figure 4.2). The ground state absorption spectra of the *deoxy* and the CO complex are reported in Figure 4.9.

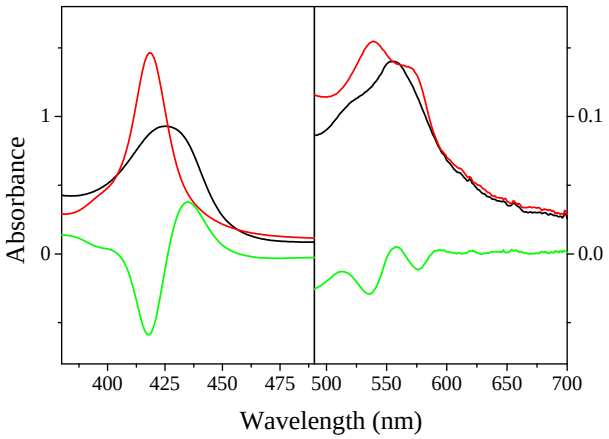

Figure 4.9: Steady-state absorption spectra of the ferrous TrpG8Phe mutant (black line) and its CO complex (red line). The difference spectrum is also shown (green line).

In the first few minutes after the addition of the reductant, the maximum of the Soret peak of the deoxygenated pentacoordinated species changes from 425 to 423 nm and, although on lower wavelengths, it undergoes the same shift experienced by the unmodified *scaffold* protein. A remarkable difference between the steady-state absorption spectra of the two proteins is found in the relative intensity of the Q bands in the CO adduct.

Table 4.3: Multiexponential fittings of the kinetic profiles recorded in **TrpG8Phe** sample: probe wavelength (λ_{probe}), time constants (τ, ps) and amplitudes (A). The analysis of the time dependent signal was done by fitting the convolution of the instrumental function with: $H(t) = \sum_i A_i(\exp(-t/\tau_i) + A_k$. Decay processes correspond to positive amplitudes while rise processes are associated with negative amplitudes. The opposite is true for the bleaching signal at 430 nm

λ_{probe}	A_1	τ_1 (ps)	A_2	τ_2 (ps)
430	-0.12 ± 0.01 (70%)	0.25 ± 0.05	-0.053 ± 0.005 (30%)	3.8 ± 0.5
454	-0.062 ± 0.005 (51%)	0.35 ± 0.05	0.059 ± 0.002 (49%)	4.9 ± 0.7
500	0.036 ± 0.005	0.38 ± 0.05	–	–
600	–	–	0.015 ± 0.001	4.2 ± 0.5

The optical transients of the *deoxy* species are similar to those of the *scaffold* protein discussed in the previous paragraph; the time constants of the corresponding photophysical processes are summarized in Table 4.3.

Differently from the previous case, no long delay offset absorption is observed. In agreement with the multi-photon origin hypothesis, the absence can be attributed to the lower energy of the pump pulse (0.6 instead of 0.8 μJ).

In Figure 4.10, the kinetic profile corresponding to the anti-bleaching maximum is compared to the profile recorded in the *scaffold* protein, together with the signal of the native protein. It can be seen that the optical transient of the TrpG8Phe is very similar to that of the native form, while a slightly faster decay can be revealed on the *scaffold* protein. Thus we are tempted to consider the effect of different heme environment on the vibrational relaxation. However, we retain that the discussion of such a little difference between the decay curves can be forced through, at the moment. Actually, some theoretical studies [54, 119] suggested that the strong electrostatic interactions between propionate side chain and solvating water is the most important "doorway" for dissipation

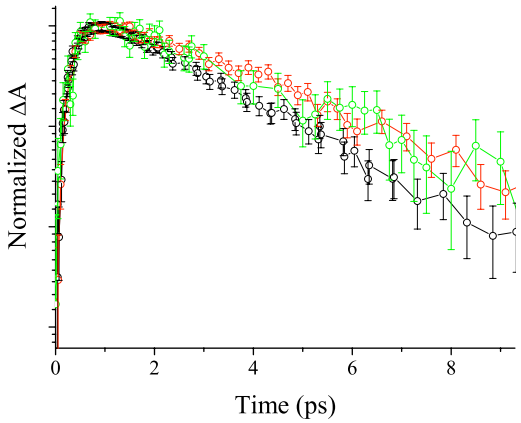

Figure 4.10: Kinetic profiles of the *scaffold* (black line) Tf-trHb, of the TrpG8Phe mutant (red line) and of the wild-type protein (green line) probed at their respective anti-bleaching maximum wavelengths.

of excess heme kinetic energy in myoglobin as it was experimentally confirmed [58] on samples with a strongly modified heme environment, i.e., the iron-porphine reconstituted myoglobin in which all of the side chains of heme are replaced by protons. In our samples the difference in the heme environments is not so pronounced, especially between the native and the *scaffold* protein, and for the sake of completeness we note that the kinetic profile of the anti-bleaching in the horse heart myoglobin does not significantly deviate from the wild-type Tf-trHb protein.

We conclude that excitation at 400 nm does not lead to significant differences between the *deoxy* form of the two proteins, the mutant and the *scaffold*. The overall similarity of the relaxation processes in the hemoproteins may be a sign that the influence of the heme environment upon the relaxation dynamics of the photoexcited heme is rather subtle.

On the other hand, the behavior of the CO adduct of the mutant is markedly dissimilar.

In Figure 4.11, the normalized kinetic profiles of the two proteins in correspondence of the respective antibleaching maximum are compared. The signal measured for the mutant is highly non-exponential: a reasonable fit can be obtained with a rise time $\tau_1 = 0.28 \pm 0.05$ ps and a decay described by multi-exponential function with $\tau_2 = 6 \pm 2$ ps (24%), $\tau_3 = 440 \pm 50$ ps (52%) and $\tau_4 = 3500$ ps (26%). The last contribution is kept

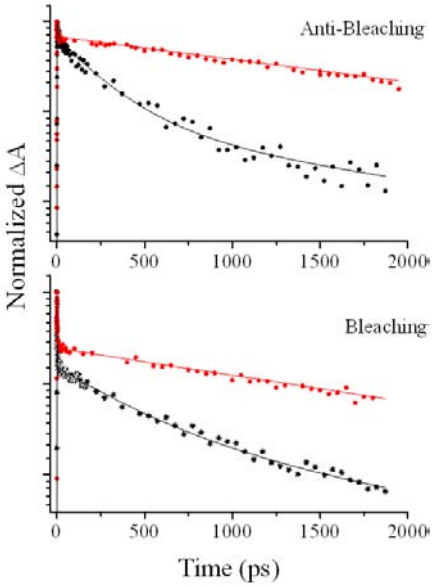

Figure 4.11: The kinetic profiles for TrpG8Phe (black solid circles) in correspondence of the bleaching and antibleaching maxima wavelengths are plotted in logarithmic scale. The continuum data are the fitting result. For comparison the data of the *scaffold* Tf-trHb are also shown in red (normalized to the maximum).

constant during the fitting procedure, on the basis of the outcome of the fitting of the *scaffold* protein data and of the slope similarity at long delay times for the two proteins. The same treatment done for the signal in correspondence of the bleaching gives the time constant $\tau_1 = 0.2 \pm 0.1$ (33%), $\tau_2 = 4 \pm 1$ ps (23%), $\tau_3 = 550 \pm 70$ ps (26%) and $\tau_4 =$ 3500 ps (18%). τ_1 and τ_2 are in very good agreement with their analogues reported in the Table 4.1 for the CO complex of the Tf-trHb. The decay of this species was in fact fitted by a three-exponential function, with time constants $\tau_1 = 0.34$ ps, $\tau_2 = 4$ ps and $\tau_3 = 3400$ ps. It appears evident that an additional process, with time constant of 550 ps contributes to the overall relaxation of the mutant protein.

4.4 The CO geminate recombination

The geminate recombination process provides a valuable tool for assessing the steric and electrostatic role of the heme pocket. In contrast to NO ligand, a sub-nanosecond

geminate recombination of CO and heme is rarely observed in hemeproteins[1].

Recently, a fast geminate recombination dynamics (τ=770 ps) in the CO complex of *Bacillus subtilis* truncated hemoglobin (Bs-trHb) has been reported by Feis *et al* [76]; their discussion supports the scenario in which the dynamics of the ligand is confined within the distal pocket with a little possibility for the CO to escape towards either the solvent or the adjacent small hydrophobic cavity comprised between the TyrB10 and PheCD1 residues. A bimolecular rebinding phase has been found with very small quantum yield $\approx 1\%$ in the microsecond time regime [22]. The fraction of heme recombining with the CO on the timescale of several nanoseconds or longer would result as an offset with constant amplitude in the transient absorption kinetics profiles. In contrast to Bs-trHb, Tf-trHb does not present any small cavity located at the top of the distal pocket. As reported in Table 4.1 and in Figure 4.11, in the case of Tf-trHb a single exponential decay with time constant of $3-4$ ns describes well the behavior of the kinetics after the first few tens of picosecond (see Fig.4.11, red lines). A nonzero asymptotic contribution is not required to simulate the decays as indicate that the energy barrier for the CO escape is very high and the yield of geminate recombination is consequently large. In the absence of experimental data for delay times longer than 2 ns, and not knowing the bimolecular dissociation yield[2], we can not completely rule out that a small fraction of heme does not recombine with CO. The same conclusion can be reached from the data recorded on the wild-type protein sample. At this point, it is interesting to note that the three-dimensional structure of the Tf-trHb shows a striking difference from those of other truncated hemoglobins that is, the absence of the internal cavities [23]. This evidence strongly suggests that the probability of the CO to escape from the heme pocket is negligible. On the other hand, the ligand stabilization inside the pocket is consistent with the "ligand-inclusive hydrogen bond network" of polar residues [75, 120], a common general pattern of the group II truncated hemoglobins. Besides, in Tf-trHb compared with

[1] A review of this topic can be found in Chapter 1.

[2] Note that in this context we refer to the bimolecular dissociation yield in the sense reported by Champion and coworkers and expressed by $Y_b = \eta Y_0$, where Y_0 is the photolysis efficiency (equal to 1 in the case of CO ligand) and η indicates the fraction of ligand that escapes to the solvent [59].

Bf-trHb an additional potential hydrogen bond donor is provided by a TyrCD1 residue; the mutation of CD1 tyrosine to phenylalanine has been considered as responsible for the 77-fold increase in the CO combination rate constant of the truncated hemoglobin from *Micobacterium tubercolosis* (trHbO) [75]. Fast geminate rebinding occurs either when the ligand can not diffuse away from the iron (rigid hydrogen bonding network) or when the iron-associated barrier is very low (no steric restraint) [75]. Therefore, the slower geminate recombination rate in Tf-trHb than in Bs-trHb can be attributed to a larger barrier for the recombination process, consistent with different interactions inside the heme distal region. The substitution of a polar amino acid (tyrosine) with an apolar one (phenylalanine) seems to facilitate the geminate recombination. This suggests that the presence of the tyrosine in position CD1 impairs binding of the ligands to the heme iron. The presence of the tyrosine instead of the phenylalanine modifies the configuration of the distal heme pocket so that steric hindrance can influence the ligand properties of the heme to a degree comparable to that of the electrostatic interactions [**?**].

As we have already seen, the mutant is characterized by a multiphasic heme-CO recombination kinetics on the picosecond timescale. The analysis of our data was performed following closely previous studies [73, 74, 121]. We can safely assume that the geminate recombination in the picosecond timescale is related to the rebinding of CO within the distal pocket, being this process favored by the orientation due to the presence of the heme iron at a short distance. The two phase relaxation can then be attributed to CO rebinding from different locations within the distal pocket region. However, due to the fact that the relaxation process of the protein takes place on the same timescale, some further considerations on the model are required. A detailed discussion about the functions used to fit the experimental data is reported for NO geminate recombination in myoglobin [68, 122]. In this case, the authors point out that the non-exponential behavior of the rebinding process can be attributed to two physically different phenomena. The distribution of rates can arise from a distribution of barriers associated with different protein molecules (substrates) or from the time-dependent evolution of the barrier for the rebinding process. The former case occurs when the transitions between the inhomo-

geneous population are slow in respect to the rebinding rate, while the latter possibility can be also seen as the non-equilibrium relaxation of the whole protein triggered by the ligand dissociation, i.e. the complex rebinding from a homogeneous population with multiple binding sites. The two processes are not mutually exclusive and can play a role of different relevance, depending on the conditions of the system, such as the temperature. The temporally distributed barrier to rebinding brought by Petrich *et al* [68] in their discussion can be adopted in our case to rationalize the applied bi-exponential fitting procedure. Therefore, the obtained multiexponential kinetics should be considered as a sketchy description of a more general non-exponential process.

A way to unravel this complex photodynamics in hemoproteins consists in applying the SVD analysis, extracting the spectra associated with each exponential time (DAS)[3]. The spectral features of the decay phases are quite distinct and are reported for the *scaffold* Tf-trHb and TrpG8Phe mutant in Figure 4.12.

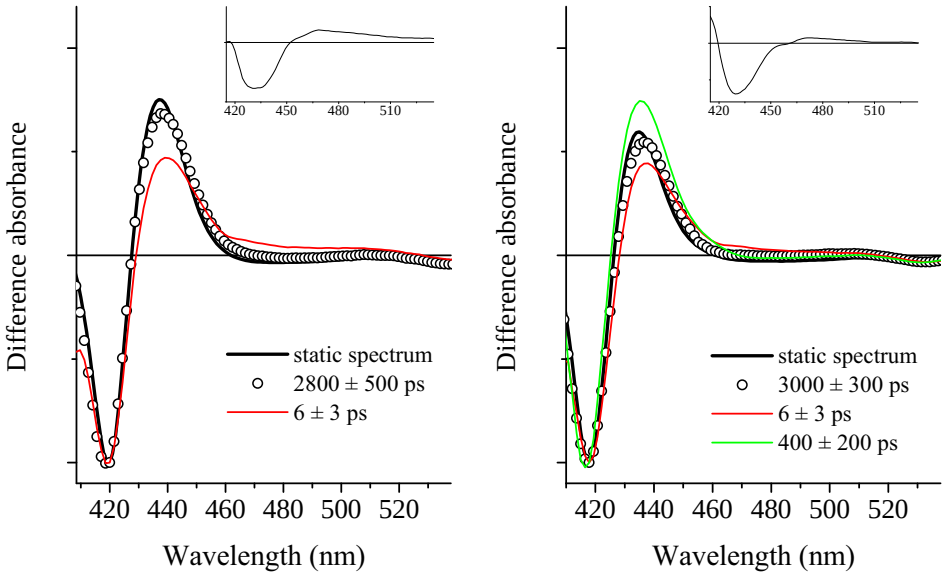

Figure 4.12: Results of SVD analysis of the *scaffold* Tf-trHb (left) and of the mutant TrpG8Phe (right). The black thick line represents the static difference spectrum, shown with the spectral component assigned to a particular relaxation times (DAS), normalized at the maximum of the Soret bleaching. In the insets: the short living decay associated spectra for the two proteins. The time constant is 0.3 ± 0.2 ps for both systems.

[3]See Chapter 2 for the description of the method adopted in the SVD analysis.

We observe that the obtained time constants are very similar to the values obtained from the single-wavelength kinetics fitting (see Table 4.1). Examination of the *scaffold* protein reveals that the component associated with the longest time (2800 ps) resembles the difference spectrum for thermally equilibrated ground state heme, as can be measured in static experiments. On the contrary, the fastest decay component (see the inset) shows a broad absorption that can be attributed to the transient CT state [45]. The intermediate component (6 ps) is red-shifted in respect to the difference spectrum so that the zero crossing is at 430 nm instead of 428 nm. Moreover, the antibleaching/bleaching intensity ratio does not match with the difference spectrum and the antibleaching appears broader. All this suggests that the heme is not thermalized and its cooling does take place on the timescale of a few picoseconds. This conclusion is in agreement with the observed coincidence of the experimental transient spectrum recorded at 40 ps with the static difference spectrum (Figure 4.8). The fact that the geminate recombination process can be described by a single exponential indicates that the global conformational change of the protein is faster than the CO geminate recombination. In contrast, the multiphasic CO rebinding kinetics in the mutant implies that the carbon monoxide, although partially restricted, can nevertheless adopt a range of different configurations from which rebinding to the heme can occur. As we noticed, a component with a time constant of $\approx 400-500$ ps must be added in order to describe the spectral evolution. The relative associated spectrum reported in Figure 4.12 (right) is blue-shifted. It was found that strong interactions with dissociated cloistered CO in the distal heme pocket can originate spectra shifted more to the blue, probably due to fact that the hemes are not completely domed [73]. This suggests that CO assumes a configuration favorable for the heme-bound state with the molecule aligned to the heme normal and the carbon atom pointing towards the iron.

Chapter 5

The flavohemoglobin from *Escherichia coli*

5.1 Structure and properties of HMP

The flavohemoglobin from *Escherichia coli* (HMP) has been identified in 1991 and it is the first discovered protein of the flavohemoglobin family [123]. Since its discovery, many studies have been undertaken with the scope of unveiling its physiological role and its structural properties. However, the detailed knowledge of its biological function remains undefined. A NO dioxygenase activity has been proposed [6] in which the NO could be aerobically converted to nitrate and more recently, it has been shown that HMP is able to catalyze the reduction of several alkylhydroperoxides into alcohols under specific conditions [124].

HMP is a 44 kDa protein whose absorption spectrum is indicative of a *b*-type hemoprotein. Because of the similarity between its amino acids sequence and that of the hemoglobin from *Vitreoscilla*, one of the first discovered bacterial hemoglobins, HMP is numbered among the "hemoglobin-like proteins". The overall fold of HMP consists on heart shaped structure in which three different domains are clearly distinguished (see Figure 5.1), namely the C-terminal NAD-binding domain, the FAD-bound domain and

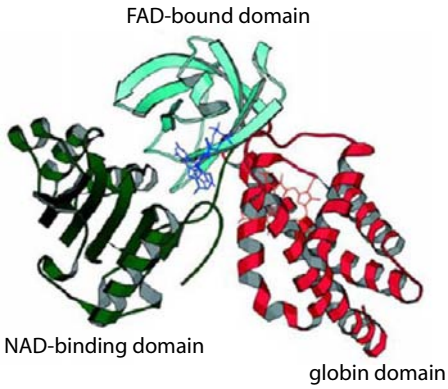

Figure 5.1: Overall structure of ferric unliganded flavohemoglobin from *Escherichia coli*; PDB code: 1GVH.

the N-terminal globin domain [19]. The architecture of the globin domain corresponds to a classical 3/3 globin fold composed of eight helices with an unusually long H helix and in which the D helix is substituted by a large loop region. From comparison of the amino acid sequence of this protein and of the vertebrate Hbs, it emerges that the topological distal positions E7 and B10, usually occupied by a histidine and a leucine, respectively, are replaced by a glutamine and a tyrosine. These amino acids determine the iron-bound ligand interactions; in particular, in the CO derivative the phenolic group of TyrB10 constitutes a hydrogen bond with the ligand [125], either direct or mediated by a water molecule. Studies in solutions [125, 126] evidenced two conformations of the distal heme pocket, the open and the closed one, the latter involves the interaction with CO and the TyrB10 side chain; this suggests that the protein presents a high conformational flexibility.

X-ray data revealed that the heme environment shows an unexpected distal pocket [19]. In fact the distal site of the ferric unliganded HMP is occupied by the isopropyl side chain of the LeuE11 with a 3.6 Å distance from the iron atom along the normal to the heme plane. This residue shields the heme iron from the residues in positions B10 and E7, the tyrosine and the glutamine, previously proposed as the iron-bound ligand stabilizers; they are shifted from the heme at a distance of more than 5 Å. In Figure 5.2 the structural details of the heme pocket are reported. The distal pocket architecture

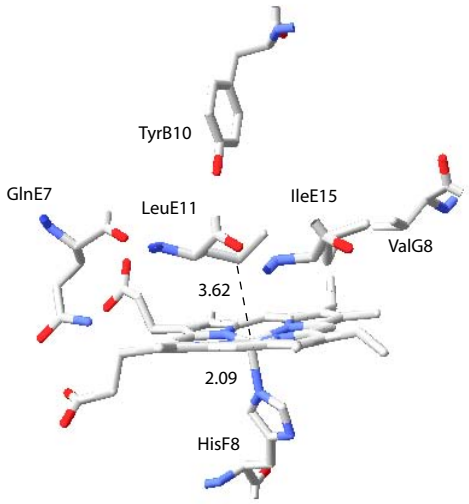

Figure 5.2: Details of the heme pocket in the unliganded ferric form of flavohemoglobin from *Escherichia coli*.

suggests a gate role of LeuE11 in the accommodation of the incoming ligand, in addition to the stabilization of a pentacoordinated ferric iron species [19]. This configuration is consistent with Resonance Raman results [30, 126]. The proximal region displays the highly conserved histidine residue that coordinates the ferric heme iron at 2.09 Å distance. This pentacoordinated structure is attributed to the strong iron-proximal histidine bond, that forces the iron out-of-plane and, consequently, inhibits the coordination of weak distal ligands to the heme. Similar to the peroxidases, the HMP shows an imidazolate character of the proximal histidine. Evidence of this specific interaction is found in the high frequency of the histidine stretching mode (244 cm^{-1}) in the ferrous protein and probably arises from a hydrogen bonding network on the proximal side of heme that imparts a rigid and tilted orientation of imidazole plane compared with the heme normal as well, in contrast with the vertebrate hemoglobins [126].

The comparison between the crystal structure of the active site of ferric HMP from *E.coli* and the ferrous lipid-bound flavohemoglobin from *Alcaligenes eutrophus* [30] shows a similar stereochemistry, in which the iron does not establish any bonding interaction at the distal site. In contrast, addition of the lipid to the ferric HMP brings to the formation of a exacoordinated species, as demonstrated from Resonance Raman and UV-

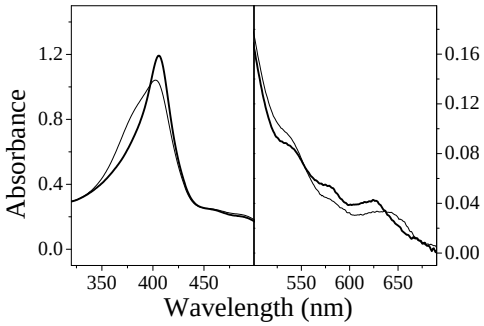

Figure 5.3: UV-vis absorption spectra of ferric *E.coli* HMP ligand-free (thin line) and palmitoleic acid bound (thick line). All spectra are in 0.1 M phosphate buffer at pH 7.0.

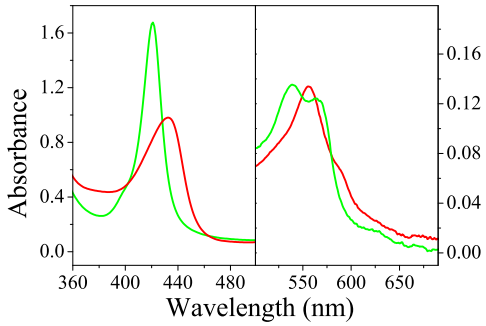

Figure 5.4: UV-vis absorption spectra of ferrous *E.coli deoxy*-HMP (red line) and its CO complex (green line). These spectra are not affected by the presence of fatty acids.

vis absorption data, EXAFS and XANES spectra [30]. These experimental evidences are consistent with an interaction between the ferric heme iron and the lipid. This interaction is found to be specific for unsatured and cyclopropane fatty acids, in which the double-bond or the cyclopropane moiety are responsible of a π electron donation to the ferric empty iron d_{z^2} orbital.

The photodynamics of flavohemoglobin has been investigated by transient absorption spectroscopy. The systems in study are the lipid-free and lipid-bound *deoxy*-HMPs, their CO complexes and the ferric forms.

The HMP samples have been kindly provided by Prof. Boffi (Department of Biochemical Sciences, University of Rome "La Sapienza", Italy) as ferric species in 0.1 M phosphate buffer at pH 7. The expression and purification processes have been previously reported [125]. The *deoxy*-HMP was prepared by adding sodium dithionite to the HMP samples in presence and in absence of palmitoleic acid; the CO adduct was prepared by flushing CO gas over the *deoxy*-HMP solution. The pump-probe experiments were carried out with ultrashort pump pulses at 400 nm in resonance with the Soret band, while white-light (410-650 nm) continuum pulses have provided the probe. The experimental set-up allows data acquisition up to 1.5 ns delay.

The steady-state absorption spectrum of the ferric is affected by the presence of the

palmitoleic acid. The spectrum of the lipid-free HMP, shown in Figure 5.3, displays a broad Soret (or B) band centered at 403 nm. In the visible region, a prominent charge transfer (CT) band is observed at 645 nm. The spectrum of the ferric HMP saturated with palmitoleic acid (lipid-bound HMP) shows a sharp peak at 407 nm and a CT band at 625 nm. The modification of the UV-vis absorption spectrum corresponds to a transition from a pentacoordinated (typical of a ligand-free protein) to a hexacoordinated, high spin, heme iron. This lipid-induced changes pertain only to the ferric species. It is noteworthy that the lipid-free and the lipid-bound HMPs, once reduced and complexed with CO, show the same spectrum. The main spectral features (see Figure 5.4) of the *deoxy* pentacoordinate high spin ferrous HMPs are the Soret band at 434 nm and the Q_v band at 555 with a shoulder around 590 nm (Q_0). No charge transfer bands are obviously observed. The CO binding brings to the formation of the exacoordinate low spin species, in which the narrower Soret band blue-shifts at 421 nm and two visible bands at 539 and 562 nm are resolved with similar extinction coefficients.

5.2 The photodynamics of reduced derivatives of HMP

Although the UV-vis absorption spectra of the reduced derivatives are not affected by the fatty acid, from the time-resolved experiments on *deoxy*-HMPs it emerges that the position and the spectral shape of transient signals depend on the presence of the palmitoleic acid. The Figure 5.5 shows that in the lipid-free *deoxy*-HMP the relaxation processes are completed in less than 50 ps, while a residual signal is observed in the lipid-bound sample. In Figure 5.6 the decays of the signals measured with the single wavelength technique at different wavelengths are reported. The fitting process involves the convolution of the instrumental function (pump-probe cross correlation function) of 160 fs with a multiexponential decay function. Well separated dynamic components are observed: a spike, appearing and decaying within the instrumental resolution, a several hundreds of femtoseconds component (0.3−0.4 ps) and a recovery of the ground state in the picosecond timescale (4−5 ps). The data recorded in lipid-bound *deoxy*-HMP sample show

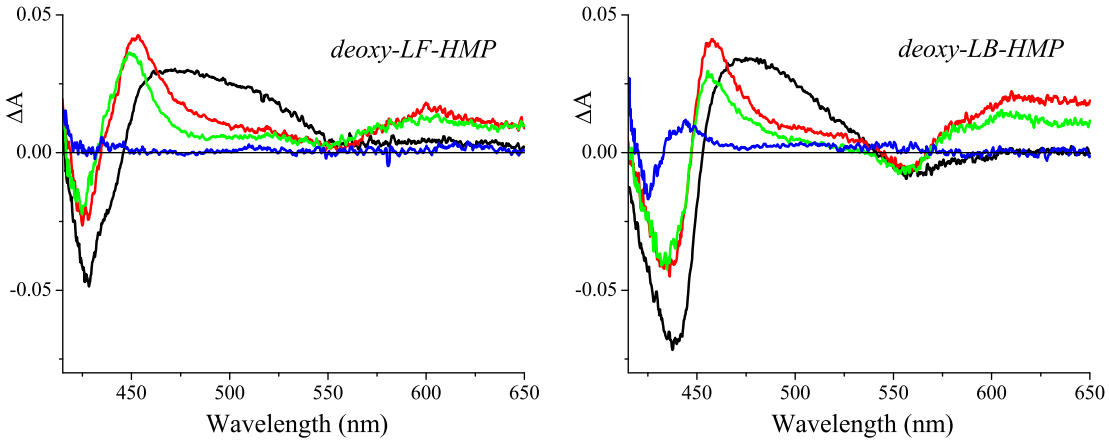

Figure 5.5: The transient absorption spectra of *deoxy*-HMP lipid-free (left) and lipid-bound (right) plotted as a function of the delay time between pump and probe pulses. The black, red, green and blue lines are recorded at 200 fs, 1 ps, 3 ps and 50 ps delay, respectively, after the excitation at 400 nm ($E = 1$ μJ/pulse). The absorbance at the pump wavelength was ≈ 0.5 of both the samples.

an other slower relaxation process (see Fig.5.6 and the transient spectrum at 50 ps in Fig.5.5) with a time constant of about 350 ps.

In the light of what we have shown up to this point, it seems meaningful to add the ferrous *E.coli* HMP decay profile to the Figure 4.10 just reported in Chapter 4. We observe in Figure 5.7 that all the decays are practically overlapped, although the heme environments are significantly different, revealing that any correlation of the vibrational cooling time with the protein structure is not straightforward. Following the analysis of the photodynamics in myoglobin [48], our data indicate that after a very rapid electronic decay the heme relaxes in the vibrationally hot ground electronic state. Then the excess energy is dissipated through vibrational cooling to the environment, the surrounding protein chain and, eventually, to the solvent, via the propionate groups of heme [54, 58, 119]. Under this assumption, the slowdown of the ground state recovery process in the lipid-bound HMP could be interpreted as due to the presence of the fatty acid deeply embedded in the heme pocket. This latter stiffens the distal pocket and reduces the coupling between the vibrational modes of the propionate groups and those of water

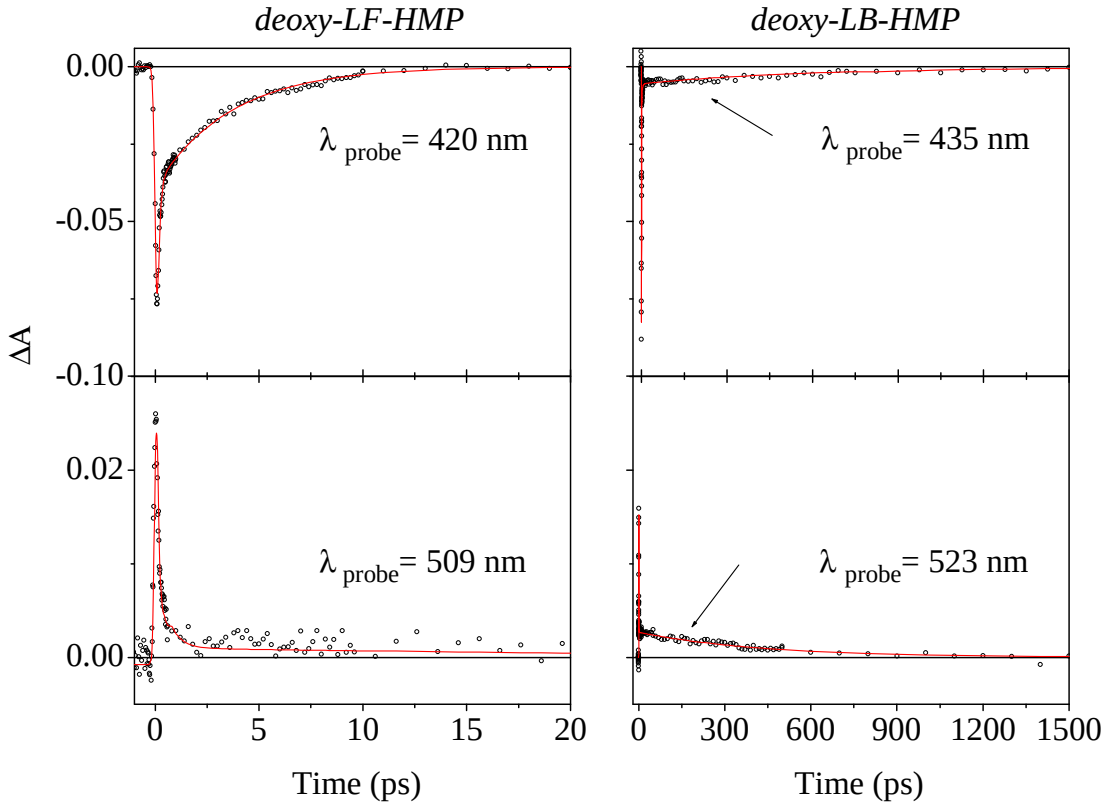

Figure 5.6: Time dependence of the transient signals at significant wavelengths. The decays are plotted on different timescales for the lipid-free *deoxy*-HMP (left) and lipid-bound *deoxy*-HMP (right) in order to underline the presence of a slow process in the latter sample. The arrows mark the slow relaxation process with time constant of 350 ± 50 ps, observed only in the ferrous derivative of the lipid-bound HMP.

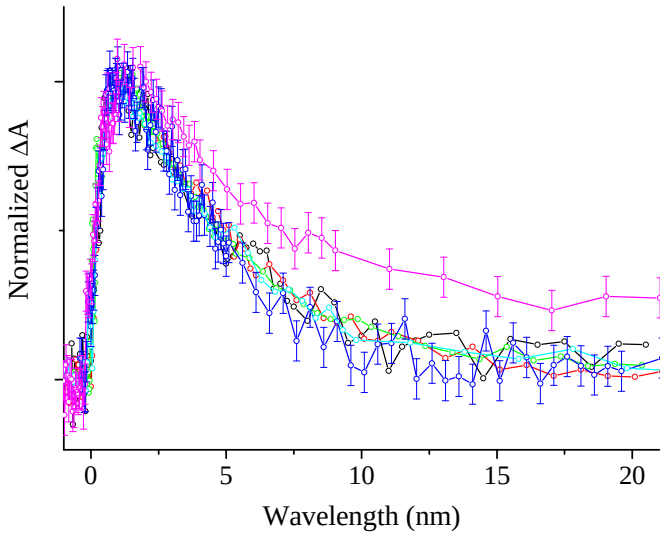

Figure 5.7: Comparison of the decays profiles in the *deoxy* form of different proteins, as probed at their respective antibleaching maxima. With the exception of lipid-bound HMP (magenta), *T.fusca* trHb (black) and its mutant TrpG8Phe (red), *B.subtilis* trHb (green) [76], Mb (blue) and lipid-free HMP (cyan) show a superimposing behavior.

molecules. As a consequence, the vibrational energy transfer and the whole protein conformational changes become slower in respect to the lipid-free protein.

A second hypothesis can be done to provide an explanation of the the slow relaxation process in the lipid-bound HMP. Taking into account the mechanism proposed by Franzen and coworker [45] that determines the excited states decay of heme, we can consider the presence of such a long time as an evidence of a direct interaction between the iron and the lipid. Charge-transfer states have been considered by the authors of ref.[45], in which an electron flux from iron towards the porphyrin macrocycle occurs. The formation of the high spin d^5 Fe(III) CT state can originate a new short-lived species formed from the interaction between the π electrons of the lipid and the excited state iron, i.e. an exciplex. As we have seen from the steady-state absorption spectra, the lipid-iron coordination is a peculiarity of the ferric state. Therefore, the time constant of 350 ps could be assigned to the lifetime of this transient species. The validity of the two interpretations is strictly correlated to the model applied for the description of the photodynamics of the heme. We have already pointed out that the unification of the hemoprotein dynamics interpretation

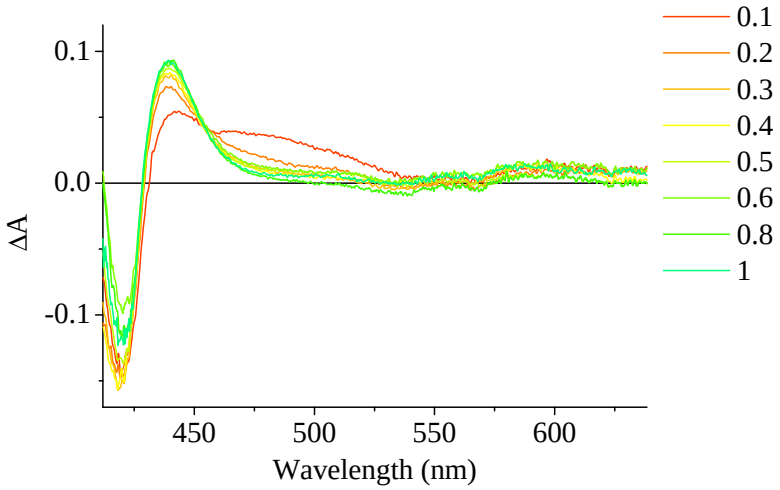

Figure 5.8: Transient absorption spectra recorded in the CO adduct of the lipid-free HMP, excited at 400 nm ($E = 1.2$ μJ/pulse). The absorbance of the sample is 1.4 at the Soret maximum. The delay times between pump and probe are reported in the legend, expressed in ps.

has not be achieved yet and more efforts must be done in order to understand it. However, considering that a relaxation time of few hundred picoseconds is very long for a vibrational cooling process, our data suggest that the charge transfer processes can play an important role in the photodynamics of heme.

To gain insight into the heme pocket and the lipid-heme interaction, the carbon monoxide would represent an excellent probe for investigating the dynamics of ligand entry/escape. Unfortunately, no evidence of any geminate recombination has been found in the sub-nanosecond timescale and the relaxation dynamics, following the photodetached of CO, are similar in both lipid-free and lipid-bound protein. For the sake of completeness, we show the transient spectra of the CO adduct of the lipid-free HMP recorded in the first picosecond in Figure 5.8 and the kinetics profiles in Figure 5.9, compared with the behavior recorded in lipid-bound protein. The scattered pump light can impinge the detector and deforms the signal, this effect is relevant up around 420 nm and seems to be enhanced in the lipid-bound samples, for which we were not able to obtain a defined shape of the Soret bleaching. After the release of the ligand that occurs in less than 50 fs [56], different contributions are clearly observed in the spectra: the instantaneous

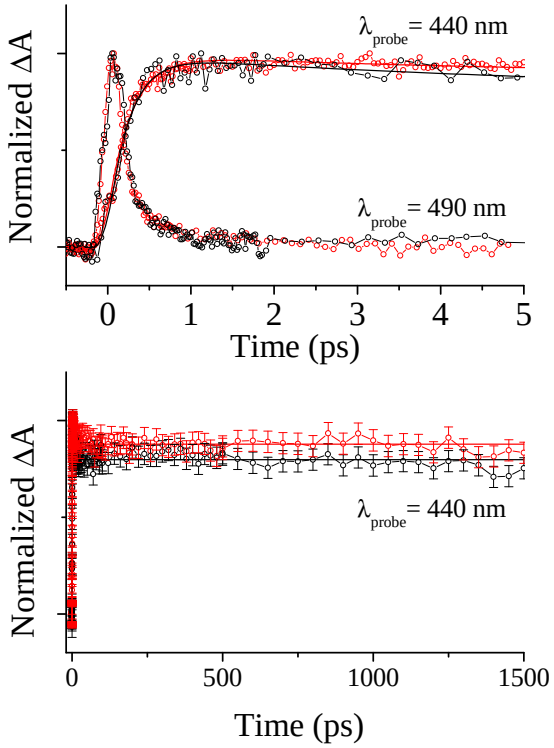

Figure 5.9: Comparison between the kinetic profiles recorded in the CO adducts of lipid-free HMP (black line) and lipid-bound HMP (red line) at two different wavelengths. The experimental conditions are the same just reported in the caption of Fig.5.8.

bleaching of the Soret and of the Q bands and a broad transient absorption band. In the first picoseconds the band becomes narrower and more intense, until the spectra resembles the static difference spectrum (see Figure 5.10), scaled by a proper factor.

The positive signal corresponds to the antibleaching due to the formation of the pentacoordinated *deoxy* form. Vibrational relaxation is the main mechanism in the first picoseconds, but the presence of an isosbestic point can be reasonably attributed to an excited electronic state relaxing into the ground state. The most likely interpretation is that the signal arises from the combination of different contributions: an electronic relaxation (0.3 ± 0.1 ps) and a second process mainly correlated to the vibrational cooling, occurring in 6 ± 1 ps.

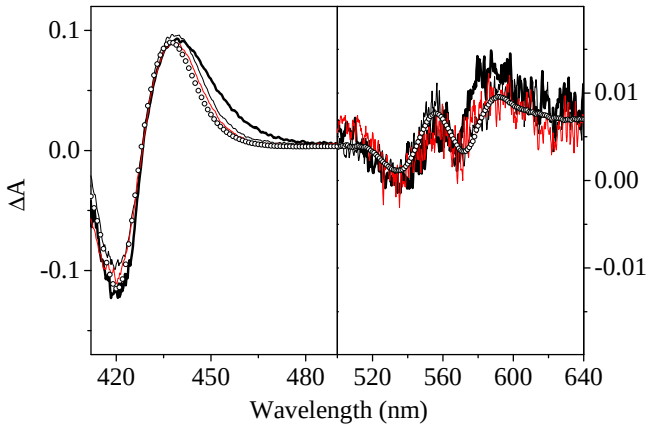

Figure 5.10: The static difference spectrum is compared with the transient absorption spectra recorded in the CO adduct of the lipid-free HMP, recorded at several chosen time delays: at 1 ps (thick black line), at 10 ps (thin black line) and at 1.5 ns (red line). The static spectrum is represented by open circles.

However the latter process is a slightly longer than the analogous process observed in the *deoxy* forms ($\approx 4-5$ ps); this suggests that a very fast geminate recombination takes place in parallel [76]. The weight of the 6 ps component is higher in the lipid-free (20%) than in the lipid-bound HMP (12%) and such observation is consistent with the hypothesis that in the latter form the fatty acid disturbs the fast geminate recombination. In Figure 5.9 (lower), it is possible to observe that the discrepancy is very low and the decay profiles recorded at 440 nm can be superimposed in the limit of the error bars. So

we can conclude that, even if we can not completely ruled out the presence of a very fast CO rebinding, the dominant relaxation process is the geminate recombination occurring on a timescale longer than that accessible to our instrumentation.

5.3 The photodynamics of ferric HMP

To the beginning of this chapter, we have observed that besides the heme, another prosthetic group is present in the HMP: the FAD (flavin adenine dinucleotide). It is an highly photosensitive chromophore that could be assumed to be in active communication with the heme moiety. The isoalloxazine ring of FAD undergoes reversible reduction, accepting either one or two electrons brought by one or two hydrogen atoms from a reduced substrate [127]. The fully reduced forms are abbreviated $FADH_2$. When FAD accepts only one electron (one hydrogen atom), the semiquinone form of the isoalloxazine ring is produced. It is a stable free radical species.

The absorption and fluorescence spectra of FAD in the HMP are reported in Figure 5.11, where two absorption maxima at 380 nm and at 450 nm are observed. It is known that in general the fully reduced flavoproteins have an absorption maximum near 360 nm [127].

The measured value of the fluorescence quantum yield of ferric lipid-free HMP is 8×10^{-3} [128]. In the pH range from 4 to 9 the fluorescence quantum yield of FAD in water solution is approximately constant at 0.033 [129]. This reduced value can be considered as the effect of the interaction between the chromophore and the protein matrix that preludes new energy deactivation channels. Optical triggering can be achieved also through primary photophysical processes such as energy and charge (electron) transfer processes which occur, depending on the distance between donor and acceptor, on the picosecond timescale. Thus, we have performed transient absorption spectroscopy with the aim to characterize the kinetic parameters of the photodynamics following the excitation of the HMP at different wavelengths.

The idea is to identify the transient spectra ascribable to each chromophore, i.e. the

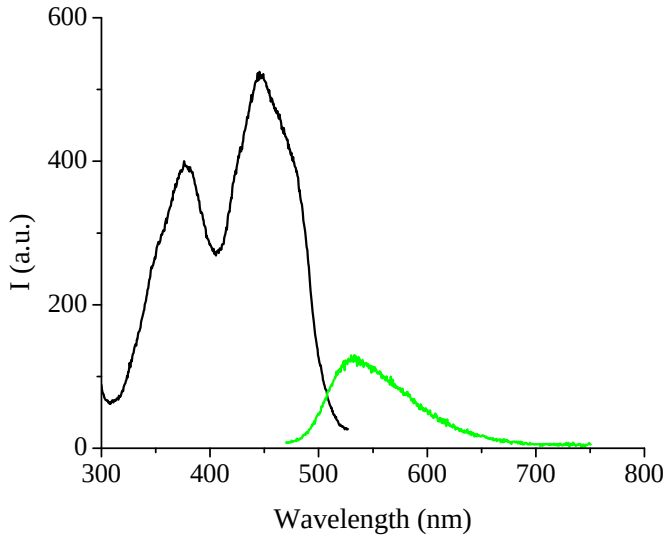

Figure 5.11: Excitation (black line) and emission (green line) spectra of the flavohemoglobin from *E.coli* in 0.1 M phosphate buffer at pH 7. The excitation spectrum with $\lambda_{EM} = 540$ nm in correspondence with the FAD emission, allows to estimate the absorption profile of this chromophore. The emission spectrum is obtained by exciting the sample at 450 nm.

donor (the flavin) and the acceptor (the heme) in order to detail the presumed energy transfer process. The final goal of this investigation is an ambitious one, it concerns the understanding of the protein functioning at the atomic level. The present results represent a first small step in this direction.

First of all, we observe that after irradiation the HMP samples become opalescent, probably as a consequence of protein aggregates formation. The position and the shape of the bands in the steady-state spectra before and after the time-resolved experiments remain essentially unchanged, but the reduced clearness of the solution causes a large instability in the *baseline* during the experiments. This is the main reason why it is practically impossible to follow the time-dependent variation of the signals when it goes lower than 0.005.

The transient spectra reported here were obtained by exciting at 360, 400 and 450 nm. These three wavelengths correspond to excitation of both chromophore, of heme (mostly) and of FAD, respectively.

The transient spectra of Figure 5.12 correspond to the latter case, i.e. to the $S_0 \rightarrow$

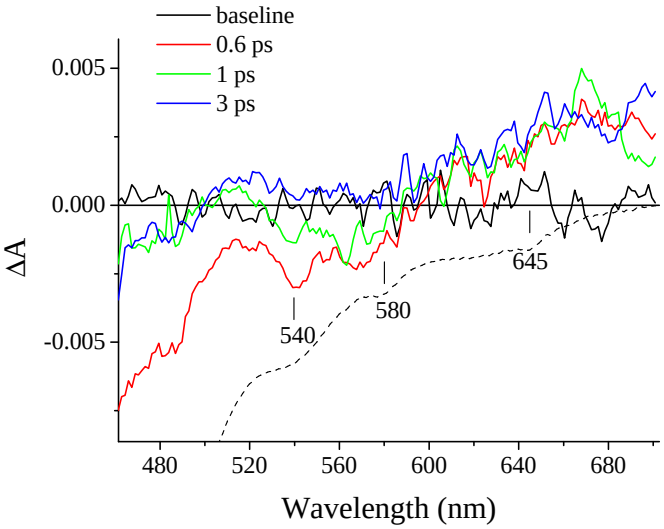

Figure 5.12: Transient absorption spectra of lipid-free HMP, exciting at 450 nm (E = 0.5 μJ/pulse), at different delay time between pump and probe. The baseline is shown among the spectra. In dashed line the inverse steady-state absorption profile is also displayed in order to unravel the contributions from heme.

S_1 transition of FAD. At all the delay time times, the signal is very low. The absorbance of the protein at 450 is 0.35, and the concentration of the protein can not be increased because the solution would become too much opalescent. Another difficulty is in spatially separating spatially the pump from the probe beam. In fact, the pump at 450 nm falls inside the probed spectral range, and the scattered pump light makes the transient spectra of Figure 5.12 of a lower quality than those obtained after the excitation at 400 nm and at 360 nm. In order to avoid that the pump beam impinges the detector a cut-off filter is put after the sample in both the pump and probe paths, and the transient signal at wavelengths lower than the pump is not recorded. The observed spectral features agree with those obtained elsewhere for FAD in water [130]. The negative tail starting from the blue side of the spectra is ascribed to ground state bleaching for the excited transition. The increased absorption peaked at about 510 nm is thought to be an excited state absorption (ESA, $S_1 \rightarrow S_n$). The two negative peaks coincide with the Q band (vibronic structure) of the heme, and a second ESA band is observed growing in beyond 600 nm. We tried to extract from the spectra the kinetic profiles at single wavelengths,

but the low S/N ratio does not allow us to estimate the time constants. Nevertheless, it is possible to note that, at early delay times, the bleaching of the heme ground state is observed, indicating that this chromophore is directly excited also at 450 nm. It is then very difficult to find the appropriate excitation wavelengths to excite separately and independently the two chromophores. Due to the low absorbance value at the excitation wavelength a strong artifact related to the XPM (cross-phase modulation) [82] is observed in the first hundreds of femtoseconds, that obscures transient absorption data at very short times.

Pumping at 360 nm, both chromophores are excited; the transient spectra are reported in Figure 5.13. The Soret bleaching appears instantaneously with a broad ESA band around 450 nm. In the first picosecond, the band narrows and rapidly decays, involving a blue-shift of the maximum. The bleaching decay is related to the ground state recovery time and two time constants can be found from the kinetic profile extrapolated at 405 nm. The short component of 0.6 ± 0.2 ps contributes by 80 % of the entire decay process, while a second longer and weaker time constant of 10 ± 5 ps is detected, consistent with a vibrational cooling process. The transient signals are dominated by

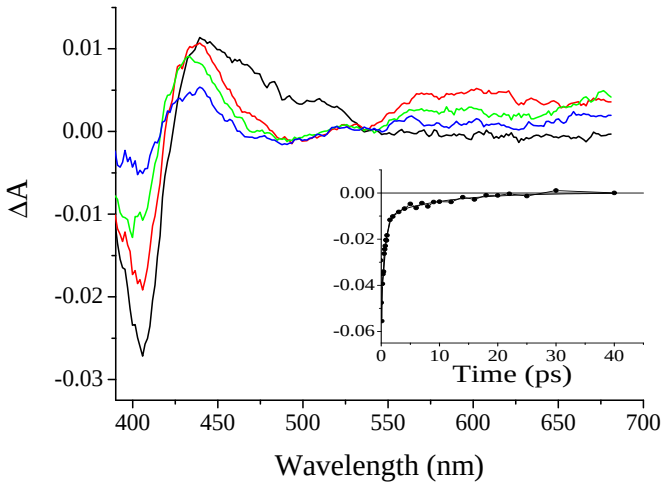

Figure 5.13: Transient absorption spectra of lipid-free HMP, exciting at 360 nm (E = 0.6 μJ/pulse), at different delay time between pump and probe: 0.5, 1, 2 and 5 ps in black, red, green and blue lines, respectively. The spectra are not corrected for the GVD. In the inset, the kinetic profile at 405 nm.

the contribution from the heme. No relevant difference can be seen (see Figure 5.14) in the transient spectra measured on the lipid-free HMP at 1 ps delay, after excitation at 360 and 400 nm. In the latter case, we only note an increase of ΔA around 450 nnm, probably due to the absence of the bleaching contribution of the directly excited FAD at 360 nm.

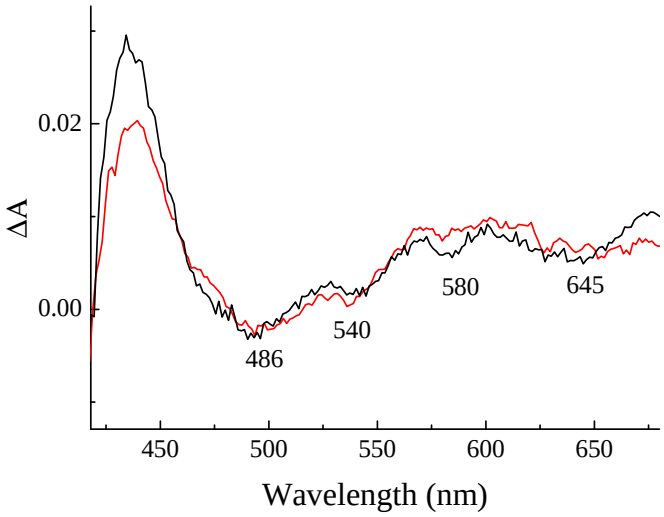

Figure 5.14: Transient absorption spectra of lipid-free HMP, exciting at 360 nm (red line) and at 400 nm (black line). Both spectra are recorded at 1 ps delay time and are normalized in correspondent to the bleaching of the Q band.

We also recorded the time evolution of the transient spectra of the lipid-free and of the lipid-bound HMP, upon photoexcitation in the Soret band (at 400 nm). In the first case, the decay of the transient signal is complete after around 30−40 ps. Instead, for the lipid-bound protein, a small residue of the signal (ΔA $\approx$ 0.002) is left even at 1.5 ns, as to indicate that the ground state is not completely recovered in this timescale. However, the intensity of this signal is very low and we can not dismiss the possibility that this contribution is originated by spurious components such as scattered light, deforming the flatness of the *baseline*.

In summary, we have presented the results of a study on lipid-free and lipid-bound flavohemoglobin from *Escherichia coli* investigated by exciting the sample in the Soret band. The experiments carried out on lipid-bound HMP reveal the slowest relaxation

process with a time constant of ≈ 350 ps that is not observed when the protein is lipid-free, suggesting that the lipid is strongly embedded in the heme pocket.

Conclusions

In this thesis we have presented a dynamical and spectroscopical characterization of porphyrins and bacterial "hemoglobin-like" proteins . The transient absorption experiments allowed us to discuss the photophysical properties of such systems in the femtosecond-nanosecond time domain upon photoexcitation with UV-visible pulses of femtosecond duration.

The results can be summarized as follows:

- Different porphyrinic systems in solution at room temperature have been studied: unsubstituted porphyrin (H_2P), diprotonated porphyrin (H_4P^{2+}), and the isoelectronic tetraoxaporphyrin dication ($TOxP^{2+}$). All of these molecular species fluoresce not only from S_1 (or Q state) but also from S_2 (or B state). Fluorescence quantum yields and lifetimes have been determined. The $S_2 \rightarrow S_0$ spectrum of $TOxP^{2+}$ has been easily observed due to peculiar features of the system, i.e., the high $S_0 \rightarrow S_2$ oscillator strength, the large S_2-S_1 energy gap, and the absence of intermediate states. On the contrary, the S_2 fluorescence spectra of H_2P and H_4P^{2+} are perturbed in comparison to $TOxP^{2+}$ (i.e., they are considerably red-shifted from the absorption band and more extended). We discussed these spectral differences in terms of variation of the equilibrium geometry upon excitation and, in the case of H_4P^{2+}, of the nonplanar conformation of the macrocycle. Internal conversion from the S_2 state to the adjacent lower state plays the most impor-

tant role in the decay processes. As the energy separation widens on going from $\Delta E(B - Q_y) \approx 6100$ cm^{-1} in PH_2 to $\Delta E(B - Q) \approx 9370$ cm^{-1} in $TOxP^{2+}$, the time constant of the internal conversion increases from ≈ 50 fs to 25 ps, with a variation of more than 2 orders of magnitude. On the other hand, internal conversion in H_4P^{2+} involves charge transfer (CT) states due to electron promotion from occupied molecular orbitals localized on the counterion to those on the porphyrin macrocycle. These states lye energetically between B and Q and favor the $B \rightarrow Q$ decay through the indirect step $B \rightarrow$ CT (≈ 300 fs). This latter result shines new light on the relevance of CT processes in modulating the relaxation dynamics of porphyrins.

- Our transient absorption data support the hypothesis that in hemoproteins fast relaxation processes occur due to the charge transfer from the metal to the porphyrin macrocycle. After photoexcitation in the Soret band of reduced derivatives of different hemoglobins (horse heart myoglobin, truncated hemoglobin from *Thermobifida fusca* and flavohemoglobin from *Escherichia coli*), transient spectroscopic changes arise from electronic and vibrational relaxation of the heme. Two components are observed: a few hundred femtosecond component (≈ 300 fs) and a picosecond (≈ 4 ps) component. The similarity of these time constants in different hemoproteins is considered as the evidence that the heme environment does not significantly influence the relaxation dynamics of the photoexcited heme. The presence of an electron-donating group such as double bond system of an unsaturated fatty acid induces the appearance of an excimer-like interaction. This is a new effect never observed in previous investigation of hemoglobins, and it can help to characterize the nature of short-living excited states of the heme group.

- On the other hand, the nature of amino acids around the prosthetic group, i.e. the heme pocket, affects the geminate recombination rate of exogenous ligands, such as carbon monoxide. If the rate of geminate rebinding is enhanced, it must be because the barrier to the diffusion of the ligand away from the heme has increased.

In flavohemoglobin from *Escherichia coli* the transient signal is dominated by the geminate recombination occurring on a timescale longer than that accessible to our instrument, while the truncated hemoglobin from *Thermobifida fusca* (Tf-trHb) displays a fast geminate recombination with time constant of 3−4 ns, suggesting an enclosed distal heme pocket. The mutation in the topological site G8 of tryptophan to phenylalanine introduces a new ultrafast geminate phase. The CO recombination process can be fitted with a double exponential function with time constants of 400−500 ps (≈ 60 %) and of 3−4 ns. The reported analysis shows that the geminate recombination in the picosecond timescale is related to the rebinding of the CO within the distal pocket, and the appearance of two phases can be attributed to the CO rebinding from different locations. We found that TrpG8 is important in the stabilization of the heme-bound ligand and its mutation strongly modifies the interaction within the heme pocket.

Further ultrafast spectroscopic experiments should be done on different mutants at the distal topological positions in order to unravel the interaction of the heme with its environment, and in particular with the nearby dissociated ligand.

Appendix A

List of acronyms and abbreviations

AB	antibleaching
Ala or A	alanine
B	bleaching
Bs-trHb	truncated hemoglobin from *Bacillus subtilis*
CT	charge transfer
DAS	decay associated spectrum
E	glutamic acid
ESA	excited state absorption
EXAFS	extended X-ray absorption fine scectroscopy
FAD	flavin adenine dinucleotide
FHb	flavohemoglobin
FHP	flavohemoglobin from *Alcaligenes eutropus*
FWHM	full width half maximum
GCS	global-coupled sensor protein
Gln or Q	glutamine
Gly or G	glycine
GVD	group velocity dispersion

GVM	group velocity mismatch
H_2P	unsubstituted porphyrin or porphine
H_4P^{2+}	diprotonated porphyrin
Hb	hemoglobin
HbCO	carboxyhemoglobin
His or H	histidine
HMP	flavohemoglobin from *Escherichia coli*
HS	high spin
IC	internal conversion
Ile or I	isoleucine
IVR	intramolecular vibration redistribution
Leu or L	leucine
LS	low spin
M	methionine
Mb	myoglobin
MbCO	carboxymyoglobin
Mt-trHb or HbO	truncated hemoglobin from *Mycobacterium tuberculosis*
NAD	nicotinamide adenine dinucleotide
OD	optical density
OKE	Optical Kerr effect
PDB	protein data bank
Phe or F	phenylalanine
R	arginine
SE	stimulated emission
SRG	stimulated Raman gain
SVD	sinlge value decomposition
TA	transient absorption
TAS	transient absorption spectroscopy
Tf-trHb	truncated hemoglobin from *Thermobifida fusca*

Thr or T	threonine
$TOxP^{2+}$	tetraoxaporphyrin dication
TPA	two-photon absorption
trHb	truncated hemoglobin
trHbN	group I trHb
trHbO	group II trHb
trHbP	group III trHb
Trp or W	tryptophan
Tyr or Y	tyrosine
Val or V	valine
VER	intermolecular vibrational energy relaxation
VHb	hemoglobin from *Vitreoscilla*
VR	vibrational relaxation
XANES	X-ray absorption near edge spectroscopy
XPM	cross-phase modulation

Bibliography

[1] Brunori, M., Cutruzzolà, F., Savino, C., Travaglini-Allocatelli, C., Vallone, B., and Gibson, Q. H. *Trends Biochem. Sci.* **24**, 253–255 (1999).

[2] Hardison, R. C. *Proc. Natl. Acad. Sci.* **93**, 5675–5679 (1996).

[3] Vinogradov, S. N., Hoogewijs, D., Bailly, X., Mizuguchi, K., Dewilde, S., Moens, L., and Vanfleteren, J. R. *Gene* **398**, 132–142 (2007).

[4] Freitas, T. A., Hou, S., Dioum, E. M., Saito, J. A., Newhouse, J., Gonzalez, G., Gilles-Gonzalez, M. A., and Alam, M. *Proc. Natl. Acad. Sci.* **101**, 6675–6680 (2004).

[5] Cossins, A. and Berenbrink, M. *Nature* **454**, 416–417 (2008).

[6] Gardner, P. R., Gardner, A. M., Martin, L. A., Dou, Y., Li, T., Olson, J. S., Zhu, H., and Riggs, A. F. *J. Biol. Chem.* **275**, 31581–31587 (2000).

[7] Pesce, A., Nardini, M., Milani, M., and Bolognesi, M. *Life* **59**, 535–541 (2007).

[8] Pesce, A., Couture, M., Dewilde, S., Guertin, M., Yamauchi, K., Ascenzi, P., Moens, L., and Bolognesi, M. *EMBO J.* **19**, 2424–2434 (2000).

[9] Hargrove, M. S., Krzywda, S., Wilkinson, A. J., Dou, Y., Ikeda-Saito, M., and Olson, J. S. *Biochemistry* **33**, 11767–11775 (1994).

[10] Wittenberg, J. B., Bolognesi, M., Wittenberg, B. A., and Guertin, M. *J. Biol. Chem.* **277**, 871–874 (2002).

[11] Vuletich, D. A. and Lecomte, J. T. J. *J. Mol. Evol.* **62**, 196–210 (2006).

[12] Sato, T. and Tamiya, H. *Cytologia, Fujii Jubilee volume* , 1133–1138 (1937).

[13] Keilin, D. and Ryley, J. *Nature* **172**, 451 (1953).

[14] Iwaasa, H., Takagi, T., and Shikama, K. *J. Mol. Biol.* **208**, 355–358 (1989).

[15] Milani, M., Savard, P.-Y., Ouellet, H., Ascenzi, P., Guertin, M., and Bolognesi, M. *Proc. Natl. Acad. Sci.* **100**, 5766–5771 (2003).

[16] Nardini, M., Pesce, A., Milani, M., and Bolognesi, M. *Gene* **398**, 2–11 (2007).

[17] Hoy, J. A., Kundu, S., Trent, J. T., Ramaswamy, S., and Hargrove, M. S. *J. Am. Chem. Soc.* **279**, 16535–16542 (2004).

[18] Bolognesi, M., Rosano, C., Losso, R., Borassi, A., Rizzi, M., Wittenberg, J. B., Boffi, A., and Ascenzi, P. *Biophys. J.* **77**, 1093–1099 (1997).

[19] Ilari, A., Bonamore, A., Farina, A., Johnson, K. A., and Boffi, A. *J. Biol. Chem.* **277**, 23725–732 (2002).

[20] Falzone, C. J., Vu, B. C., Scott, N. L., and Lecomte, J. T. *J. Mol. Biol.* **324**, 1015–1029 (2002).

[21] Milani, M., Pesce, A., Ouellet, Y., Ascenzi, P., Guertin, M., and Bolognesi, M. *EMBO J.* **20**, 3902–3909 (2001).

[22] Giangiacomo, L., Ilari, A., Boffi, A., Morea, V., and Chiancone, E. *J. Biol. Chem.* **280**, 9192–9202 (2005).

[23] Bonamore, A., Ilari, A., Giangiacomo, L., Bellelli, A., Morea, V., and Boffi, A. *FEBS Lett.* **272**, 4189–4201 (2005).

[24] Nardini, M., Pesce, A., Labarre, M., Richard, C., Bolli, A., Ascenzi, P., M. Guertin, M. M., and Bolognesi, M. *J. Biol. Chem.* **281**, 37803–37812 (2006).

[25] Gardner, A. M., Martin, L. A., Gardner, P. R., Dou, Y., and Olson, J. S. *J. Biol. Chem.* **275**, 12581–12589 (2000).

[26] Ermler, U., Siddiqui, R. A., Cramm, R., and Friedrich., B. *EMBO J.* **14**, 6067–6077 (1995).

[27] Ollesch, G., Kaunzinger, A., Juchelka, D., Schubert-Zsilavec, M., and Ermler., U. *Eur. J. Biochem.* **262**, 396–405 (1999).

[28] Ramandeep, Hwang, K. W., Raje, M., Kim, K.-J., Stark, B. C., Dikshit, K. L., and Webster, D. A. *J. Biol. Chem.* **276**, 24781–24789 (2001).

[29] Pathania, R., Navani, N. K., Rajamohan, G., and Dikshit, K. L. *J. Biol. Chem.* **277**, 15293–302 (2002).

[30] D'Angelo, P., Lucarelli, D., della Longa, S., Benfatto, M., Hazemann, J. L., Feis, A., Smulevich, G., Ilari, A., Bonamore, A., and Boffi, A. *Biophys. J.* **86**, 3882–3892 (2004).

[31] Gouterman, M. *The Porphyrins.* D. Dolphin Ed. Academic Press, (1978).

[32] *Iron Porphyrins, Part I.* Edited by A. B. P. Lever and Harry B. Gray, (1983).

[33] Dixon, D. W., Kirmaier, C., and Holten, D. *J. Am. Chem. Soc.* **107**, 808–813 (1985).

[34] Rodriguez, J., Kilmaier, C., and Holten, D. *J. Am. Chem. Soc.* **111**, 6500 (1989).

[35] Rodriguez, J., Kilmaier, C., and Holten, D. *J. Chem. Phys.* **94**, 6020–6029 (1991).

[36] Shank, C. V. and Ippen, E. P. *Science* **193**, 50–51 (1976).

[37] Greene, B. I., Hochstrasser, R. M., Weisman, R. B., and Eaton, W. A. *Proc. Natl. Acad. Sci.* **75**, 5255–5259 (1978).

[38] Chernoff, D. A., Hochstrasser, R. M., and Steele, A. W. *Proc. Natl. Acad. Sci.* **77**, 5606–5610 (1980).

[39] Eaton, W. A., Hanson, L. K., Stephens, P. J., Sutherland, J. C., and Dunn, J. B. R. *J. Am. Chem. Soc.* **100**, 4991–5003 (1978).

[40] Cornelius, P. A., Steele, A. W., Chernoff, D. A., and Hochstrasser, R. M. *Proc. Natl. Acad. Sci.* **78**, 7526–7529 (1981).

[41] Martin, J.-L., Migus, A., Poyart, C., Lecarpentier, Y., Astier, R., and Antonetti, A. *Proc. Natl. Acad. Sci.* **80**, 173–177 (1983).

[42] Petrich, J. W., Martin, J.-L., Houde, D., Poyart, C., and Orszag, A. *Biochemistry* **26**, 7914–7923 (1987).

[43] Martin, J.-L. and Vos, M. H. *Annu. Rev. Biophys. Biomol. Struct.* **21**, 199–222 (1992).

[44] Petrich, J. W., Poyart, C., and Martin, J.-L. *Biochemistry* **27**, 4049–4060 (1988).

[45] Franzen, S., Kiger, L., Poyart, C., and Martin, J.-L. *Biophys. J.* **80**, 2372–2385 (2001).

[46] Franzen, S., Bohn, B., Poyart, C., DePillis, G., Boxer, S. G., and Martin, J.-L. *J. Biol. Chem.* **270**, 1718–1720 (1995).

[47] Franzen, S., Bohn, B., Poyart, C., and Martin, J.-L. *Biochemistry* **34**, 1224–1237 (1995).

[48] Kholodenko, Y., Volk, M., Gooding, E., and Hochstrasser, R. M. *Chem. Phys.* **259**, 71–87 (2000).

[49] Miller, R. J. D. *Annu. Rev. Phys. Chem.* **42**, 581 (1991).

[50] Lingle, R., Xu, X., Zhu, H. P., Yu, S. C., and Hopkins, J. B. *J. Phys. Chem.* **95**, 9320 (1991).

[51] Mizutani, Y. and Kitagawa, T. *Science* **278**, 443 (1997).

[52] Lim, M. H., Jackson, T. A., and Anfinrud, P. A. *J. Phys. Chem.* **100**, 12043–12051 (1996).

[53] Harvey, J. N. *J. Am. Chem. Soc.* **122**, 12401–12402 (2000).

[54] Sagnella, D. E. and Straub, J. E. *J. Phys. Chem. B* **105**, 7057–7063 (2001).

[55] Dreuw, A., Dunietz, B. D., and Head-Gordon, M. *J. Am. Chem. Soc.* **124**, 12070–12071 (2002).

[56] Dunietz, B. D., Dreuw, A., and Head-Gordon, M. *J. Phys. Chem. B* **107**, 5623–5629 (2003).

[57] Ugalde, J. M., Dunietz, B., Dreuw, A., Head-Gordon, M., and Boyd, R. J. *J. Phys. Chem. A* **108**, 4653 (2004).

[58] Ye, X., Demidov, A., Rosca, F., Wang, W., Kumar, A., Ionascu, D., Zhu, L., Barrick, D., Wharton, D., and Champion, P. M. *J. Phys. Chem. A* **107**, 8156–8165 (2003).

[59] Ye, X., Demidov, A., and Champion, P. M. *J. Am. Chem. Soc.* **124**, 5914–5924 (2002).

[60] Vos, M. H. *Biochim. Biophys. Acta* **1777**, 15–31 (2008).

[61] Vojtěchovský, J., Chu, K., Berendzen, J., Sweet, R. M., and Schlichting, I. *Biophys. J.* **77**, 2153–2174 (1999).

[62] Lim, M. H., Jackson, T. A., and Anfinrud, P. A. *Nat. Struct. Biol.* **4**, 209–214 (1997).

[63] Šrajer, V., Teng, T.-Y., Ursby, T., Pradervand, C., Ren, Z., Adachi, S., Schildkamp, W., Bourgeois, D., Wulff, M., and Moffat, K. *Science* **274**, 1726–1729 (1996).

[64] Šrajer, V., Ren, Z., Teng, T.-Y., Schimidt, M., Ursby, T., , Bourgeois, D., Pradervand, C., Schildkamp, W., Wulff, M., and Moffat, K. *Biochemistry* **40**, 13802–13815 (2001).

[65] Schotte, F., Lim, M., Jackson, T. A., Smirnov, A. V., Soman, J., Olson, J. S., Phillips, G. N., Wulff, M., and Anfinrud, P. A. *Science* **300**, 1944–1947 (2003).

[66] Bossa, C., Anselmi, M., Roccatano, D., Amadei, A., Vallone, B., Brunori, M., and Di Nola, A. *Biophys. J.* **86**, 3855–3862 (2004).

[67] Anselmi, M., Di Nola, A., and Amadei, A. *Biophys. J.* **94**, 4277–4281 (2008).

[68] Petrich, J. W., Lambry, J.-C., Kuczera, K., Karplus, M., Poyart, C., and Martin, J.-L. *Biochemistry* **30**, 3975–3987 (1991).

[69] Chowdhury, P. K., Kundu, S., Halder, M., Das, K., Hargrove, M. S., and Petrich, J. W. *J. Phys. Chem. B* **107**, 9122–9127 (2003).

[70] Kuczera, K., Lambry, J.-C., Martin, J.-L., and Karplus, M. *Proc. Natl. Acad. Sci.* **90**, 5805–5807 (1993).

[71] Cornelius, P. A., Hochstrasser, R. M., and Steele, A. W. *J. Mol. Biol.* **163**, 119–128 (1983).

[72] Lim, M. H., Jackson, T. A., and Anfinrud, P. A. *J. Biol. Inorg. Chem.* **2**, 531–536 (1997).

[73] Silkstone, G., Jasaitis, A., Vos, M. H., and Wilson, M. T. *Dalton Trans.* **21**, 3489–3494 (2005).

[74] Silkstone, G., Jasaitis, A., Wilson, M. T., and Vos, M. H. *J. Biol. Chem.* **282**, 1638–1649 (2007).

[75] Ouellet, H., Juszczak, L., Dantsker, D., Samuni, U., Ouellet, Y. H. B., Wittenberg, B. A., Friedman, J. M., and Guertin, M. *Biochemistry* **42**, 5764–5774 (2003).

[76] Feis, A., Lapini, A., Catacchio, B., Brogioni, S., Foggi, P., Chiancone, E., Boffi, A., and Smulevich, G. *Biochemistry* **47**, 902–910 (2008).

[77] Bayanov, I. M., Danielius, R., Heinz, P., and Seilmeier, A. *Opt. Commun.* **113**, 99 (1994).

[78] Danielius, R., Piskarskas, A., Di Trapani, P., Andreoni, A., Solcia, C., and Foggi, P. *Appl. Opt.* **35**, 5336 (1996).

[79] Neuwahl, F. V. R., Bussotti, L., and Foggi, P. *Res. Adv. In Photochem. & Photobiol.* **1**, 77 (2000).

[80] Rullière C. (Ed.). *Femtosecond Laser Pulses. Principles and Experiments.* Springer, New York, (2004).

[81] Schmidt, M., Rajagopal, S., Ren, Z., and Moffat, K. *Biophys. J.* **84**, 2112–2129 (2002).

[82] Lorenc, M., Ziólek, M., Lorenc, M., Naskręcki, R., Karolczak, J., Kubicki, J., and Maciejewski, A. *Appl. Phys. B* **74**, 19–27 (2002).

[83] Ziólek, M., Lorenc, M., and Naskręcki, R. *Appl. Phys. B* **72**, 843–847 (2001).

[84] D'Souza, F., Gadde, S., Shafiqul Islam, D.-M., Wijesinghe, C. A., Schumacher, A. L., Zandler, M. E., Araki, Y., and Ito, O. *J. Phys. Chem. A* **111**, 8552–8560 (2007).

[85] Kuciauskas, D., Liddel, P. A., Lin, S., Stone, S. G., Moore, A. L., Moore, T. A., and Gust, D. J. *J. Phys. Chem. B* **104**, 4307–4321 (2000).

[86] Ogawa, K., Zhang, T., Yoshihara, K., and Kobuke, Y. *J. Am. Chem. Soc.* **124**, 22–23 (2002).

[87] Thorne, J. R. G., Kuebler, S. M., Denning, R. G., Blake, I. M., Taylor, P. N., and Anderson, H. L. *Chem. Phys.* **248**, 181–193 (1999).

[88] Kuebler, S. M., Denning, R. G., and Anderson, H. L. *J. Am. Chem. Soc.* **122**, 339–347 (2000).

[89] Sternberg, E. D., Dolphin, D., and Bruckner, C. *Tetrahedron* **54**, 4151–4202 (1998).

[90] Medforth, C. J., Senge, M. O., Smith, K. M., Sparks, L. D., and Shelnutt, J. A. *J. Am. Chem. Soc.* **114**, 9859–9869 (1992).

[91] Crane, B. R., Siegel, L. M., and Getzoff, E. D. *Science* **270**, 59–67 (1995).

[92] Gentemann, S., Medforth, C. J., Forsyth, T. P., Nurco, D. J., Smith, K. M., Fajer, J., and Holten, D. *J. Am. Chem. Soc.* **116**, 7363–7368 (1994).

[93] Gentemann, S., Nelson, N. Y., Jaquinod, L., Nurco, D. J., Leung, S. H., Medforth, C. J., Smith, K. M., Fajer, J., and Holten, D. *J. Phys. Chem. B* **101**, 1247–1254 (1997).

[94] Chirvony, V. S., van Hoek, A., Galievsky, V. A., Sazanovich, I. V., Schaafsma, T. J., and Holten, D. *J. Phys. Chem. B* **104**, 9909 (2000).

[95] Chen, D.-M., Liu, X., He, T.-J., and Liu, F.-C. *Chem. Phys.* **289**, 397 (2003).

[96] Jelovica, I., Moroni, L., Gellini, C., Salvi, P. R., and Orlic, N. *J. Phys. Chem.* **109**, 9935 (2005).

[97] Cheng, B., Munro, O. Q., Marques, H. M., and Scheidt, W. R. *J. Am. Chem. Soc.* **119**, 10732–10742 (1997).

[98] Ohno, O., Kaizu, Y., and Kobayashi, H. *J. Chem. Phys.* **82**, 1779 (1985).

[99] Vogel, E., Haas, W., Knipp, B., Lex, J., and Schmickler, H. *Angew. Chem. Int. Ed. Engl.* **27**, 406 (1988).

[100] Berlmann, I. *Handbook of Fluorescence Spectra of Aromatic Molecules.* Academic Press, (New York 1971).

[101] Lakowicz J. R. *Principles of Fluorescence Spectroscopy.* Kluwer, New York, 2nd ed., (1999).

[102] Gouterman, M. *J. Chem. Phys.* **30**, 1139 (1959).

[103] Nagashima, U., Takada, T., and Ohno, K. *J. Chem. Phys.* **85**, 4524–4529 (1986).

[104] Strickler, S. J. and Berg, R. A. *J. Chem. Phys.* **37**, 814 (1962).

[105] Marcelli, A., Foggi, P., Moroni, L., Gellini, C., Salvi, P. R., and Jelovica, I. *J. Phys. Chem. A* **111**, 2276–2282 (2007).

[106] Dobryakov, A., Kovalenko, S., and Ernsting, N. *J. Chem. Phys.* **123**, 044502 (2005).

[107] Akimoto, S., Yamazaki, T., Yamazaki, I., and Osuka, A. *Chem. Phys. Lett.* **309**, 177 (1999).

[108] Baskin, J. S., Yu, H.-Z., and Zewail, A. H. *J. Phys. Chem. A* **106**, 9837 (2002).

[109] Elsaesser, T. and Kaiser, W. *Annu. Rev. Phys. Chem.* **42**, 83–107 (1991).

[110] Englman, R. and Jortner, J. *Mol. Phys.* **18**, 145–160 (1970).

[111] Gurzadyan, G. G., Tran-Thi, T.-H., and Gustavsson, T. *New Trends in Atomic and Molecular Spectroscopy*, volume 4060 SPIE. G. G. Gurzadyan and A. Karmenyan V Eds., (Bellingham WA 2000).

[112] Karolczak, J., Kowalska, D., Lukaszewicz, A., Maciejewski, A., and Steer, R. *J. Phys. Chem. A* **108**, 4570–4575 (2004).

[113] Avilov, I. V., Panarin, A. Y., and Chirvony, V. S. *Chem. Phys. Lett.* **389**, 352–358 (2004).

[114] Gurzadyan, G. G., Tran-Thi, T.-H., and Gustavsson, T. *J. Chem. Phys.* **108**, 385 (1998).

[115] Yu, H.-Z., Baskin, J. S., and Zewail, A. H. *J. Phys. Chem. A* **106**, 9845–9854 (2002).

[116] Sorgues, S., Poisson, L., Raffael, K., Krim, L., Soep, B., and Shafizadeh, N. *J. Chem. Phys.* **124**, 114302 (2006).

[117] Boffi, A., Wittenberg, J. B., and Chiancone, E. *FEBS Lett.* **411**, 335 (1997).

[118] Challa, J. R., Gunaratne, T. C., and Simpson, M. C. *J. Phys. Chem. B* **110**, 19956–19965 (2006).

[119] Okazaki, I., Hara, Y., and Nagaoka, M. *Chem. Phys. Lett.* **337**, 151–157 (2001).

[120] Mukai, M., Savard, P. Y., Ouellet, H., Guertin, M., and Yeh, S. R. **41**, 3897–3905 (2002).

[121] Grogan, T. G., Bag, N., Traylor, T. G., and Madge, D. *J. Phys. Chem.* **98**, 13791–13796 (1994).

[122] Petrich, J. W., Lambry, J.-C., Balasubramanian, S., Lambroght, D., Boxer, S. G., and Martin, J.-L. *J. Mol. Biol.* **238**, 437–444 (1994).

[123] Vasudevan, S. G., Armarego, W. L., Shaw, D. C., Lilley, P. E., Dixon, N. E., and Poole, R. K. *Mol. Gen. Genet.* **226**, 49–58 (1991).

[124] Bonamore, A., Gentili, P., Ilari, A., Schininà, M. E., and Boffi, A. *J. Biol. Chem.* **278**, 22272–22277 (2003).

[125] Bonamore, A., Chiancone, E., and Boffi, A. *Biochim. Biophys. Acta* **174**, 1549 (2001).

[126] Mukai, M., Savard, P. Y., Ouellet, H., Guertin, M., and Yeh, S. R. **41**, 3897–3905 (2002).

[127] Nelson D. L. and Cox M. M. *Lehninger, Principles of Biochemistry.* W. H. Freeman and Company, New York, fourth edition, (2005).

[128] Bagnetti, A. *Tesi di Laurea.* Università degli Studi di Perigia, (2008).

[129] Islam, S. D. M., Susdorf, T., Penzkofer, A., and Hegemann, P. *Chem. Phys.* **295**, 137–149 (2003).

[130] Stanley, R. J. and MacFarlane IV, A. W. *J. Phys. Chem. A* **104**, 6899–6906 (2000).

List of publications

Publications related to this thesis

1. **A. Marcelli**, P. Foggi, L. Moroni, C. Gellini, P.R. Salvi, I.J. Badovinac
   "Relaxation Properties of Porphyrin, Diprotonated Porphyrin, and Isoelectronic Tetraoxaporphyrin Dication in the S2 State"
   J. Phys. Chem. A (2007), 111, 2276-2282

2. **A. Marcelli**, P. Foggi, L. Moroni, C. Gellini, P.R. Salvi
   "Excited State Absorption and Ultrafast Relaxation Dynamics of Porphyrin, Diprotonated Porphyrin and Tetraoxaporphyrin Dication"
   J. Phys. Chem. A (2008), 112, 1864-1872

3. L. Moroni, C. Gellini, P.R. Salvi, **A. Marcelli**, P. Foggi
   "Excited States of Porphyrin Macrocycles"
   J. Phys. Chem. A (2008), 112, 11044-11051

Publications not related to this thesis

1. P. Sassi, **A. Marcelli**, M.Paolantoni, A. Morresi, R.S. Cataliotti
   "Structural Properties of 1-Octanol/n-Ocane Mixtures Studied by Brillouin Scattering"
   J. Phys. Chem. A (2003), 107, 6243-6248

2. C. Bazzicalupi, A. Bencini, L. Bussotti, E. Berni, S. Biagini, E. Faggi, P. Foggi, C. Giorgi, A. Lapini, **A. Marcelli**, B. Valtancoli
   "A dizinc complex for selective fluorescence sensing of uridine and uridine-containing dinucleotides"
   Chem. Commun. (2007), 1230-1232

3. S. Cicchi, P. Fabbrizzi, G. Ghini, A. Brandi, P. Foggi, **A. Marcelli**, R. Righini, C. Botta
   "Pyrene Excimers Based Antenna Systems"
   Chemistry - A European Journal, on line in advance of print

4. E. Giorgetti, S. Cicchi, M. Muniz-Miranda, G. Margheri, T. Del Rosso, A. Giusti, A. Rindi, G. Ghini, S. Sottini, **A. Marcelli**, P. Foggi
   "Surface Enhanced Fluorescence and Surface Enhanced Raman Scattering of ultrathin layers of bichromophoric antenna systems absorbed on nanoislands silver films"
   J. of Lumin., accepted

5. E. Giorgetti, S. Cicchi, M. Muniz-Miranda, G. Margheri, T. Del Rosso, A. Giusti, A. Rindi, G. Ghini, S. Sottini, **A. Marcelli**, P. Foggi
   "Self assembled monolayers of a bichromophoric antenna system adsorbed on silver or gold nanoisland films"
   Langmuir, submitted

Acknoledgements

To conclude, I would like to thank the people who have significantly contributed to the research presented in this thesis.
First of all, I would like to express gratefulness to Prof. Roberto Righini and Prof. Paolo Foggi for giving me the opportunity to undertake this project.
Many thanks to Dr. Laura Bussotti for her useful suggestions and support during my PhD years and for reviewing some parts of my thesis.
Particular thanks to Prof. Piero Salvi, Dr. Cristina Gellini and Dr. Laura Moroni for their feedback on the porphyrins time-resolved data, they have always given me interesting perspectives.
I am grateful to Dr. Alessandro Feis for his critical reading of this thesis and to Prof. Giulietta Smulevich and coworkers for inviting me to take part in their group meetings and helping me reflect on my results.
Thanks to Prof. Alberto Boffi for kindly providing samples of the investigated proteins.
Thanks also to the LENS staff, in particular to Andrea Lapini, Sandra Mosquera Vázquez, Patricia Tourón Touceda and to the technicians of electronic and mechanical workshops: Marco De Pas, Mauro Giuntini,Alessio Montori, Riccardo Ballerini and Ahmed Hajeb.
Finally, a very warm thank you to Enzo for designing the front cover of my thesis.